UNIVERSITY OF SOUTHAMPTON

Superluminous Supernovae in Large Astronomical Surveys

by

Szymon Prajs

A thesis submitted in partial fulfillment for the
degree of Doctor of Philosophy

in the
Faculty of Physical Sciences and Engineering
School of Physics and Astronomy

March 2019

UNIVERSITY OF SOUTHAMPTON

Abstract

Faculty of Physical Sciences and Engineering
School of Physics and Astronomy

Doctor of Philosophy

by Szymon Prajs

This thesis focuses on the photometric classification and the properties of superluminous supernovae (SLSN), as observed in large astronomical surveys. When working with large samples of transients and a limited spectroscopic follow-up campaign, photometric classifications are the only tool available to select objects which can subsequently be used to study their statistical properties including the rate and its evolution.

I begin by introducing the surveys which produce the transients archive used in this work. I discuss the effect of their properties and design on the work performed in this thesis. I also introduce the sources of auxiliary data, including the spectroscopic follow-up facilities as well as summarise the Dark Energy Survey (DES) spectroscopic sample of SLSNe.

Next, I develop a number of models and techniques used to simulate both core-collapse supernovae (CCSN) and SLSNe. I use the spin-down of a magnetar model in conjunction with spectroscopic UV absorption templates to build SLAP, a tool for simulating SLSN at any redshift, in any arbitrary photometric system. Similarly, I develop CoCo which can be used to simulate and generate the templates for CCSNe.

I then use the tools developed in this thesis to build a definition of SLSNe in terms of the spin-down of a magnetar model and apply it to a sample of transients detected by the Supernova Legacy Survey (SNLS), uncovering one previously unclassified SLSN. I use this and two previously spectroscopically confirmed objects to calculate the rate of SLSNe at z$\sim$ 1 with the help of a Monte Carlo simulation of the survey. I find the rate to be $91^{+76}_{-36}\,\mathrm{SNe\,Yr^{-1}\,Gpc^{-3}}$, equivalent to $2.2^{+1.8}_{-0.9} \times 10^{-4}$ the rate of CCSN at the same redshift.

Finally, I use the models of CCSN and SLSNe developed in this work as well as the simulations of SN Ia and AGN to build a large artificial training sample of DES-like transients to be used in the photometric selection of SLSNe. Based on this, I build a two-stage machine learning photometric classification tool. In the first step I separate SN from other contaminating transients with an accuracy of 99.8%. Then, I separate the sample of SNe into its individual subclasses, achieving an overall accuracy of 97.85%. Using complementary selection techniques, I identify 26 new SLSNe candidates in DES.

"...isn't it a noble and enlightened way of spending our brief time in the sun to work at understanding the universe and how we have come to wake up in it?"

Richard Dawkins

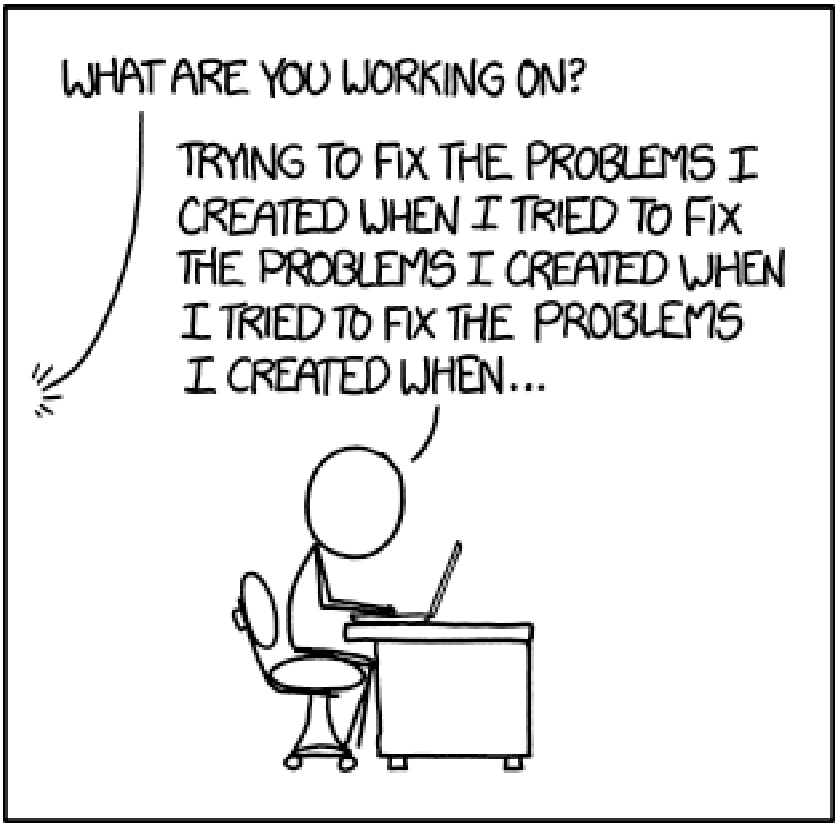

xkcd.com/1739

Contents

List of Figures

List of Tables

Abbreviations

SN	**S**uper**N**ova
SLSN	**S**uper-**L**uminous **S**uper**N**ova
BYO	**B**aryon **A**coustic **O**scillations
SNLS	**S**uper**N**ova **L**egacy **S**urvey
CFHT	**C**anadian-**F**rench-**H**awaiian **T**elescope
CFHT-LS	**C**anadian-**F**rench-**H**awaiian **T**elescope **L**egacy **S**urvey
DES	**D**ark **E**nergy **S**urvey
VLT	**V**ery **L**arge **T**elescope
PSF	**P**oint **S**pread **F**unction
SMP	**S**cene **M**odeling **P**hotometry
SN	**Si**gnal-to-**N**oise
SPCC	**S**upernova **P**hotometric **C**lassification **C**hallenge
AAT	**A**nglo-**A**ustralian **T**elescope
DDT	**D**irectors **D**iscretionary **T**ime
ATel	**A**stronomical **Tel**egram
KDE	**Kernel** **D**ensity **E**stimate
GP	**G**aussian **P**rocess
GPR	**G**aussian **P**rocess **R**egression
ML	**M**achine **L**earning
ANN	**A**rtificial **N**eural **N**etwork
CNN	**C**onvolutional **N**eural **N**etwork

Physical Constants

Speed of Light $c = 2.997\ 924\ 58 \times 10^{8}\ \mathrm{ms^{-S}}$ (exact)

$H_0 = 72\ \mathrm{Km\ s^{-1}Mpc^{-1}}$

$\omega_M = 0.3$

$\omega_\Lambda = 0.7$

$\mathrm{k}_B = 5.6704 \times 10^{-5}\ \mathrm{ergs^{-1}cm^{-4}K^{-4}}$

Symbols

z	
D_L	(cm)
M	
m	
f	$(erg\ s^{-1} cm^{-2} \AA^{-1})$
R	(cm)
D_L	(K)
B	(G)
P	(ms)
τ_M	(day)
τ_p	(day)
E_k	(erg)
κ	($\mathrm{cm}^2\ \mathrm{g}^{-1}$)
M_{ej}	(Kg)
ρ_{SLSN}	($\mathrm{Gpc}^{-3}\ \mathrm{Yr}^{-1}$)
$\mathcal{N}$	
$\mathcal{L}$	

Declaration of Authorship

I, Szymon Prajs, declare that this thesis titled, 'Superluminous Supernovae in Large Astronomical Surveys' and the work presented in it are my own. I confirm that:

- This work was done wholly or mainly while in candidature for a research degree at this University.
- Where any part of this thesis has previously been submitted for a degree or any other qualification at this University or any other institution, this has been clearly stated.
- Where I have consulted the published work of others, this is always clearly attributed.
- Where I have quoted from the work of others, the source is always given. With the exception of such quotations, this thesis is entirely my own work.
- I have acknowledged all main sources of help.
- Where the thesis is based on work done by myself jointly with others, I have made clear exactly what was done by others and what I have contributed myself.

Signed: ______________________________

Date: ______________________________

Acknowledgements

First of all I would like to sincerely thank my supervisor, Professor Mark Sullivan, for his fantastic support, mentorship and the opportunities he has given me over the last four years. I thoroughly enjoyed all our discussions, meetings and working together. Even at times when my motivation was lacking, Mark was able to raise my spirit and give me the goals and directions that I needed to get me to where I am now.

I would also like to express my gratitude towards to everyone in the Southampton Supernova group, with whom I had the pleasure of collaborating and sharing my time at Southampton. I would like to specifically single out Mat Smith, who was always there to answer my every small questions and help me with the countless bugs and mistakes made along the way.

Most importantly, I would like to thank my Fiancée Toyah without whom I would have never been able to get to this point. Despite the months of putting up with my long working hours, stress, bad moods and constant complains, she was always by my side and on my side. I could have never wished for a more amazing, loving and wonderful companion and I will always remain grateful for all the help and comfort she has provided me in these last difficult months.

To Toyah…

Chapter 1

Introduction

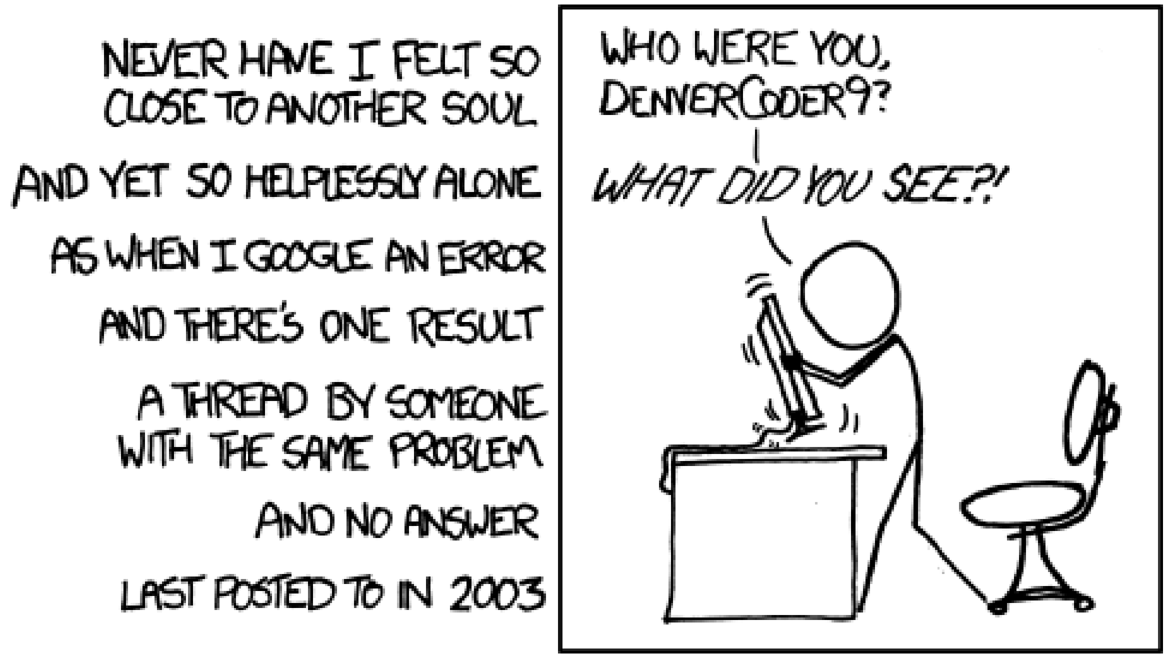

xkcd.com/979

Supernovae (SN) are extremely luminous stellar explosions. At their brightest, they can outshine the galaxy that gave birth to them, making them visible at great distances and far back in time. SNe have been observed by stargazers since the dawn of humankind. By studying nebulae formed as remnants of past explosions, as well as ancient records we know that human history is filled with observations of 'guest stars' most famously in 1054 where the SN, now observed as the Crab nebula, has been recorded in China, seen to be brighter than the full moon at night and visible during the day, as well as the SN1574, known as the Tycho SN and SN1604 in the end of the 16th and beginning of 17th centuries.

Despite their early observations, the term 'Supernova' was not coined until 1934 when Baade & Zwicky (1934) were able to estimate their absolute magnitudes. Using Cepheid variables, they measured the distance to several SN host galaxies and found them to be significantly greater than those of classical 'novae'. The prefix 'super' reflects their absolute luminosity which must be much greater than that of novae to explain their bright observed magnitudes.

1.1 SN classification

At that point of their discovery, little has been known about the properties and physical origin of these extreme objects, largely due to the scarcity of their observations at that time (Zwicky, 1938). In the years to come, many generations of astronomers built increasingly larger and more sensitive surveys, observing thousands of SNe to date (Alsabti & Murdin, 2017). With this came our understanding of the various types and flavours of SNe and the breath of the variation in the objects that can give rise to such brilliant explosions.

1.1.1 SN Ia

Perhaps the most well understood and most heavily studies class are the thermonuclear SNe. While a number of their subclasses exists (amongst others: SN .Ia, SNÍax, SN Ia-91T, SN Ia-91bg Alsabti & Murdin, 2017) all of these objects likely share a similar physical origin to the main SN Ia class. There are competing theories explaining their origin, both describe a thermonuclear explosion of a white dwarf (WD) star but differing in the mechanism which triggers the ignition. In the single-degenerate scenario (Whelan & Iben, Icko, 1973) a WD, in a binary system, accretes matter from a main-sequence or red giant star until it reaches the Chandrasekhar limit defined as the point at which the electron degeneracy pressure can no longer support the star against a gravitational collapse, resulting in an increase in pressure and subsequent thermonuclear ignition of its core. The alternative explanation suggests that instead of a single WD, a binary WD system interacts internally, spiralling down through the release of gravitational waves, resulting in their eventual collision triggering a powerful shockwave, sufficient to ignite the degenerate matter even at sub-Chandrasekhar limit masses (Iben & Tutukov, 1984). Both of the above mechanisms result in a production of $\sim$0.7M$_\odot$) of ^{56}Ni (Scalzo et al., 2014) which decay radioactively to ^{56}Co and Fe56 producing a vast quantity of high energy Gamma radiation, which is subsequently reproduced by the SN ejecta into visible light.

1.1.2 SN II

The origin of SN II in many ways mirrors that of SN Ia; both are the result of the end point of the evolution and the death of their progenitor star. SN II are born when a $>8M_\odot$ star exhausts all of its nuclear fuel at the end of the iron burning phase (Clayton, 1968). At that point, the core is supported purely by the electron degeneracy pressure and collapses shortly afterwards into neutron star under the gravitational pressure of the outer layers of the star. The infalling shells rebound of the, now, solid core and are further energised and accelerated by either the neutrinos released in the collapse of the degenerate core (Burrows & Lattimer, 1987) or jets formed due to the accretion of the infalling matter onto the core (Khokhlov et al., 1999; Burrows et al., 2007).

In this process, only a small, in comparison to SN Ia, amount of the ^{56}Ni is formed which alone could not explain neither the luminosity of these core-collapse SNe (CCSN) nor their light curve morphologies which are often associated with a sharp rise followed by either a long plateau phase (SN IIP) or a linear decline (SN IIL) (Alsabti & Murdin, 2017). These are the effect of Hydrogen recombination (ionised to neutral) in the outer layer of the ejecta, resulting in a blackbody-like a spectrum with prominent P-cygni profiles visible in the spectra. Additionally, some objects also show narrow emission lines (SN IIn), of mostly hydrogen, which are the result of the interactions between the SN ejecta and extended material ejected by the progenitor star some time before the main event (Pastorello et al., 2002; Sternberg, 2013).

1.1.3 SN Ib/c

SN Ib/c have a very similar origin to SN II. They are also a result of a core collapse of a giant star but significantly they originate from larger and more ‘stripped’ stars. These objects are often referred to as Stripped-Envelope SNe reflecting the fact that no hydrogen (SN Ib) nor helium (SN Ic) are visible in their spectra as they were removed from the surface of the star by either winds or coronal mass ejections a relatively long time period to the onset of the SN event. Some theories suggest that the stripping cannot be explained solely using wind and coronal ejections and must be a result of an interaction with a companion star (Tauris et al., 2013).

Thanks to the higher mass of the progenitor star, these objects often result in a larger production of ^{56}Ni, resulting in a higher luminosity and a morphology which in the extreme cases can closely resemble that of a SN Ia. Spectroscopically, this class of SNe shows a strong formation of Oxygen and Carbon and well as small quantities of other, intermediate-mass elements (Filippenko, 1997).

1.1.4 Other subclasses

Outside of the main, or most commonly detected, subclasses of SNe lives a number of rarer and more exotic transient types. Amongst these, there is a number of intermediate classes of CCSNe that originate at the boundaries of the progenitor scenarios. This includes SNIIb, SNIbn and SNIbc amongst others (Alsabti & Murdin, 2017), however, an overlap also exists between the SN Ia and the interacting CCSN. SN Ia-CSM are one of the most luminous classes of SNe as the extreme brightness of SN Ia is enhanced further by the interaction of the ejecta with a layer of circumstellar material (CSM) likely ejected by the companion star (Dilday et al., 2012).

As SN surveys become more sensitive and sophisticated, the numbers of known SN classes grew as well. In recent years, higher cadence SN searches have led to the discovery of a new class of Rapidly Evolving Transients (RAT) with an extreme variation in their peak luminosity ranging from -15 M -22 (Pursiainen et al., 2018). Little is yet known about their physical origins, however, their observations suggest a featureless blackbody-like spectrum, often associated with initially high temperatures followed by rapid cooling. A possible interpretation of these objects is an object which undergoes a direct collapse to a black hole, producing none or little ^{56}Ni, explaining the lack of a slowly declining light curve. In this scenario, the observed morphology is a result of the interaction between the SN shock with an extended shall of dense wind (Piro, 2015), similarly to an effect sometimes observed in superluminous supernovae (SLSN).

1.2 Superluminous Supernovae

Superluminous supernovae (SLSNe) are a recently identified class of transients defined as events with an absolute magnitude brighter than -21 ($M < -21$) (Gal-Yam, 2012). They appear 10-100 times brighter than normal supernova events, and form at least two distinct classes: SLSNe-II, which show signatures of interaction with CSM via hydrogen and other lines (Ofek et al., 2007a; Smith et al., 2007; Drake et al., 2011), and SLSNe-I (or SLSNe-Ic), which are hydrogen-poor (Quimby et al., 2011). While SLSNe-II may naturally be explained as an extension of the fainter SN IIn events, the power source behind SLSNe-I remains a subject of debate (Gal-Yam, 2012).

SLSNe-I (SLSN; henceforth) are the protagonists of this thesis. In this section, I will introduce the observations that have led to their discovery, their spectroscopic and photometric properties as well as their host galaxies. Furthermore, I will introduce their most commonly accepted formation theories and their effect on the rate of SLSN.

1.2.1 Discovery

The observational properties of SLSNe had a strong impact on the timing of their discovery. As a rare but luminous class of transients, the probability of was low in the early SN surveys in the local universe due to lower sensitivity and search volume. The first signs of the existence of a new class of extremely luminous SNe came with the discovery of SN2005ap (Quimby et al., 2007), SN2006gy (Ofek et al., 2007b) and SCP06F6 (Barbary et al., 2009). In each case, the distance measurements for the objects have placed them at a luminosity ∼100 times brighter than ordinary SNe. However, the low quality of their early light curves and spectra along with a lack other example resulted in these objects being treated more as extremes of the known classes of objects instead of a separate new class.

This picture has evolved dramatically in the last decade with the onset of a number of deep, wide field surveys such as the Texas Supernova Search (TSS; Quimby, 2006), the Palomar Transient Factory (PTF; Law et al., 2009; Rau et al., 2009), the Supernova Legacy Survey (SNLS; Astier et al., 2005; Guy et al., 2010; Perrett et al., 2010), the Panoramic Survey Telescope & Rapid Response System (Pan-STARRS; Kaiser et al., 2010) and the Dark Energy Survey (DES; Flaugher, 2005). With an increased sensitivity, longer observing season and a lack of host galaxy selection bias ; each one of these surveys was responsible for detecting several SLSNe, jointly shaping our current understanding of this new and exciting area of SNe research.

1.2.1.1 Luminous Supernoavae

The terms ‘Luminous Supernovae’ and ‘Superluminous Supernovae’ became popular in the literature upon the discovery of SN2007bi (Gal-Yam et al., 2009) during the science verification phase of PTF. Its light curve, containing only the single r-band filter, lacked the rise time information but demonstrated a very slow decline consistent with the radioactive decay of a large mass of ^{56}Ni. At that time, it was believed that such event could be a result of a Pair Instability SNe (PISN; Section 1.2.3) and were therefore thought to be a new class of transients.

Following shortly from this, a number of objects were discovered with similar properties. Quimby et al. (2011) presented a sample of SNe detected by PTF along with the first, comprehensive sample of their spectra. While mostly consisting of a blue, featureless blackbody continuum, some absorption lines including CII, MgII and OII (see Mazzali et al., 2015, for more recent line identification) were identified in all spectra in this sample, confirming the redshifts and extreme luminosity of these events.

1.2.2 Properties

Beyond confirming their redshifts, the prominent UV spectral lines can also be used to measure the expansion velocity and temperature of the photospheres of SLSNe, measured around the maximum light to be of the order of ~15000km/s and ~10,000K respectively (Inserra et al., 2013). This suggests that SLSNe are a class of very energetic events powered by an internal engine capable to re-energise the ejecta to produce the observed temperature, impossible to sustain in a scenario where the SN is expanding adiabatically in absence of internal heating source.

The combination of the size of the photosphere and the extreme temperatures results in objects which are extremely luminous, particularly in the blue bands where most of their luminosity is being emitted (Yan et al., 2017). From the point of view of their detectability, this makes SLSNe fantastic probes of the high redshift universe as the increasing distance modulus is partially offset by the increase in observed flux as we probe the UV SED redshifted into the visible bands (Smith et al., 2018).

Another clear observable difference between SLSNe and other classes of SNe is their slow evolution (Gal-Yam et al., 2009; Inserra et al., 2013; Nicholl et al., 2015a). Their rise time of ~30 days in the rest-frame and decline times as slow as 0.01 magnitudes per day are vastly longer timescales than those of other luminous classes of transients including SN Ia and Gamma Ray Burst (GRB) afterglows.

1.2.3 Origins

The most popular model in the literature to explain SLSNe involves energy input from the spin-down of a newly-formed magnetar following a CCSN (Kasen & Bildsten, 2010; Woosley, 2010; Inserra et al., 2013), although alternative models involving PISN (Woosley et al., 2007; Yan et al., 2015) or interaction with a hydrogen-free CSM (Chevalier & Irwin, 2011; Chatzopoulos et al., 2013; Sorokina et al., 2015) have also been proposed.

1.2.3.1 Magnetar model

The spin-down of the magnetar model postulates that the birth of a SLSN is linked with the death of an extremely massive star with an intrinsically high angular momentum and magnetic field. As this star collapses, it forms a Magnetar, defined as a neutron star with a magnetic field of B~ 10^{14}G and spin period, P~1ms. As the young magnetar remains shrouded by the relatively dense ejecta in the early phases of the SN, the rapidly rotating and magnetised core interacts with the inner layers of the SN, through the process of magnetic breaking, converting some of its rotational inertial into high energy radiation. The x-rays photons produced in this process are then thermalized by the ejecta and re-emitted as the observed blackbody radiation.

A further prediction of this model is the formation of a powerful shockwave, at the birth of the magnetar, which propagates through the ejecta compressing it into a thick layer (Jerkstrand et al., 2016; Chen et al., 2017) expanding at a uniform rate (Inserra et al., 2013), unhampered by any interactions and collisions between varying velocity layers as observed in other SNe. This results in a high and stable opacity value, leading to a full trapping of the high energy radiations by the ejecta.

There is a range of observational evidence supporting this model. have demonstrated that the total radiated bolometric luminosity of SLSNe are consistent with the predicted energy emitted by a spin-down of a magnetar (Inserra et al., 2013). Furthermore, the decline phase of these SNe, which was shown to be difficult to model under other assumptions, is very well explained by the slow energy deposition into the ejecta by the magnetar. However, perhaps most intriguingly, a thorough examination of the spectra of SLSNe in Mazzali et al. (2016) showed that the existence of some of the lines could only be attributed to a non-thermal ionisation of a dense ejecta by a luminous X-ray source.

1.2.3.2

Amongst the alternative models describing the origin of SLSNe, PISN remains a plausible alternative, especially in the cases of some of the less luminous and slowly declining objects. PISNe have been theorised for a number of decades (Fraley, 1968) and are a result of the end point of the evolution of extremely massive stars with mass, $\mathrm{M}\sim140\mathrm{M}_{odot}$. At this extreme limit, the density and temperature of the core are sufficiently high to achieve a rate of electron-positron pair production higher than their rate of annihilation. This results in a decrease in the pressure and subsequently a further collapse of the which in turn increases its density and temperature leading to a runaway reaction that culminates in a thermonuclear detonation of the core, not unlike that of SN Ia albeit producing significantly larger quantities of the radioactive ^{56}Ni in the process.

While the development of the PISN models continues, it is not unlikely that the majority of SLSNe can be explained using this model as it is believed (Jerkstrand et al., 2016) that such events would likely result in a red SED due to large amount of Iron produced in the explosion leading to line blanketing of the UV regions of their spectra, similarly to the effect observed in other ^{56}Ni powered SNe.

1.2.3.3 Interactions with the Circumstellar Material

A similar scenario has been suggested as the powering mechanism behind SLSN-Ic (Chevalier & Irwin, 2011). Here, the lack of hydrogen or helium detection in their spectra is attributed to the SN event taking place in an environment where the star has either efficiently burned all of its hydrogens or expelled it a long time before the core-collapse event, resulting in the star shrouded by CSM composed of intermediate-mass elements alone. Similarly, to the PISNe, this model is not believed to be the likely source of the majority of the SLSNe population due to the lack of hydrogen detections in even very late light curves (Jerkstrand et al., 2016), as would be predicted by the model.

1.2.4 Host Galaxies

Additional clues about the origins and conditions required to form SLSNe also provided by the environments in which they occur: predominantly vigorously star-forming and low-metallicity dwarf galaxies (e.g., Lunnan et al., 2014; Leloudas et al., 2015a; Angus et al., 2016). There are now a number of clues which suggests that a direct consequence of the scenario where the spin-down of the magnetar is responsible for the formation of .

The preference for low-metallicity environments is supported by the modelling of the SLSN spectra, which favours a fairly low metal abundance (Mazzali et al., 2016). It has also been suggested (Nomoto et al., 2016) that it is unlikely for a high metallicity star to retain sufficient mass, throughout its evolutionary cycle, to result in a SN with $\sim$40M$_\odot$ of ejected material. Furthermore, metallicity might be the answer to the questions raised about the formation of a star which is simultaneously extremely magnetised and rapidly rotating as such extreme objects have, to date, not been observed in the local universe.

Another driving factor behind the connection to young, metal-poor, heavily star-forming dwarf galaxies is the formation rate of massive stars known to be associated with these conditions as seen locally in the Small Magellanic Cloud (SMC). If the strong preference for a young environment reflects a real physical effect, any evolution in the SLSN rate with redshift should also track the cosmic star-formation and metal enrichment history of the Universe, and the underlying evolving populations of galaxies.

1.2.5 Rates

Of particular interest in this thesis, and a topic of Chapter 4, is the rate of SLSN. The late discovery and identification of SLSN are heavily attributed to their rarity. Even after several years of study, the number of well-observed SLSNe does not yet exceed 100 objects (e.g., see compilations in Inserra & Smartt, 2014; Papadopoulos et al., 2015; Nicholl & Smartt, 2016; De Cia et al., 2017a). Initial estimates placed the rate of SLSNe at less than one for every 1000 core-collapse supernovae (Quimby et al., 2011), and more recent studies are broadly consistent with this (Quimby et al., 2013; McCrum et al., 2014a). However, prior to this thesis, there has been no direct measurement of the SLSN rate for a well-controlled optical transient survey. Such a measurement can provide constraints on progenitor models, as there must, at the very least, be a sufficient number of any putative progenitor system to produce the observed SLSN rate.

1.2.6 Connection to Long GRBs

One of the latest pieces of the SLSNe puzzle that came to light in the recent years is their potential connection to Long (and more importantly, Ultra Long) Gamma Ray Bursts (GRB). From their earliest detections, the similarity in the total energy radiated by these very morphologically different events has raised questions. In particular, some models for the formation of Long GRBs involve the creation of a young Magnetar, albeit with different initial conditions to the model postulated for SLSNe (Margalit et al., 2018). The connection between the classes became apparent upon discovery of GRB 111209A/SN2011kl, first detected as an Ultra Long GRB (ULGRB) with an event duration of $\sim$ 1000s. The event was then followed by a luminous and slowly declining light curve alike to those observed for SLSNe (Greiner et al., 2015). Spectroscopic follow-up provided further evidence that the object is similar in origin to its more luminous cousin (Mazzali et al., 2016) and likely also driven by a spin-down of a Magnetar (Metzger et al., 2015).

1.3 SN Surveys

One of the most instrumental advances that lead to the discovery and the development of our understanding surrounding SLSNe is the dawn of the new era of automated, untargeted wide field SN surveys. While there is now an ever-growing number of such projects, I endeavour to avoid the discussion of individual surveys and instead summarise their general features that impact the study of SLSNe. In particular, I would like to focus the attention of this section on the limitations of the past, current, and future surveys and the impact they have on the work presented in this thesis, affecting the search for and classification of high redshift SLSNe.

1.3.1 Cadences

It is perhaps unsurprising that in the field dominated by the study of SN Ia and their use as cosmological probes (Perlmutter et al., 1999; Riess et al., 1998), the large majority of surveys operated in the last two decades optimise their design to maximise the quality of their relatively short light curves. The cadences, i.e. the frequency of observations, are chosen at ∼5 days, sufficient to give each SN Ia light curve between three to five points during the critical rise phase, as necessary for high precision model fitting used in the cosmological studies. A number of surveys including SDSS, PTF, Pan-STARRS, SNLS amongst others conform to this common design ideology.

As rare, slowly evolving and particularly brilliant objects, SLSNe do not require the same observing criteria as their less luminous cousins. In fact, a design that would maximise their detectability would focus on lower cadence and shallower fields and instead use the telescope time to search a larger observing area (Scovacricchi et al., 2015). Ideally, these fields should also be placed in the parts of the sky visible for a long period of time. While surveys like this were attempted in the past (e.g. SUDSS; Section 2.3), they were met with particularly bad observing conditions and therefore never realising their full potential. As a result, all observations of SLSNe are limited to relatively short light curves (∼5 months), often observing the SNe at a very high signal to noise despite their low numbers.

The observing conditions have a huge effect on the detection and even more so on the analysis of SLSNe. In the past, single component survey, designed to focus only on SNe, unfavourable atmospheric conditions would usually result in a lower than designed cadence.

1.3.2 Differential photometry

Further to the uncontrollable by us cadence of the SN light curves, another component of survey designs that strongly affect our analysis is the algorithm used to extract the SN flux from their raw observations. Nearly all surveys, including those used in this thesis, rely on a technique known as Difference Imaging (Alard & Lupton, 1997) to measure the change in flux in the science frames compared to a template image.

This technique works on the principle of selecting high quality, low Point Spread Function (PSF), reference images which are then downgraded in quality to match that of the science images. In order to measure the flux correctly, the reference images must not contain any SN light and are therefore either collected sometime prior to the start of the survey or several years after the explosion epoch in case of data re-analysis. Once the science and reference images are matched in image quality, they are warped such as to match their photometric solutions. Next, the reference frame is subtracted from the science images resulting in a residual image containing, in the ideal case, only SN light.

As the final stage of the analysis, the flux of the object is measured using an aperture (in the case of fast, less precise pipelines) or PSF photometry (in the science analysis pipeline). A further difference between the reduction pipelines is the use of a fixed or variable SN centroid. Forced Photometry (Bertin, 2011), a technique often applied to the faintest transients, first measures the of the center of the point sources in the full time-series of images, before measuring the flux at that location. Besides providing an extremely accurate measurement of the position of the transient, it also allows for a much higher photometric precision and measurements of its uncertainties (Firth et al., 2015).

1.4 Cosmology and Distance measurements

The fields of Cosmology and SN research live in a fascinating symbiotic relationship. Without our understanding of the expansion of the universe, and the ability to use redshift as a distance measure, we would not be able to study SNe at high redshifts where estimating distances using alternative methods becomes near impossible. Conversely, SNe provides one of the most powerful tools for studying the cosmological parameters of our universe, famously leading to the discovery of the accelerated expansion of the universe (Riess et al., 1998; Perlmutter et al., 1999) for which Adam Riess, Brian Schmidt and Saul Perlmutter have been awarded the Nobel Prize in Physics in 2011.

1.4.1 Basic Cosmological Model

The question of the origin of the universe, its age and size have been at the forefront of scientific research since the dawn of time. For many millennia, we have seen our place at the centre of the known universe, putting us in a special position against other celestial objects. These allowed us to look further in the universe, slowly discovering that our home planet is only one of many orbiting the Sun, which is one of the billions of similar stars in our galaxy that forms a single spec in the vast structures of the ever-expanding and evolving web of the Universe.

One of the most important discoveries on this journey towards our current understanding of the origins of the universe came early in the 20th century when (Slipher, 1915) discovered that the wavelengths of the spectral line features observed for a large majority of local galaxies appear to be shifted towards the longer, or redder, wavelengths. This redshift became key to one of the greatest scientific discovery in human history when (Hubble, 1929) measured distances to these galaxies using Cepheid variables and discovered that the distance, d, to the galaxies is proportional to their velocity, v, (computed using the redshift as a Doppler shift), which he concluded was due to the expansion of the universe.

$$H_0 \;=\; v/d \;\approx\; 72\,\mathrm{Km\,s^{-1}\,Mpc^{-1}} \tag{1.1}$$

Hubble's discovery brought upon the birth of the field of cosmology with a number of theories, describing the evolution of the universe, being proposed in the years immediately to follow. After decades of debate, searching for evidence and paradigm-shifting discoveries, we now (Adam et al., 2016) know that we live in a universe which begun in the Big Bang, ∼13.7 Billion years ago. After a short, initial era where the radiation pressure dominated its expansion to the universe has entered a phase of matter domination before, ∼5 Billion years ago, the universe became dominated by the mysterious Dark Energy which drives its accelerated expansion.

1.4.2 Measuring the Cosmological Parameters

The measurements of cosmological parameters are, in essence, all based on the principle of observing known physical dimensions vs their apparent size as a function of redshift. In the context of the expanding universe, this is equivalent to measuring the evolution of the Hubble as a function of redshift. In the ΛCDM model, which described our current best understanding of cosmology, this relationship between the scale factor, define as $a = 1/(1+z)$, and Hubble constant is defined as:

$$H(a) \equiv \frac{\dot{a}}{a} = H_0\sqrt{\omega_R a^{-4} + \omega_M a^{-3} + \omega_k a^{-2} + \omega_\Lambda} \tag{1.2}$$

Where H_0 is the current, rest-frame Hubble constant, ω_R is the radiation pressure density parameter, ω_M is the matter density parameter and ω_Λ is the dark energy density term. It's important to note here that the majority of cosmological probes do not measure the absolute values of $\mathrm{H_0}$ and H(a) but instead determine their ratio.

The change in the Hubble constant can be therefore measured as the evolution in the apparent properties of any fixed quantity in the universe. A number of standard rulers (fixed length scales; e.g Baryon Acoustic Oscillation (BAO) (Cole et al., 2005; Eisenstein,

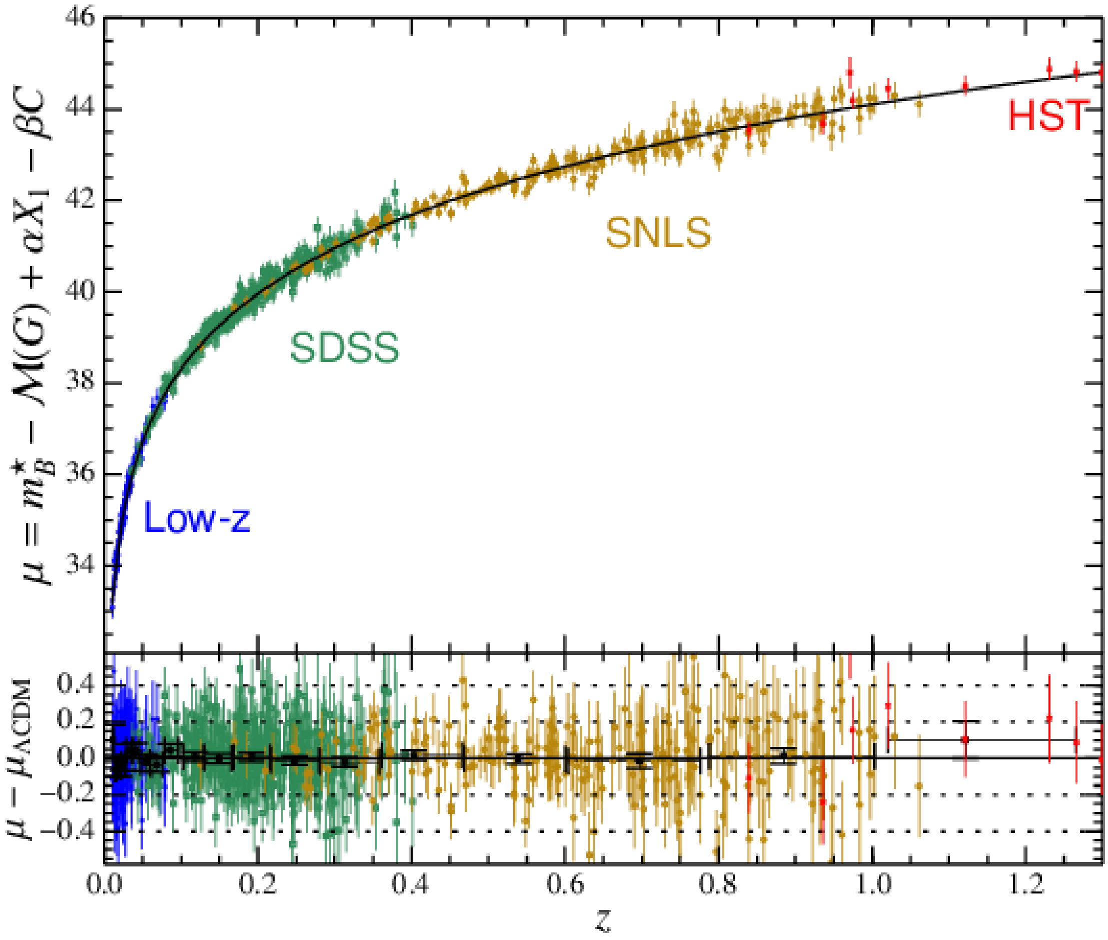

Figure 1.1: An example of a Hubble diagram reproduced from the Joint Light curve Analysis project (Betoule et al., 2014). ∼700 SN Ia form part of the sample which combines objects from the SNLS, SDSS, HST as well as low redshift SN observed by miscellaneous instruments.

2005)) and standard candles (objects of fixed luminosity; e.g SN Ia) have been proposed and are widely used in modern observational cosmology.

1.4.2.1 Cosmology with SNe

One of the most ground-breaking discoveries in the field of SN was the discovery that the luminosity SN Ia, is related to the width of the light curve. This relationship is known as the Phillips relation (Phillips, 1993) and forms the basis for the use of SN Ia as standardisable candles in a number of cosmological studies (Perlmutter et al., 1999; Riess et al., 1998; Astier et al., 2005; Betoule et al., 2014). Using the standardised luminosity of the objects we can measure the distance modulus, proportional to the ratio of H(a) and H_0, as a function of redshift giving the Hubble Diagram (Figure 1.1; Betoule et al., 2014)

One of the largest problems with using SNe as cosmological probes is the difficulty of detecting these objects at redshifts higher than z>0.6 due to the majority of their optical flux being redshifted into IR bands where our ground-based telescopes are less sensitive (Smith et al., 2018). It is perhaps not surprising that the possibility of SLSNe, which do not suffer from the same issues, possibly acting as standardisable candles (Inserra & Smartt, 2014; Papadopoulos et al., 2015; Inserra et al., 2017) has propelled the interest in the new class of luminous transients.

While still a subject to active debate, the most promising route towards their standardisation, presented in Inserra et al. (2017), suggests that absolute luminosity of SLSNe is inversely proportional to their decline time in a near inverse Phillips relation. Currently, these types of analysis are difficult to undertake due to the low number of complete and low redshift samples of objects, however, early indications do suggest a standardizability similar to those found in the early publication on the width-luminosity relationship of SN Ia (Inserra et al., 2017).

1.4.3 Redshift as a distance measure

In SN research, in alignment with most branches of stronomy, distance measurements are crucial for nearly all analysis. As SN are extremely distant and often associated with faint galaxies that are undetectable, redshift is often the only possible measure of their separation from us, the observers.

Luminosity distance is the measure used in astronomy as it directly corresponds to the distance modulus, defining the relationship between the absolute (M) and the apparent (m) magnitudes of an object with distance:

$$m = M + 5log(\frac{D_L}{10pc}) \tag{1.3}$$

Redshift and distance are not linearly proportional to each other and depend very strongly on the cosmological model used and its parameters. Throughout this thesis I use Equation 1.4 to compute all distances in conjunction with the standard cosmology defined as: $\mathrm{H_0} = 70\mathrm{Km\,s^{-1}\,Mpc^{-1}}$, $\omega_M = 0.3$, $\omega_\Lambda =$

$$D_L = (1+z) \times \frac{c}{H_0} \int_0^z \frac{dz}{\sqrt{(1+z)^3\omega_M + \omega_\Lambda}} \tag{1.4}$$

1.5 Thesis overview

The overarching goal of this thesis is to demonstrate our ability to photometrically select SLSNe amongst the samples of transients detected by large astronomical surveys, focusing on the detection of the most distant objects of the class. This thesis is laid out as follows:

In Chapter 2, I introduce the surveys and other auxiliary data sources used in this thesis. I also present the sample of spectroscopically confirmed SLSN from Dark Energy Survey and introduce a sample of literature objects used as templates for their class. Following from this, Chapter 3 describes a number of techniques and analytical frameworks, as well as packages designed to study and simulate artificial samples of both SLSNe and CCSNe. As part of this, I introduce the spin-down of the magnetar model, in the context of modelling the light curves of SLSNe, as well as a technique for enhancing the blackbody approximation of the SLSN SED to account for a number of absorption features commonly associated with this class.

Chapter 4 builds upon the models and techniques developed in Chapter 3 to produce a definition of SLSN in the context of the spin-down of a magnetar model. This is then applied to the archival SNLS data identifying one, previously unclassified SLSN. Together with the sample of additional two, spectroscopically confirmed object, they formed the base for a calculation of the rate of SLSN at z$\sim$1.

In Chapter 5, I discuss the possibility and the drawbacks of using a similar technique to detect SLSN in DES. Upon demonstrating that a novel Machine Learning approach is required, I discuss the development of artificial samples of SN light curves of all common classes as well as AGN and spurious survey noise, before applying it as a training sample for a Convolutional Neural Network powered photometric SN classifier. This model is then applied to the sample of real DES transients, first producing a pure sample of SNe before identifying a sample of potential SLSN candidates.

I then analyse this sample, shown to suffer from contamination with SNIIP, to purify it and select the strongest SLSN candidates. The observation properties of the sample are then briefly analysed before discussing its implications on the study of high redshift SLSNe. Finally, Chapter 6 summarises this thesis, highlights and concluding all the major finding as well as provides a forward look at what new surveys, such as LSST, will bring to the field of SLSNe.

Chapter 2

Data

xkcd.com/1231

This thesis focuses on the study and searches for SLSNe in the Supernova Legacy Survey (SNLS) and the Dark Energy Survey (DES). Before I discuss the methods and results in the forthcoming chapters, I will first introduce the surveys as well as the data they obtained. This includes their designs, cadences, transient detection pipelines, SN follow-up programs and facilities, as well as their general properties and trends. While the data for both surveys is not used in a joint analysis in this thesis, it is nevertheless beneficial to discuss together. For both historical and practical reasons these surveys show many commonalities with DES learning and improving on the work done by SNLS a decade earlier. This mirrors the work in this thesis where, based on the study of SLSNe in SNLS, I have learned and improved many techniques for searching and modelling these objects before applying them to DES.

Further to describing the sources of the data used in this work, I also provide an overview of the SLSNe discovered by both surveys. However, this includes only the objects that were identified independently of the searches described in this thesis. This is also an opportunity to discuss the literature sample of SLSNe that played a pivotal work in forming a training sample, and subsequently defining, SLSNe.

In this chapter, I begin by discussing the SNLS, used in the early parts of this thesis, as the source of data for my work on the rate of SLSNe at z∼1, discussed in Chapter 4. Following this, I discuss DES which provided a larger and higher redshift sample of transients used in my search for high redshift SLSNe as described in Chapter 5. I then outline the spectroscopically confirmed sample of SLSNe used as the ground truth sample for comparison to the sample presented in Chapter 5. I also give an overview of the SUDSS survey, which provided some auxiliary data for the DES SLSN sample. Throughout the chapter, I describe the follow-up facilities used in the classifying of SLSNe, both those discovered during the real-time search in SNLS as well as the objects that were targeted using the selection techniques discussed in Chapter 5 within DES. Finally, I describe the process of collecting and unifying the sample of published SLSNe used as our base training dataset.

2.1 Supernova Legacy Survey

The Supernova Legacy Survey (Boulade et al., 2003; Pritchet & Collaboration, 2004) was run as part of the Canada-France-Hawaii Telescope Legacy Survey (CFHT-LS) between 2003 and 2008. Over this time, it was proven to be one of the most successful SN surveys to date, observing thousands of transients and spectroscopically confirming a large proportion of them. This includes over 300 SN-Ia (Perrett et al., 2010), more than 50 core-collapse supernovae and the measurement of their respective rates (Perrett et al., 2012; Bazin et al., 2009). SNLS has also discovered two SLSNe at z =1.588 and z=1.50 (Howell et al., 2013), which, until recently, have been the highest redshift spectroscopically identified objects of this class. The principal objective of the survey was to perform a measurement of the cosmological constants ω_Λ and ω_m (Astier et al., 2006). This was extremely successful, producing the most precise ground-based measurement of its time (Sullivan et al., 2011). This was in large part possible due to the observing strategy optimized to maximize the number of high redshifts SN-Ia candidates and the thorough spectroscopic follow-up program (Bronder et al., 2007), which gave much stronger constraints for the Hubble diagram thanks to the high redshift leverage not possible before with the low redshift SN-Ia surveys.

2.1.1 Survey Overview

SNLS used the 4m CFHT situated on Mauna Kea, Hawaii. It was operated by teams from Canada and France as part of the CFHT Legacy Survey that composed of a small area, deep SN survey and a shallow, wide galaxy survey aimed at studying the large-scale structure of the Universe as well as the cosmological parameters through galaxy clustering and weak lensing (Pritchet & Collaboration, 2004; Astier et al., 2006). Four deep fields of $\sim$1 deg^2 have been observed to the limiting magnitude of m $\sim$24.5 using the 400-megapixel MegaCam camera (Boulade et al., 2003). Observations took place over five seasons, each lasting approximately 5 months. In total, 202 nights were allocated to the survey (Pritchet & Collaboration, 2004).

2.1.2 Cadence and Observations

SNLS carried out the observations in the *griz* photometric bands, similar in bandpass to the filters used in SDSS (Figure 2.1). Each field was observed over five to seven periods, each lasting approximately 18 days during the lunar dark times, with an average cadence of 3-4 days (Astier et al., 2006; Guy et al., 2010). Where the weather conditions allowed, all bands were . The quality criteria required the light curves to have two detections before and two detections after the maximum light of the SN, which the cadence used by SNLS was well suited for. In cases where the observing plan could not be fully executed, due to weather condition or otherwise, the r and i band observations have been prioritized over the g and z band observations (Guy et al., 2010). This meant that even during the early commissioning stages of the survey or suboptimal weather conditions, the quality of the light curves remained sufficient enough for SN-Ia analysis. However, this had a large effect on the g-band data in the later stages of the season where the data is often missing due to a shorted observing window where the field was visible. This had an effect on the analysis of the much bluer, in comparison to SN-Ia, SLSN in the sample (Prajs et al., 2016).

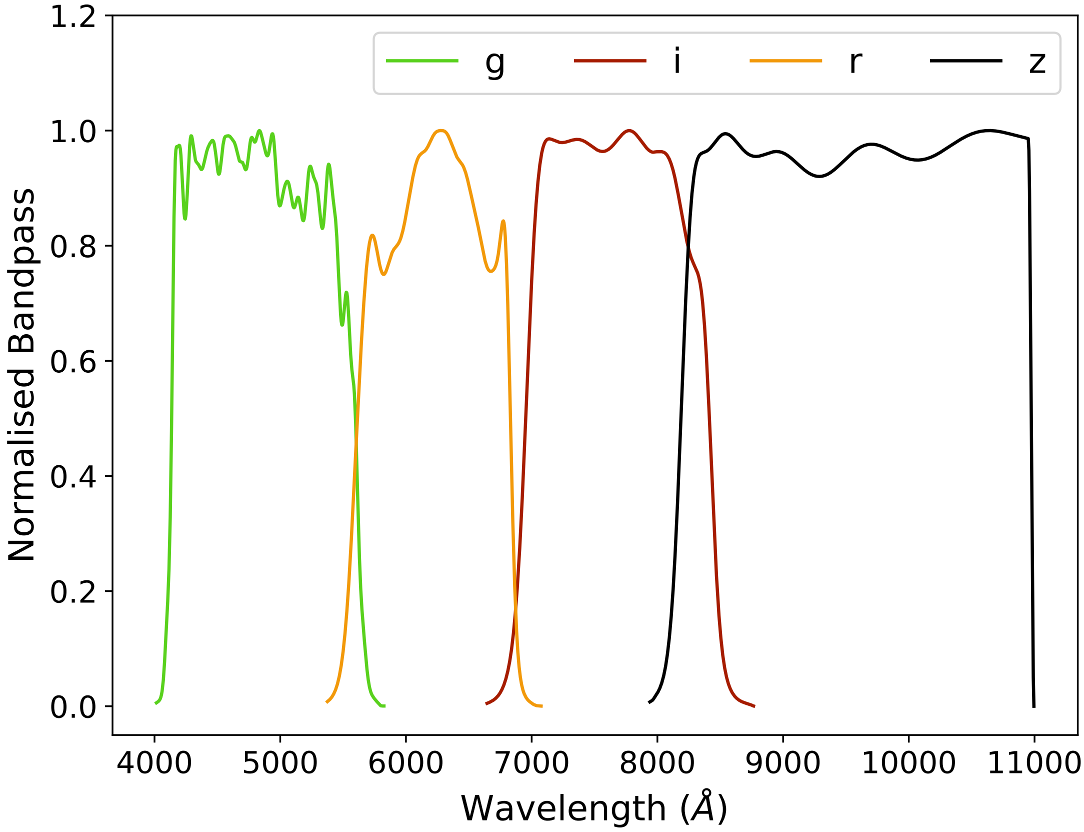

FIGURE 2.1: Bandpass response for filters used in SNLS.

2.1.3 Data Reduction

Several different data reduction pipelines have been used in the analysis of the SNLS data. In this thesis, we used a combination of data prepared for public and internal data releases. We have also reanalysed the data for some objects of interest using PTFPhot, a custom, a pre-existing pipeline designed to improve the data reduction quality for faint sources (Firth et al., 2015).

2.1.3.1 Real-time photometry

During the live operations of the survey, the data pre-processed by applying flats and biases using the ELIXIR pipeline (Magnier & Cuillandre, 2004). The data were independently analysed by the French and Canadian teams using separate quick-reduction pipelines (Astier et al., 2006; Bazin et al., 2011). Both teams aimed to produce lists of new, viable SN candidates within hours of their observations before sending them to the spectroscopic follow-up facilities. Both teams were very successful and produced mostly identical lists which lead to high classification accuracy, largely contributing to the overall success of the survey (Pritchet & Collaboration, 2004).

2.1.3.2 Forced photometry

The quick reduction pipelines used in the detection of objects were optimized with speed, as opposed to accuracy, in mind. Any scientific analysis of the data requires a more precise treatment of the photometry. The data for 'real' transient, defined as having detections on multiple epochs and in multiple bands, was passed through an early version of PTFPhot (Firth et al., 2015): a much improved, custom, forced photometry pipeline. The improvements in the photometry, compared to the quick photometry, come mainly from the treatment of the PSF of the images. The quality of the science images is measured precisely on a number of stars, allowing for the reference images, usually with better quality, to be downgraded to match the quality of the science frames by convolving them with the PSF. Furthermore, the photometry is measured at the centroid of the source, as determined in image stacks as opposed to individual frames, giving rise to the term 'forced' photometry as the positions of the objects are forced to be consistent between all images. The full treatment of the PSF decreases the uncertainties associated with the flux measurement, especially for faint sources close to, or below, the detection limit. This analysis has been applied to the data releases that provided the sources and light curves for the work described in Chapter 4 in a similar way to other SNLS analysis such as the rates of SN-Ia (Perrett et al., 2012) and core-collapse SN (Bazin et al., 2009), as well as the cosmological measurements (Astier et al., 2006; Sullivan et al., 2011).

2.1.4 Spectroscopic Follow-Up

The success of SNLS cannot be attributed only to the number of transients discovered by the survey, but also to the effort behind the spectroscopic follow-up of the candidates. Between the Very Large Telescope (VLT), Keck, Gemini North and South and Magellan, more time has been allocated for spectroscopic follow-up than the time allocated to the photometric survey alone (Pritchet & Collaboration, 2004). As a result, 322 SN-Ia have been spectroscopically confirmed along with 51 CCSN and two SLSNe (Guy et al., 2010; Howell et al., 2005, 2013). A large number of the SN confirmed by the survey have been classified before or at their maximum thanks to both the follow-up selection criteria, which correctly identified the most promising candidates (Sullivan et al., 2006), and the readiness of the survey to sacrifice the classification rate in order to improve the quality of the data. While a large number of CCSN and AGN have been targeted for follow-up, which perhaps in the eyes of the primary goal of SNLS could be considered as undesired contaminants, this process also leads to the accidental discovery of two high redshift SLSN. These objects would be almost certainly overlooked if they were targeted post-peak as their evolution would have strongly disfavoured them as SN-Ia candidates.

In turn, the rapid follow-up of SNLS06D4eu has produced a spectrum at a rest-frame phase of -34 days, which remains to this day as one of the earliest spectra of a SLSN.

2.1.5 Redshift measurements

Distance measurements are invaluable in any type of SN analysis beyond just their application in cosmology. SNLS has provided three types of redshift measurements, used as distance probes: SN spectroscopic redshift, host galaxy spectroscopic redshift and photometric redshift estimates. The case of the SN spectroscopic redshift is the most accurate and rarely disputable as lines used to identify the redshift can be confirmed in the raw spectrographic images to be coincidental with the trace of the SN light. In SNLS this was measured for all classified SN (Howell et al., 2005; Bronder et al., 2007; Ellis et al., 2008; Balland et al., 2009). Furthermore, it may sometimes be possible to measure the redshift of an object that has an ambiguous classification as some spectral features may be strong enough to be detectable despite low SN of the continuum.

Similarly, to the SN spectroscopy, the host spectroscopy can provide a very high accuracy measurement of the redshift using narrow spectral features. However, it is possible that the host of the object may be misidentified. For example, the redshift might be measured for a bright galaxy apparently coincidental with the SN while the true host was a background galaxy or a dwarf foreground galaxy. Since these errors are relatively rare, we use both the target and host spectroscopic redshifts as absolute. SNLS, similarly to other large SN surveys, was not able to target all potential SN candidates during the live operations of the survey with many unclassified objects, later photometrically selected as good SN candidates after they faded below the detection limit. Lidman et al. (2012) used the AAOmega multi-fibre spectrograph on the Anglo-Australian Telescope (AAT) to target nearly 700 hosts of SN candidates in two of the four SNLS fields, obtaining redshift for 400 of them. Other, similar catalogues were created, including Lilly et al. (2007); Le Fèvre et al. (2013)

Beyond the spectroscopic measurement, it is also possible to estimate the redshift using the photometry of the galaxies. The SED of a galaxy usually contains a characteristic sharp break at ∼4000Å which can be observed to transition between filters as a function of redshift. This is a very powerful technique which, when used with a number of photometric filters, can very accurately estimate the redshift of a galaxy for $z>0.3$. Below that threshold, the SED break is contained within a single filter largely increasing the uncertainty of the estimate (Connolly et al., 1995). This technique has been used to estimate redshifts for over 500,000 galaxies within the CFHTLS, which overlapped with the SNLS fields giving a redshift estimate to nearly all candidates with a host magnitude of $M_i < 25$ giving a median redshift uncertainty of $\delta z = 0.1$ (Ilbert et al., 2006).

2.1.6 SLSN in SNLS Light Curves

As a survey designed with a heavy focus on SN-Ia, SNLS was not an ideal for detecting SLSN or other transients with relatively peculiar evolution. Its small area and relatively dense cadence meant that the volume searched was not sufficient to the detect a large number of SLSN, known to be a very rare class of astronomical events (Cooke et al., 2012; Prajs et al., 2016; Quimby et al., 2013). It is therefore perhaps not a coincidence that the only two objects spectroscopically confirmed by the survey were found at z=1.50 and z=1.588 where the survey was searching a much greater volume.

Beyond the nominal, live survey, the images for individual SNLS seasons have been co-added together to create "super" stacks, reaching a detection magnitude of m=26.5 (Cooke et al., 2012). A further two SLSN candidates have been detected using this technique. Their light curve behaviours were similar to that of a SLSN in terms of the absolute luminosity and temporal evolution. While it was impossible at that point (several years after the explosion time of the SN) to spectroscopically identify these objects, host galaxy spectroscopy was obtained for both objects determining redshifts of z=2.05 and z=3.9 (Cooke et al., 2012), confirming that these transients had luminosities comparable to that of SLSN. While these candidate SLSNe shows an interesting precedent for what may be hiding beyond the reach of our current 4m telescope class optical surveys, they were not used in any projects within this thesis. The lack of certain confirmation, low cadence in the stacked images light curve and the difference in the detection technique used deemed these objects incompatible with other SLSN data sources (Prajs et al., 2016).

2.2 Dark Energy Survey

The Dark Energy Survey (DES) is the largest cosmology survey operated to date. It is composed of two elements; a wide galaxy survey and a SN component. Its main aim is to perform the most precise to date measurement of the cosmological parameters. Many features and components of DES have been borrowed and improved on from previous surveys including SDSS and SNLS.

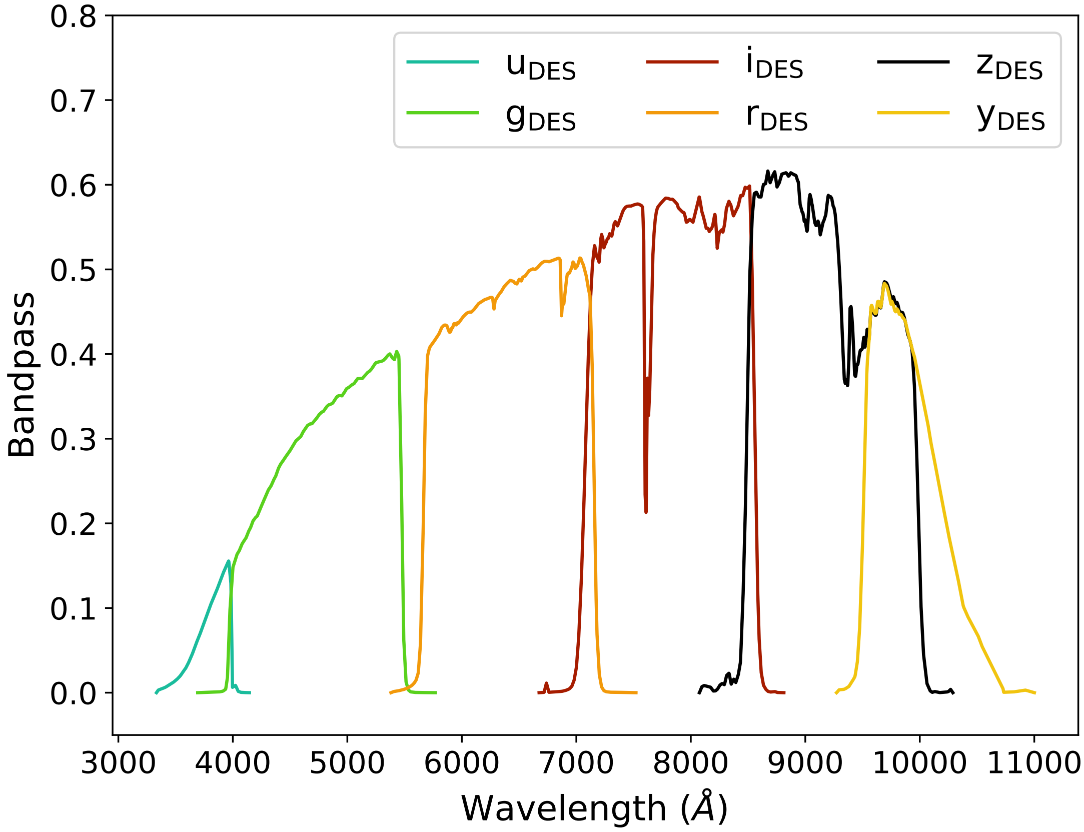

FIGURE 2.2: Bandpass response for filters used in DES.

2.2.1 Survey Setup

DES uses a purpose-built, 570 mega-pixel DECam CCD camera (DePoy et al., 2008; Flaugher et al., 2015) mounted on the 4m Blanco telescope at the Cerro-Tollolo observatory in Chile. One of the greatest advantages of DECam over its predecessors is its high sensitivity at red wavelengths allowing for the high signal-to-noise (SN) observations in z and y bands compared to other surveys, allowing for SN detections at high redshift (Figure 2.2). DES was awarded 500 observing nights over the period of 5 years between 2013 and 2018 (Dark Energy Survey Collaboration et al., 2016). While the SN component has come to an end at the end of the fifth season as originally planned, the DES wide field component has been awarded more time to make up for the time lost due to unusually bad weather conditions in Chile over the last few years. Each season of observations started in late August and continued through to the end of January giving an average length of 5 months.

2.2.1.1 Wide Survey

DES wide survey has been designed to observe 5000 deg^2 of the southern sky to the depth of m$\sim$25 in the *ugrizy* filters. The aim of this is to create the largest catalogue of galaxies and their associated redshifts to date at an unprecedented resolution and depth for a ground-based survey, with the first public data release contained a catalogue of 400 million galaxies from the initial 3 years of the survey (Abbott et al., 2018). These data can be used to study cosmology via three separate experiments; the Baryon Acoustic Oscillations (BYO), Galaxy Clustering and Weak Lensing (Dark Energy Survey Collaboration et al., 2016; Prat et al., 2017; Drlica-Wagner et al., 2017; DES Collaboration et al., 2017).

2.2.1.2 Supernova Survey

The goal of the DES SN search is to produce the largest, homogeneous catalogue of SN-Ia to date. To achieve this, 10 observing fields have been selected are observed in the *griz* photometric bands with an average cadence of $\sim$5 days. Eight of these fields are 'shallow' and observe to the depth of m=23.5 while two fields have been chosen to be 'deep' and observe to m=25. The number of deep and shallow fields was chosen such as to maximize the number of discovered SN-Ia while still allowing for a sufficient number of high redshift objects to be detected (Bernstein et al., 2012).

2.2.2 Data Reduction

While the basic structure and principles behind the data reduction in DES are very similar to that of SNLS, the major differences lay in the treatment of transient detection in the difference images. As the volume of data in DES was too large to allow for manual selection of real sources as a long-term solution. A manual classification was performed only in the first year of the survey operation. This dataset was then used as a training sample for machine learning classification pipeline, AUTOSCAN Goldstein et al. (2015).

Thanks to a large number of computing resources available to the survey the computationally expensive force photometry has been automatically performed on every transient candidate, defines as an object with at least three detections in a minimum of two different bands where the detections were within 30 days but not all on the same night.

2.2.3 Spectroscopic redshift

One of the biggest differences in the design of DES versus other SN Ia surveys is its approach to redshift measurements.

2.2.3.1 Host galaxy redshift

From the predicted number of objects to be detected by DES, it was clear, since the early planning stages, that it would be impossible to obtain spectroscopic redshift using the SN spectra for all the candidates. The survey, therefore, focused on obtaining the spectroscopic redshift of the host galaxy for all objects. This is being achieved in collaboration with OzDES, an Australian survey using the AAOmega multi-fibre spectrograph mounted on the AAT telescope dedicated to spectroscopic follow-up of DES SN fields. All real transients are targeted regardless of the brightness of their host as the target is observed multiple times over the duration of the survey and the spectra are stacked. Is some cases redshift has been measured in galaxies down to r=24.5. Furthermore, DES SN fields were purposely selected to overlap with other surveys in order to provide a catalogue of redshifts for galaxies in the fields. This included Chandra Deep Field South (CDF-S), European Large Area ISO Survey (ELAIS), XMM Large Scale Structure survey (XMM-LSS) as well as SNLS and the SDSS Stripe82 regions.

2.2.3.2 Hostless SN

While redshifts for the majority of SNe can be obtained from their hosts, there remain some that are associated with galaxies fainter than the detection limit of even the stacked AAT spectra. For these objects, it is critical that the redshifts are measured during the live transient which has been the main focus of the extensive spectroscopic campaign. A number of facilities including VLT, Keck, Magellan, MMT, SALT SOAR and NTT amongst others have been used. 251 SN Ia have been classified along with 61 CCSN and 18 SLSNe. A short description and circumstances involving the classification of DES SLSN are described in Section 2.2.5

2.2.4 Photometric Redshifts

All experiments that form part of DES rely heavily on photometric redshift measurements making it an integral part of the survey. The wide component uses the measurement as a base for their cosmological measurements as it is currently impossible to measure spectroscopic redshifts for even a fraction of the nearly half a billion galaxies detected by DES. The SN survey used the measurements as redshift priors in transient classification. These fits are not used for cosmology, instead, they act as a prioritizing tool for the spectroscopic follow-up program. Photometric redshifts have also been used as part of the SLSN search. While most SLSNe would be expected to have a faint or no host associated with them thanks to their common association with dwarf galaxies, we have used the photometric information (also the lack of it) as a possible sign that an object may be a SLSN, e.g. in cases where the galaxy was measured to be too local or where there was no photometric redshift present meaning that the object can be considered as 'hostless'. This is described in more detail in Chapter 5.

2.2.5 SLSNe in DES

While SLSNe have never been a primary target of DES, their potential use as cosmological probes (Inserra & Smartt, 2014) meant that they have generated a large interest within the survey. The first SLSN, and the only one detected in the first season of the survey, DES13S2cmm has been classified using a Directors Discretionary Time (DTT) program at the VLT and was published as one of the earliest results from DES (Papadopoulos et al., 2015). In the following seasons, the number of objects discovered has increased dramatically with ∼6 objects confirmed per year, giving motivation to the photometric search for the missing SLSN in the data performed in this thesis. The sample (Angus et al. in prep), has shown a large diversity of the objects with many falling outside of the 'classical' definition of a SLSN (Inserra et al., 2018). I briefly outline the spectroscopic sample from the first four years of DES and its interesting properties as well as any peculiarities in the light curve or spectral evolution in the context of their modelling and comparisons with the photometric sample of SLSN described in Chapter 5. The sample is summarized in Table 2.1

2.2.5.1 DES13S2cmm

DES13S2cmm was the first SLSN discovered by DES. It was identified during a visual light curve scan and quickly selected as a potential SLSN candidate due to its particularly long rise and faint host. A spectrum of the SN has been obtained with the VLT/FORS2 using a DDT program. The observation confirmed that the SN is at z=0.609 and has features comparable to a SLSNe. At the time of discovery, this was one of the lowest luminosity SLSNe at M_u=-19.9.

Table 2.1: Summary of the DES spectroscopic sample of SLSNe.

Name	Redshift	Peak M_u	RA	DEC	Reference
DES13S2cmm	0.663	-19.9	02:42:32.83	-01:21:30.1	Papadopoulos et al. (2015)
DES14C1fi	1.4	-21.9	03:33:49.80	-27:03:31.6	Angus et al. (in Prep.)
DES14C1rhg	0.481	-19.2	03:38:07.27	-27:42:45.7	Angus et al. (in Prep.)
DES14E2slp	0.57	-20.5	00:33:04.08	-44:11:42.8	Angus et al. (in Prep.)
DES14S2qri	1.5	-21.6	02:43:32.14	-01:07:34.2	Angus et al. (in Prep.)
DES14X2byo	0.869	-21.6	02:23:46.93	-06:08:12.3	Angus et al. (in Prep.)
DES14X3taz	0.608	-21.6	02:28:04.46	-04:05:12.7	Smith et al. (2015)
DES15C3hav	0.39	-19.1	03:31:52.17	-28:15:09.5	Angus et al. (in Prep.)
DES15E2mlf	1.86	-22.1	00:41:33.40	-43:27:17.2	Pan et al. (2017)
DES15S1nog	0.565	-20.0	02:52:14.98	-00:44:36.3	Angus et al. (in Prep.)
DES15S2nr	0.22	-20.0	02:40:44.62	-00:53:26.4	Angus et al. (in Prep.)
DES15X1noe	1.188	-22.5	02:14:41.93	-04:52:54.5	Angus et al. (in Prep.)
DES15X3hm	0.86	-21.8	02:26:54.96	-05:03:38.0	Angus et al. (in Prep.)
DES16C2aix	1.07	-20.6	03:40:41.17	-29:22:48.4	Angus et al. (in Prep.)
DES16C2nm	1.998	-22.3	03:40:14.83	-29:05:53.5	Smith et al. (2018)
DES16C3cv	0.727	-20.7	03:40:14.83	-29:05:53.5	Angus et al. (in Prep.)
DES16C3dmp	0.526	-20.5	03:31:28.35	-28:32:28.3	Angus et al. (in Prep.)
DES16C3ggu	0.95	-21.4	03:31:12.00	-28:34:38.7	Angus et al. (in Prep.)

2.2.5.2 DES14C1fi

DES14C1fi was similarly identified as a plausible candidate using a manual search due to its slow evolution. It was observed at the Keck telescope and again, 7 days later, using VLT/XShooter, which found a featureless continuum that was a very good match to a blackbody SED. A 3728Å oxygen emission doublet was used to identify the redshift as z=1.30 giving it a luminosity of M_u = -21.9. While this result is somewhat tentative due to a very low SN in the IR arm of XShooter there is a possible sign of a broad H-α feature. DES14C1fi is the only SLSN in the DES sample that shows potential signs of being a SLSN-II candidate in the first four seasons.

2.2.5.3 DES14C1rhg

DES14C1rhg was targeted as a hostless SLSN candidate based on its long rise time of 30 days. It was observed using our VLT/XShooter SLSN program and confirmed at z=0.47 putting it at a lower than expected redshift for a SLSN of that apparent magnitude and giving it a luminosity of M_u = -19.2. Combining its low brightness with a relatively fast decline time puts DES14C1rhg on the extreme of the population, making it incompatible with any current photometric definition of a SLSN despite its spectroscopic resemblance. DES14C1rhg gave us the first indication that the DES sample is able to identify objects in the gap between SLSN and SN Ic.

2.2.5.4 DES14E2slp

DES14E2slp was detected at a very late stage of the season with only a single epoch of observations after maximum light. It was selected as a target for the VLT/XShooter program due to being blue, hostless and relatively slowly rising. The classification spectrum was obtained at a phase of ∼-20days and showed a blue, featureless continuum despite a relatively high SN. A spectroscopic redshift was measured using a weak absorption feature to be z=0.64, placing the object a luminosity of M_u = -20.5. With the inconclusive spectroscopic redshift, no decline data and no spectral features this remains the most tentatively confirmed SLSN in our sample.

2.2.5.5 DES14S2qri

DES14S2qri is the most peculiar SLSN detected in the second season of DES. It was targeted for follow-up as a hostless object with a long rise in the redder bands. Its spectrum perfectly matches that of a SLSN at z=1.5 making it the highest redshift SN found up to that point of the survey. More interestingly, it featured some of the most unusual behaviours in the observer frame *g*-band where the object is not detected until the maximum light in the *i*-band. Magnetar modelling of the light curve shows that the *g*-band underwent very strong absorption in the early stages before returning to the expected SED. Unfortunately, the classification spectrum was taken too late to observe this behaviour.

2.2.5.6 DES14X3taz

DES14X3taz was the second SLSN published as part of DES and is one of the most important objects of this class discovered to date as it is the most well-observed example of a pre-maximum 'bumps' in a SLSN. It was initially misidentified as a potential SN Ia during the 'bump' phase but never targeted at that stage until, during a manual scan of the light curves, it was observed to be rising again. The spectrum taken pre-peak has confirmed the object to be a perfect match to a SLSN at z=0.608. Further discussion of the modelling of this object can be found in Chapter 3 where we model this object using a combination of the Magnetar model and ejecta spreading inside of a dense, extended wind envelope (Piro, 2015).

2.2.5.7 DES14X2byo

DES14X2byo was first identified due to its long rise and colour with subsequent spectroscopic follow-up confirming it to be a SLSN at z=0.86 with a peak luminosity of M_u=-21.5. Despite its average spectrum, evolution and peak luminosity, DES14X2byo is one of the bluest SLSNe ever discover reaching a photospheric temperature of 27,000K. One possible suggestion is that a pre-peak event like the one seen in DES14X3taz took place at the same time as the onset of the spin-down of the central engine injecting extra energy which thermalized to produce the excess temperature.

2.2.5.8 DES15C3hav

In a sample full of what one could describe as peculiar SLSNe, DES15C3hav stands out as one of the deepest mysteries the field has to offer. The object was discovered in the latter stages of the third DES season and was targeted as an early SN Ia using a dedicated program at the MMT due to its light curve behaviour. It was then identified as a SLSN at z=0.39 giving it a peak magnitude of M_u=-19.1, making it the least luminous example of its class. It wasn't until after its classification that we discovered that the SN was associated with a pre-peak bump. While this would normally not be considered unusual, the bump was observed to have a peak luminosity of M_u=-16 (nearly 3 magnitudes dimmer than any previous example), relatively red with a peak temperature of 6,500K and consistent with an explosion before the start of the season giving it a rise time of >50 days. These three characteristics are in strong contradiction to what we grew to expect similar events to look like.

2.2.5.9 DES15E2mlf

DES15E2mlf was the third individual SLSN published by DES (Pan et al., 2017). Upon discovery, the object was matched with a SN Ia model showing an excellent fit at z$\sim$0.3. The object was simultaneously associated with a bright and blue compact galaxy with a photometric redshift perfectly matching that of the SN Ia fit. DES15E2mlf was, therefore, a seemingly ideal target for a young, nearby SN Ia program. However, the obtained spectrum wasn't that of a SN Ia but a SLSN at z=1.86, making it the highest redshift confirmed SLSN at the time. Later analysis showed that the host galaxy, whilst larger than those normally associated with SLSN at low redshift, was consistent with an extremely star-forming galaxy giving it its excess UV flux. As the first truly high redshift SLSN in DES, DES15E2mlf informed us of the what we can expect an object of similar distance to appear as and helped us modify our approach to searching for SLSN.

2.2.5.10 DES15S1nog

DES15S1nog is another example of a SLSN discovered accidentally in DES when targeting the object under a SN Ia program. While the classification spectrum is mostly featureless, galaxy emission features place the object at z=0.565 giving it a peak luminosity of M_u=-20. Furthermore, the slow rise time of ∼30 days makes it a viable SLSN candidate.

2.2.5.11 DES15S2nr

DES15S2nr was first detected on the second epoch of observations of the third DES season and was selected as a SLSN candidate using our magnetar model selection technique described in Chapter 3. The SN was quickly identified to be an example an undulating SLSN with a very fast initial pre-peak ‘bump’ followed by a very slow rise and decline that lasted the full duration of a DES season. We obtained a series of spectroscopic follow-up observations placing the object at z=0.22, giving it a peak magnitude of M_u=-20. DES15S2nr contains the best photometric and spectroscopic dataset of any SLSN in our sample due to its distance and robust follow-up campaign.

2.2.5.12 DES15X1noe

DES15X1noe is the most luminous and slowly evolving SN in the DES sample. It was targeted as a very slowly rising object and found to be a good match to a SLSN at z=1.188, giving it a peak brightness of M_u=-21.7. The rise time of DES15X1noe is estimated to be rest-frame ∼50days however the value is uncertain as the peak occurred after the end of the third DES season. Interestingly the SN has been very strongly detected throughout most of the following season of data making it the first truly slowly declining SLSN detected by DES.

2.2.5.13 DES15X3hm

DES15X3hm is perhaps one of the most ’ordinary’ SLSNe in our sample. It was first detected several weeks after maximum light and selected for classification based on our magnetar model classification. A follow-up spectrum taken at a rest-frame phase of +20days confirmed the object to be a SLSN at z=0.86. The pre-maximum data was obtained in auxiliary SUDSS observations which allowed us to constrain the time of the maximum as well as its model parameters.

2.2.5.14 DES16C2aix

DES16C2aix was another example of a relatively faint but slowly evolving SLSNe in our sample. It was observed under a peculiar transient program at the GTC due to its long rise time. It was found to be a SLSN at z=1.07 with a peak luminosity of M_u=-20.6. DES16C2aix is a relatively red SN even when accounting for the redshift with no detections in the *g*-band and *r*-band flux below that expected from our magnetar model fits.

2.2.5.15 DES16C2nm

DES16C2nm is the crown jewel in our sample as it is the highest redshift spectroscopically classified SN ever and recently published by Smith et al. (2018). DES16C2nm was detected at the start of the season and followed-up under a peculiar transient program and was subsequently followed by observation from VLT and HST in a number of IR bands with the aiming of reconciling the rest-frame UV spectra with the rest-frame optical. Discovering an object at such high redshift has provided us with a unique opportunity to determine the feasibility of detecting SLSN in DES at even higher redshifts. Smith et al. (2018) found that DES deep-fields should be able to detect objects like DES16C2nm up to z=3.0, which independently confirms our simulations found in Chapter 3 and provided a further motivation for our search for high redshift SLSN Chapter 5.

2.2.5.16 DES16C3cv

DES16C3cv is a very curious case in our sample. Targeted as a peculiar SN using a program on the GTC the redshift was obtained to be z=0.727 and peak magnitude of M_u=-20.7, however further follow-up using the VLT/XShooter, while confirming the redshift, does not appear to match the features expected of a SLSN. Furthermore, the SN contains two, nearly identical in luminosity peaks separated by rest-frame 60 days which is much greater than the delay expected for a SLSN ‘bump’.

2.2.5.17 DES16C3dmp

DES16C3dmp was targeted under our rapidly evolving transients program at the VLT/XShooter and found to be at z=0.526 with the peak magnitude of M_u=-20.5. Despite its relatively low luminosity and fast rise, the object is blue and has a very slow decline time allowing it to be detectable in both season four and five of DES making it another rare example of a slowly declining SLSN.

2.2.5.18 DES16C3ggu

DES16C3ggu was the last SLSN discovered and classified by DES in the fourth season. It was targeted as a fast-rising, blue object under our VLT/XShooter program but was subsequently classified as a SLSN at z=0.95. As the end of the DES observations came before the SN reached its maximum light we can only estimate, based on our magnetar model fitting that the object would reach a peak luminosity of M_u=-21.4.

2.3 SUDSS

The Search Using DECam for Superluminous Supernovae (SUDSS) (PI: Sullivan) was designed as a dedicated SLSN survey working in conjunction with DES. Its aim was to extend the DES observing season from ∼6 months to ∼9 months by observing the fields, even at high airmass, until the observations become impossible due the sun constraints. The motivation behind the survey was the possibility of using SLSNe as a cosmological probe (Inserra & Smartt, 2014). Unfortunately, due to issues with the data quality and reduction, it has never been used as a tool for searching for new SLSN candidates. Instead, SUDSS has greatly enhanced the light curves of some SLSNe discovered by DES and strongly contributed to the analysis of their sample.

2.3.1 Observations and Data Reduction

SUDSS observed 6 fields overlapping with DES with observations carried out using DECam using an identical setup to DES, allowing for the same pre-processing steps to be applied to the data. The data was not directly fed into the DES database nor did it use the force photometry pipeline used by DES for technical reasons. Instead, we reduced the data using a custom PTFPhot pipeline (Firth et al., 2015). For the purpose of unbiased comparison, corresponding DES observations of the SUDSS SLSNe were also reduced using the PTFPhot pipeline.

2.3.2 Cadence and Exposures

SUDSS was designed with the aim of discovering new SLSN candidates at its very heart. It was initially estimated that it will be capable of identifying ∼ 200 SLSN candidates during its operation (Papadopoulos et al., 2015). As SLSNe are a class of slowly evolving SNe, the DES observing cadence was not replicated for SUDSS and instead it was chosen to be approximately two weeks. Due to worse than anticipated weather conditions, many of these nights have been lost to clouds resulting in a final cadence closer to approximately a month. On average three additional observations were made in each field outside of the DES observing season.

A further difference between the DES and SUDSS observing strategies comes in the exposure times used for the observations. As SLSNe are much brighter but rarer events than SN Ia the exposure times did not have to match that of the DES deep fields. The exposure times are in between that of the DES shallow and deep fields allowing for a balance between the number of observed fields and the volume searched that is optimized for SLSN. In practice, the limiting magnitude of SUDSS was similar to that of the DES shallow fields once the unfavourable atmospheric conditions and high air mass have been taken into account.

2.3.3 Findings

As a result of the poor cadence and lower than expected image quality, it was not possible to carry out a dedicated search for SLSN in the SUDSS data alone. Instead, the SUDSS data has been re-purposed as an auxiliary data source for objects already discovered by DES. This has been extremely successful and resulted in a great improvement to the light curves of some of the SLSNe discover by DES. In cases of DES15C3hav and DES15X2hm, we were able to determine the explosion date and hence constrain the rise time of these SNe using the SUDSS data points.

The most significant observations came in form of DES14X3taz where the auxiliary SUDSS data provided the observations of the pivotal rise and peak of this unique ‘bumpy’ SLSN. Without the SUDSS observations, a large proportion of the analysis carried out in (Smith et al., 2015) would not have been possible.

2.4 Literature sample of SLSNe

As SLSNe are still a new and rapidly evolving branch of SN research, the definition has been a subject of debate since their first discovery (Gal-Yam, 2012; Inserra et al., 2013; Nicholl et al., 2014). Recently proposed classification method by Inserra et al. (2018), which involves measuring the peak and colour of the SLSN at peak and 30 days post maximum light, was not available at the time when all projects described in this thesis were undertaken. While the new approach has been used in the DES Machine Learning classification study in Chapter 5, the measurement of the rate of SLSNe in SNLS was performed using our own definition described in Chapter 4. Any attempt at defining a class requires a training sample of examples that inform that definition.

In this thesis, we have collected the data for a large number of literature SLSNe data, published in the years between 2010 and 2016, including their light curves and spectra. This was not limited to objects published in journals, but also included Astronomical Telegrams (ATels) as well as spectra published on the online WISeREP repository (Yaron & Gal-Yam, 2012), producing a list similar to that published by Schulze et al. (2016). It is important to note at this point that in this work we were only interested in hydrogen-poor SLSN, however, we did not distinguish between slowly and rapidly evolving objects (Gal-Yam, 2012; Inserra et al., 2013).

2.4.1 Quality cuts

Many of the objects in this list were of very poor quality containing only a handful of photometric points and single classification spectra with no data for their evolution. Furthermore, the data originated from a variety of sources including PTF, iPTF, SNLS, DES, Pan-STARRS and LSQ amongst others, giving a broad range of photometric bands and systems.

We devised a set of quality cuts to ensure that the objects used in our analysis meet a minimum standard. As most of our analysis, discussed in the forthcoming chapters, depends on fitting blackbodies to the data, we require that the light curve must contain a minimum of three distinct photometric bands. While in the latter modelling we treat such bands independently, for the purpose of the quality cuts we take bands that are derivatives of each other (i.e. R and r) as the same. Furthermore, we make cuts based on the number of epochs observed per band. In order to use models which, depend on the rise and decline time of the supernova, we require that there is a minimum of two photometric points before the peak and two points between the time of maximum light and +30 days. As the SN evolve rapidly in temperature (and hence colour) the bluer bands peak several days before redder bands. We define the peak as the maximum in the band closest to rest-frame SDSS u-band. Table 2.2 shows the final list of 15 SLSN, available at the time, that passed our data quality cuts and have hence been used in Chapter 4 as the base for our definition of SLSNe.

TABLE 2.2: The training sample of SLSNe-I.

SN Name	Redshift	Survey	Reference
PTF12dam	0.108	Palomar Transient Factory	Nicholl et al. (2013)
SN2011ke	0.143	Catalina Real-Time Transient Survey & Palomar Transient Factor	Inserra et al. (2013)
SN2012il	0.175	Pan-STARRS	Lunnan et al. (2013)
SN2010gx	0.230	Palomar Transient Factory	Pastorello et al. (2010)
PTF09cnd	0.258	Palomar Transient Factory	Quimby et al. (2011)
SN2013dg	0.265	Catalina Real-Time Transient Survey	Nicholl et al. (2014)
PS1-11ap	0.524	Pan-STARRS	McCrum et al. (2014b)
DES14X3taz	0.608	Dark Energy Survey	Smith et al. (2015)
PS1-10bzj	0.650	Pan-STARRS	Lunnan et al. (2013)
DES13S2cmm	0.663	Dark Energy Survey	Papadopoulos et al. (2015)
iPTF13ajg	0.741	intermediate Palomar Transient Factory	Vreeswijk et al. (2014)
PS1-10awh	0.909	Pan-STARRS	Chomiuk et al. (2011)
SNLS-07D2bv	1.500	Supernova Legacy Survey	Howell et al. (2013)
SNLS-06D4eu	1.588	Supernova Legacy Survey	Howell et al. (2013)

2.4.2 Converting and converging photometric systems

The magnitude scale is not optimal for model fitting. Due to being logarithmic in nature, the photometric uncertainties, originally measured in the linear count space and Gaussian in nature, become asymmetric and therefore more difficult to use within the model fitting. It is easier to simply apply a conversion from the magnitudes, M, to flux, ν using a zero point, zp, for a given filter. We have also set an arbitrary error floor of 0.03 magnitudes for all photometric points to account for possible systematic uncertainties that were not included in the published data:

$$f_\nu = 10^{-0.4 \times M \, + \, zp} \tag{2.1}$$

similarly, we convert the uncertainties in magnitude to flux using (2.2).

$$\Delta f_\nu = 0.921034 \, \times \, 10^{-0.4 \times M \, + \, zp} \, \times \, \Delta M \tag{2.2}$$

It is customary to quote the magnitudes for the SDSS-like filters ($ugrizy$) in the AB photometric system and the Johnson filters ($UBVRIJHK$) in the Vega system. If not stated otherwise it was also assumed that the photometry has been corrected for Milky Way extinction as is standard procedure in most modern surveys.

Chapter 3

Techniques

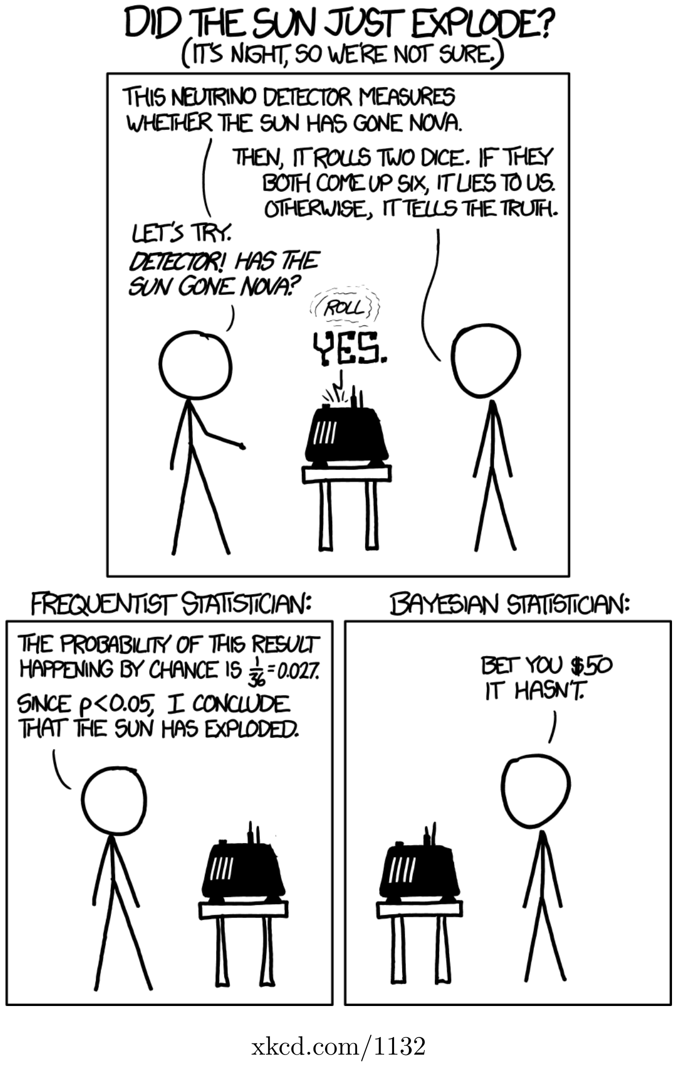

xkcd.com/1132

Throughout this thesis, my goals were to identify SLSNe in a number of surveys. I have approached this problem using a number of tools and techniques, each playing an important role in achieving this goal. The aim of this chapter is to provide an overview of the methods used in this work. I begin by discussing my approach to the modelling of SLSNe using the popular spin-down of a magnetar model (Section 3.1.3). I describe the model and the improvements I introduced in order to better model the UV region of the SLSN SED. I also describe the fitting routines used in the modelling of SLSNe (and other projects as part of this thesis). While this technique was successful in reproducing the light curves of SLSNe, as well as identifying a new SLSN in the SNLS, it was not robust enough to fully capture the diversity of the SLSN sample and was not sufficient to classify SLSNe by itself. To solve this problem, I followed the increasingly popular approach of applying state-of-the-art Machine Learning (ML) techniques to automate the classification process. The later parts of this chapter focus on the techniques and software developed in order to build the training sample of SNe and other transients required for this study, described in Chapter 5.

The use of ML moves the focus of this work away from understanding the parameter spaces of the SLSN models, or the choice of cuts needed to define them. Instead, I focus on simulating transients and their detectability in DES. This includes SN Ia, hydrogen-poor (SN Ib/c) and rich CCSNe (SN II), SLSNe, AGNs as well as random noise spikes which are the main source of contamination in the data. The models of SN Ia are mature and ready to be deployed in this work (Kessler et al., 2009, 2015) thanks to being used as cosmological probes for over two decades (Riess et al., 1998; Perlmutter et al., 1999). Simulations of CCSNe, however, not driven by similar motivations as SNIa, have not been developed equally extensively, becoming one of the key subjects of this thesis. CCSNe are usually more rapidly evolving and fainter than SNIa, resulting in a significantly smaller sample of well-observed objects. The number of objects with a high-quality spectroscopic follow-up is also much lower in comparison. In recent years, the interest in modelling these objects has increased dramatically with large surveys, such as LSST, requiring samples of fake transients in order to inform the design of their observing strategies. In this chapter, I describe our approach to creating a new set of spectroscopic templates for CCSN as well as simulating them in a number of surveys. This project was built to provide a sample of stripped-envelope CCSNe as part of the LSST photometric light curves classification challenge. However, later I have extended its use to DES in order to create samples of both hydrogen-rich and poor CCSNe.

The last, but perhaps the most important, technique described in this chapter is Gaussian Process Regression (GPR). DES, like other transient surveys, does not support a stable and uniform cadence of observation making the data incompatible with the majority of ML techniques that require evenly sampled data (Lochner et al., 2016). I used GPR as a method for interpolating the light curves using a non-parametric approach which does not introduce any physically motivated biases in the fitting process. This is key to solving the overfitting problem, often encountered when working with relatively small training sample within ML framework.

This chapter is divided in the following way: I begin by describing the methods behind the modelling of SLSNe using the magnetar model as well as the extensions I have introduced alongside the SED corrections in the UV. Next, I discuss the packages and techniques developed in order to model SN Ib/c as well as SNII. Finally, I describe GPR as a non-parametric approach to interpolating light curves.

3.1 Modelling SLSN Light Curves

Throughout this thesis, the modelling of SLSNe light curves plays a pivotal role. The measurement of the rate of SLSNe presented in Chapter 4, as well as the search for SLSNe in DES, described in Chapter 5 uses a definition of SLSNe based on the spin-down of the magnetar model. This choice comes after a simpler model, describing SLSNe using a linearly expanding and cooling photosphere (Howell et al., 2013), was tested but eventually rejected in favour of the magnetar model. I introduce this basic model, including its drawbacks, before I describe the magnetar model. I also outline the improvements introduced to the modelling of the SED of SLSNe.

When modelling light curves of SLSNe there are two independent, but equally important, areas that contribute to the accuracy of the model: the SED of the SN, and its evolution with time. The need to model the SED of a SN could be avoided if we used an approach which purely relied on the bolometric light curves as opposed to multi-band observations. From the implementation point-of-view, these models are easier to use and are common in the literature (Inserra et al., 2013; Papadopoulos et al., 2015; Nicholl et al., 2014). However, they do not consider the colour, along with its evolution, of a SN which provides a very powerful tool for further constraints on the properties of the SNe. It has been previously shown (Chomiuk et al., 2011; Howell et al., 2013; Papadopoulos et al., 2015; Vreeswijk et al., 2014) that the SLSN SED can be accurately approximated, in the visible spectrum, by a slowly evolving blackbody with an addition of their characteristic broad absorption lines of O II. However, this approximation breaks down in the near UV due to the prominent broad absorption features which can be attributed to Mn II, Mg II, Fe II, Fe III, C II, Ca III, Si III, Ti II and Ti III (see Mazzali et al., 2016; De Cia et al., 2017b, for line identifications).

3.1.1 Improving the blackbody approximation

In order to improve the modelling of the SLSN SED, I propose a method of improving the blackbody approximation by superimposing an absorption template onto the simple blackbody SED. In order to derive this template, I use a method similar to that of Vreeswijk et al. (2014) where I fit the Planck function to several featureless, 50$\AA$ wide regions of the spectrum in order to measure the underlying blackbody continuum in the SED, as shown in figure 3.1. The resulting fits show that the absorption relative to the blackbody is low in the regions of $\lambda > 3000\AA$, and increases drastically in the bluer regions of the spectrum.

The time evolution of the spectra appears to be weak in comparison to other SNe, making it possible to approximate the SED at any epoch using the Planck function, where the temperature evolves with time, and a single absorption template is used. The absorption is calculated as a ratio of the observed flux to the continuum blackbody fit. The number of SLSNe with good UV coverage remains small, with only the spectra of iPTF13ajg (Vreeswijk et al., 2014), SCP06F6 (Barbary et al., 2009), SNLS-06D4eu (Howell et al., 2013), DES15E2mlf (Pan et al., 2017), DES16C2nm (Smith et al., 2018) and Gaia16apd (Yan et al., 2017). Due to the observer-frame coverage of their respective spectra, our spectral templates cover a rest-frame wavelength range of ∼1600–3500Å.

3.1.2 Modelling the SED evolution

The ability to describe the SEDs of SLSNe as blackbodies greatly simplify the modelling of its evolution. A model is only required to provide the thermal and radial evolution of the photosphere, therefore removing the need for complex modelling such as radiative transfer or hydrodynamic simulations.

3.1.2.1 Fireball model

Perhaps the simplest approach to modelling the SED evolution is to assume that the SN, with an initial radius R$_0$ and initial temperature T$_0$, expands and cools at a constant rate as seen in Equation 3.1

$$R(t) = R_0 + \dot{R}t \tag{3.1}$$

$$T(t) = T_0 - \dot{T}t \tag{3.2}$$

While this model is not motivated, Howell et al. (2013) showed that it provides a good, first-order approximation to the light-curves of SLSNe. Due to its simplicity, the model

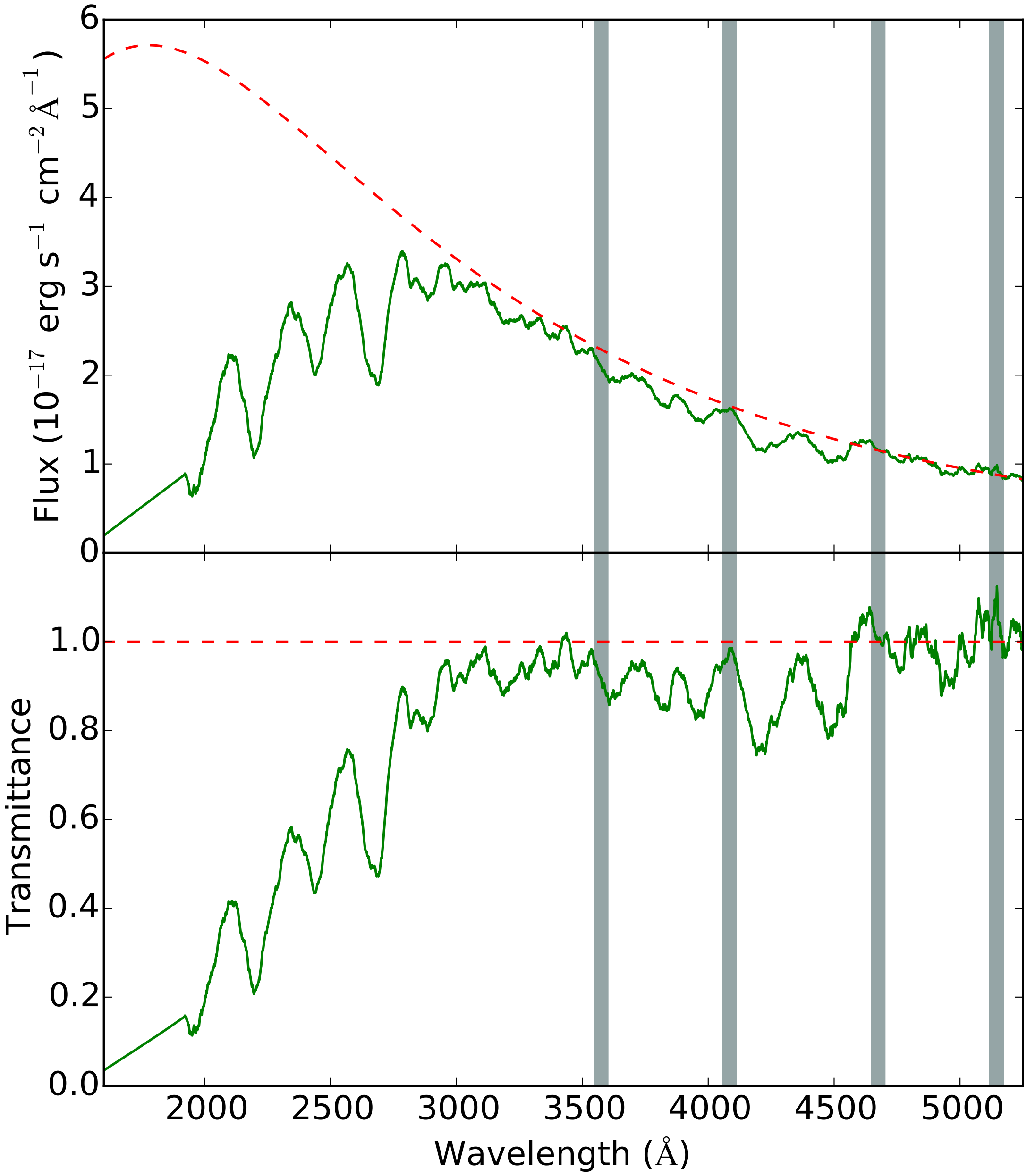

FIGURE 3.1: iPTF13ajg is fitted with the Planck function. The spectrum of iPTF13ajg (green) shows a good agreement with the blackbody (red) at $\lambda > 3000\AA$. At lower wavelengths a strong deviation from the model is observed, highlighting the need for a correction to the model. The ratio between the observed spectrum and the continuum give a measure of the absorption strength as a function of wavelength and can be used in modelling the SLSN SED.

appeared as an attractive prospect for the modelling of SLSN SEDs. However, our testing showed that while it produces a good fit to a SLSN around the maximum light (<+30days) it is not able to capture the slow evolution in the tail of the light curve as seen in Figure 3.2, making it unfavourable in comparison with the more complex magnetar model.

3.1.2.2 Magnetar model

To fully capture the evolution of the SED with time we must employ a model for an engine that provides the late time energy deposition needed to explain the photospheric velocity and temperature observed in SLSNe. While still a matter of active debate in the literature, in recent years the birth and spin-down of a magnetar model have appeared as the strongest candidate to explain these extremely luminous events (Inserra et al., 2013; Nicholl et al., 2013). In this model, SLSNe begin as CCSNe with a magnetar, a rapidly rotating, highly magnetised neutron star, born at its core. As the magnetar spins down due to the interactions , it dissipates its energy in the form of high energy radiation that is then captured by the expanding ejecta and thermalized to produce the observed blackbody SED (Kasen & Bildsten, 2010; Woosley, 2010; Inserra et al., 2013).

I follow the method from Inserra et al. (2013), based on the Arnett law for the energy diffusion through SN ejecta (Arnett, 1982), and the energy radiated by the central engine from Kasen & Bildsten (2010); Woosley (2010). In order to model the bolometric luminosity, L, of a SLSN as a function of time, t, we use equation 3.3:

$$L(t) = 4.9 \times 10^{46}\, e^{-(t/\tau_{\rm m})^2} \delta(t) \int_0^t \frac{2t'}{\tau_{\rm m}^2}\, e^{(t'/\tau_{\rm m})^2}\, \frac{B_{14}^2\, P_{\rm ms}^{-4}}{(1+t'/\tau_{\rm p})^2} dt', \tag{3.3}$$

$$\tau_p = 4.7 B_{14}^{-2} P_{ms}^2 days \tag{3.4}$$

where $\tau_{\rm m}$ is the diffusion timescale, B_{14} is the neutron star magnetic field in units of 10^{14} G, $P_{\rm ms}$ is the magnetar spin period in ms, $\delta(t)$ is the deposition function or trapping coefficient, and $\tau_{\rm p}$ is the magnetar spin-down timescale, is defined in Equation 3.4, inferred from B_{14} and $P_{\rm ms}$.

Physically τ_M is proportional to the ejecta mass(M_{ej}) which is sometimes chosen as the fit parameter instead. The two parameters are related to each other by equation 3.5, where E_k is the explosion energy and κ the opacity of ejecta.

$$M_{ej} = (\frac{\tau_M}{10days})^{4/3} (\frac{\kappa}{0.1cm^2g^{-1}})^{-2/3} (\frac{E_k}{10^{51}erg})^{1/3} M_\odot \tag{3.5}$$

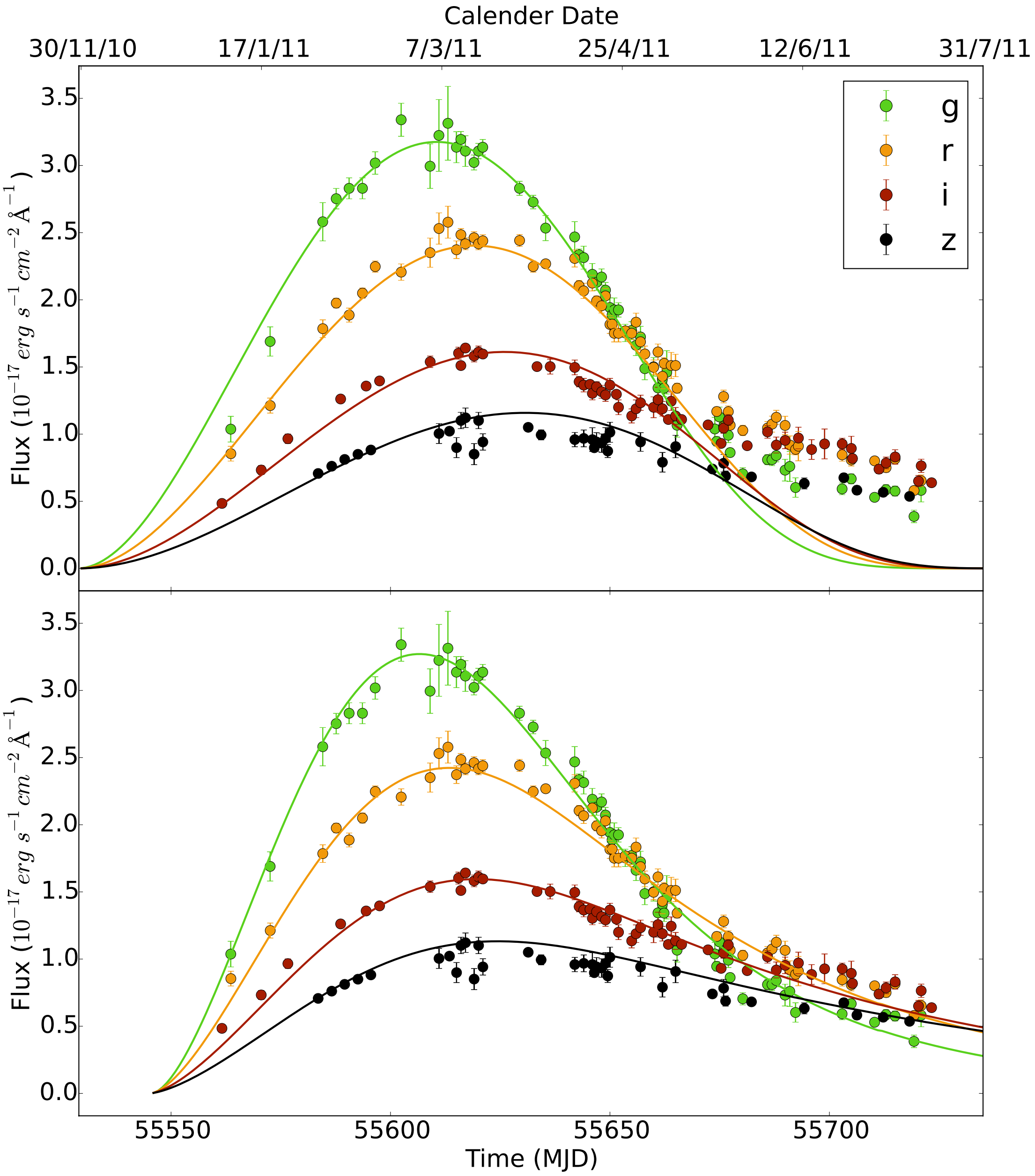

FIGURE 3.2: The SLSN PS1-11ap *griz* light curve (McCrum et al., 2014a) compared to two models describing its photometric evolution. In the upper panel, the model is a simple expanding and cooling blackbody fitted to data around maximum light only, and in the lower panel, the model is our 'absorbed' magnetar model fitted to the entire light curve. In the case of the magnetar model, the spectrum of SNLS-06D4eu (Howell et al., 2013) has been used as an absorption template in the modelling of the SED (see Section 3.1.1). Note that while both models can produce reasonable fits around the peak of the light curve, the black body model is not able to reproduce the characteristic late-time behaviour of SLSNe. Light curve phases are measured with respect to peak brightness in the rest-frame u-band as predicted by our magnetar model fit.

It has been shown (Inserra et al., 2013; Inserra & Smartt, 2014; Nicholl & Smartt, 2016; Papadopoulos et al., 2015) that the opacity and explosion energy parameters have only a weak effect on the quality of fitting and have therefore been fixed as $\kappa = 0.1cm^2g^{-1}$ and $E = 10^{51}$erg respectively.

The velocity of the ejecta, v_{core} is assumed to be constant and can be found using the inferred mass of the ejecta, M_{ej} and its explosion energy. E_{mag} in turn depends on the explosion energy and the energy released by the spin down of the magnetar, shown in Equation 3.7:

$$E_{mag} = 4.9 \times 10^{46} B^2 P^{-4} \tau_P \text{ erg} \tag{3.6}$$

$$E_k = 10^{51} + 0.5 \times E_{mag} \text{ erg} \tag{3.7}$$

$$v_{core} = \sqrt{\frac{10E_k}{3M_{ej}}} \text{ cm s}^{-1} \tag{3.8}$$

Trapping coefficient The trapping coefficient, $\delta(t)$, is defined as the fraction of the high-energy radiation produced by the central engine that gets trapped, and subsequently reproduced as visible light, by the ejecta. It is often assumed in the literature that the trapping coefficient is time-independent and close to unity, implying the full trapping of radiated by the supernova ejecta (Inserra et al., 2013; Papadopoulos et al., 2015; Nicholl & Smartt, 2016). In this work, I use a correction introduced by Wang et al. (2015) with a time-dependent trapping coefficient:

$$\delta(t) = 1 - \exp\left(-\frac{9\kappa \mathrm{M}_{\mathrm{ej}}^2}{40\pi E_k} t^{-2}\right), \tag{3.9}$$

where $\mathrm{M_{ej}}$ is the ejecta mass, E_k is the explosion energy, and κ is the opacity. $\mathrm{M_{ej}}$ is proportional to τ_{m}, E_k and κ (Inserra et al., 2013). We again fix the explosion energy to be $E_k = 10^{51}$ erg and the opacity as $\kappa = 0.1\,\mathrm{cm^2 g^{-1}}$.

Using this time-dependent trapping coefficient improves the late-time fit to the light curve. For a typical SLSN we calculate $\delta \simeq 1$ up to 75 days post-explosion. However, as the ejecta opacity to high energy photons decreases with time we find $\delta \simeq 0.8$ at 150 days post-explosion, emphasising the importance of this correction in the late time light curves.

Deriving Radius and Temperature In its simplest form, the magnetar model only predicts the total radiated energy of the SN and does not make any predictions about the SED of the object. It is therefore most commonly used with bolometric light curves, synthesised from the photometry. Inserra et al. (2013), however, shows that it is possible to predict the photospheric radius of a SN based on this model deriving the following equations:

$$R(t) = r_{core}(t) \left(\frac{\alpha - 1}{\tau_{core}(t)} \right)^{\frac{1}{1-\alpha}} \tag{3.10}$$

while the radius of the photosphere exceeds that of the core ejecta, and; 3.11.

$$R(t) = r_{core}(t) - \frac{1 - \frac{\tau_{core}(t)}{\alpha-1}}{\kappa \rho_{core}(t)} \tag{3.11}$$

when the photosphere recedes into the core. $r_{core}(t)$, $\rho_{core}(t) =$ and $\tau_{core}(t)$ are defined as follows:

$$r_{core}(t) = v_{core} t \tag{3.12}$$

$$\rho_{core}(t) = \frac{3M_{ej}}{4\pi r^3_{core}(t)} \tag{3.13}$$

$$\tau_{core}(t) = \kappa \rho_{core}(t) v_{core} t \tag{3.14}$$

Combining this with the total luminosity and assuming that the object radiates as a uniform, spherical blackbody gives us the photospheric temperature. This can be injected into the Planck law to give an approximation for the SED of a SLSN. This method allows for the magnetar model to be fitted directly to the multi-band photometry without the need to produce the pseudo-bolometric light curves. We combine this with the absorption templates to produce a model of the SLSN spectral evolution as a function of time.

3.1.3 SLAP

Upon establishing an approach for modelling SLSNe it was important to encapsulate it in a software package capable of performing under a number of situations. In this thesis, the magnetar model was used in fitting the light curves of both confirmed SLSNe as well as a variety of transients, the majority of which were not SLSNe and could not be well described using this model. We have also used it to simulate SLSN in SNLS as well as produce an artificial training sample for their search in DES.

The code had to satisfy the following requirements:

- Fit the magnetar model to all literature SLSNe and estimate their parameters.
- Perform a successful fit to any light curve and return an output, regardless of whether it is physical.

- Move the object to any redshift within the detection range of SNLS and DES.
- Allow for the use of any spectral template.
- Allow for extensions and modifications to the magnetar model.
- Simulate SLSN light curves given input model parameters.
- Plot the data and the model, allowing for model comparisons.
- Fit light curves on the time scale of minutes and simulate with sub-second performance.

The performance requirements of the required package were the most difficult requirement to meet. It was based on our need to fit the entire archival sample of transients from SNLS as well as regularly fit the live DES transients with an aim of searching for new SLSN candidates. At an average DES cadence of ∼5 days it was necessary that the fitting is performed at a shorter timescale. Similarly, the studies of the rate of SLSNe Chapter 4 and the ML search for SLSNe Chapter 5 required millions of SLSN light curves to be generated for each iteration of the experiment.

After initially testing the model alongside a number of fitting routines in the PYTHON language environment, I have developed a package that satisfies all of our requirements: The SLSN Light curves Analysis Package (SLAP). Written in a combination of C++, CYTHON and PYTHON, it was utilised in nearly every project undertaken as part of this thesis. The use of C++ and a number of optimisation techniques allowed for a very large performance improvement versus a similar PYTHON package. SLAP performs model fitting in ∼40 s for an average SNLS light curve and simulated a SLSN in ∼10 ms. The package was published as part of my study of the rate of SLSNe in SNLS (Prajs et al., 2016).

3.1.3.1 Code design and structure

SLAP was designed as a modular, reusable and extendable package while at the same time heavily focussing on the run-time performance of the code. I have heavily relied on the concepts of Object Oriented Design and Polymorphism to allow me to implement any required model as an extension of the code. At the core of SLAP I have relied on the approximation that the SED of SLSNe can be described as an absorbed black body. I have defined a virtual MODEL class that acts as a base class defining the methods for calculating SEDs based on the temperature and radii of SNe photospheres. This class is then inherited by any model that defines the time evolution of the SED. This allowed me to use a number of extensions to the base magnetar model that were implemented as plug-ins.

3.1.3.2 Model extensions

While the base magnetar model is a good fit for the majority of SLSNe light curves, in some cases, such as DES14X3taz, it is impossible to fully model the SN without introducing any further assumptions. In this section, I will describe a number of magnetar model extensions which I have introduced as an attempt to improve the quality of our fits. It is important to note that these were never used in the simulation of SLSNe for both the rates of SLSNe in Chapter 4 nor the creation of the DES artificial training sample in Chapter 5, as the base model remains a good fit around maximum light which, in case of the DES and SNLS seasons, is the region observed by our data. The extensions demonstrate the capabilities of SLAP and were used only to broaden our understanding of specific, individual objects.

Piro (2015) Upon the discovery of DES14X3taz, an important question was the nature of the engine powering the precursor bump. Smith et al. (2015) showed that the peak of DES14X3taz was well explained by a model where the supernova explodes inside an envelope of an extended dense wind. The shock-breakout, which is usually observed as a short, <1 day, is a flash of high energy radiation that gets reprocessed into a longer duration emission of lower energy. This model is highly degenerate in the ejecta mass and explosion energy. However, as these parameters also play a part in the modelling of the spin-down of a magnetar, the combination of these two models gave us an unprecedented opportunity to derive these parameters directly from the observed data.

In this extension of the model, we introduced parameter, t_d, measuring the delay between the explosion of the SN and the onset of the magnetar spin-down. These have not been previously considered to occur at different times (Nicholl et al., 2015b). However, I have found through the modelling of DES14X3taz (Figure 3.3) that it is impossible to reconcile the magnetar and extended shock models without the introduction of this parameter. Further evidence for is presented in Section 3.1.3.2, where the best fit magnetar model for DES14X3taz is shown to require an extended photosphere, consistent with a $t_d \sim 17$ days (assuming a constant expansion velocity), in order to better describe the rise phase of the SN.

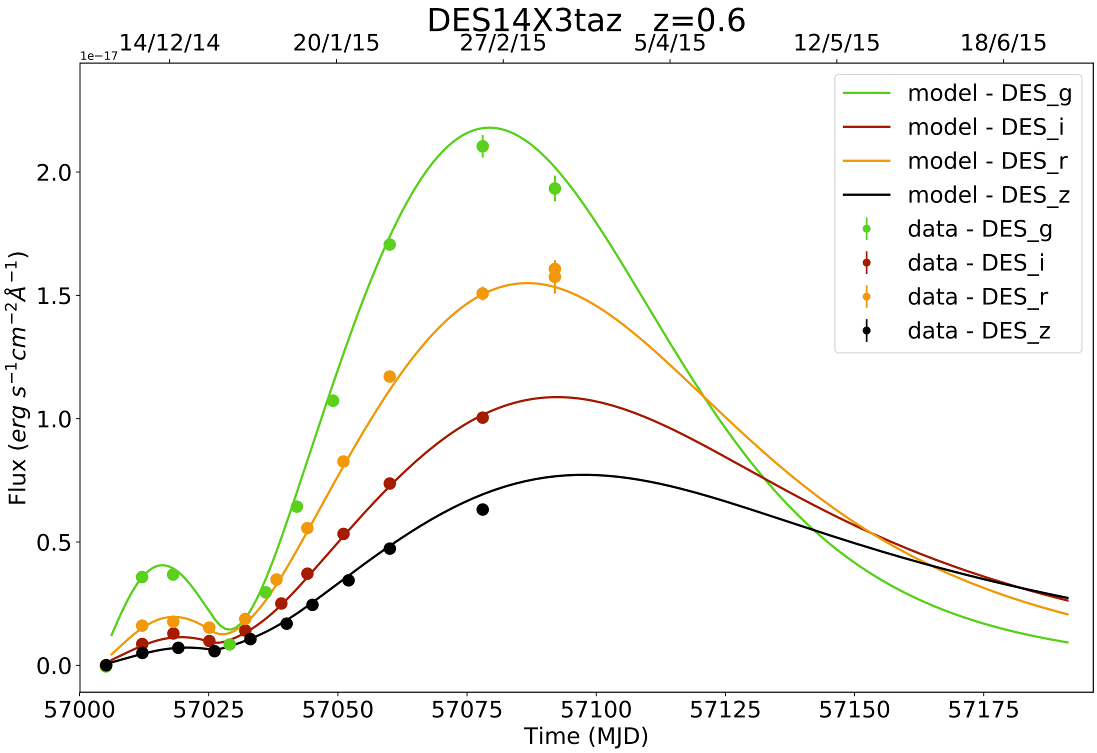

FIGURE 3.3: SLSN DES14X3taz fit with the combined Magnetar and Piro (2015) models. Combining the models breaks the degeneracy between the kinetic energy of the SN explosion energy and the ejecta mass allowing for a direct measurement of these values.

$R_0 > 0$ While it is widely accepted that the birth and a spin-down of a magnetar is the most likely progenitor of SLSN, the exact process through which the high-energy radiation produced by the magnetic breaking is transported into the outer shells of the ejecta is not yet understood. If the injection of energy does not closely coincide with the time of the explosion of the progenitor star, the SN could go through a 'grey' phase, powered only by the explosion energy of the SN, followed by a rapid rebrightening at the point of the spin-down energy injection. In several cases, including PS1-11ap and DES14X3taz (where we exclude the pre-peak bump data), the magnetar model does not fit the earliest stages of the light curve correctly.

In order to investigate this delay, I have introduced a non-zero initial progenitor radius. While the radius of the progenitor star is never zero, it is usually considered negligible in comparison with the expansion velocity of the ejecta. However, in the case of DES14X3taz and PS1-11ap, I found initial radii consistent with ejecta that underwent an expansion, at a constant velocity, for 17 and 9 days respectively. PS1-11ap has no observations prior to its first detections making it impossible to determine if the object was associated with a pre-peak event. As shown in Figure 3.4, this technique, can provide insight into the mechanism behind the magnetar energy injection even in the absence of the earliest and pre-explosion epochs.

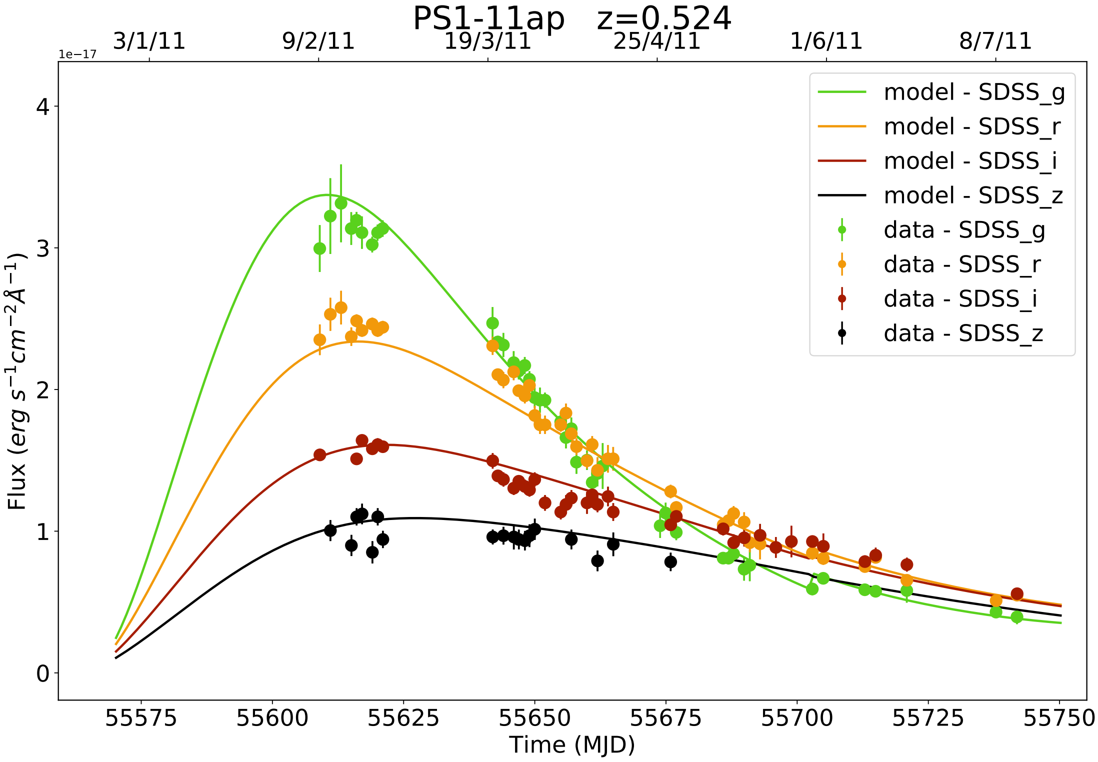

FIGURE 3.4: The magnetar model fit to a SLSN, PS1-11ap. The model does not assume the initial radius of the SN to be zero at the onset of the spin down of the Magnetar, instead, it is fitted as a free parameter. The value for R_0 found for PS1-11ap is consistent with a ejecta that has undergone expansion for 9 days prior to the onset of the Magnetar

Nickel decay Another interesting questions that we were able to investigate using SLAP is the contribution from the radioactive decay of ^{56}Ni and ^{56}Co as an additional energy source powering the ejecta. I have introduced this to investigate a potential mechanism powering the peculiar, flat evolution of DES13S2cmm. In this model, I add the contribution from the decay of these radioactive elements into the bolometric luminosity of the SN and do not introduce any other modification to the model. While we find that the radioactive decay alone cannot account for the evolution of DES13S2cmm, this test demonstrated the ease with which we are able to modify our models to test new assumptions. The evolution of DES13S2cmm is further investigated in Angus (in prep).

3.1.3.3 Maximum Likelihood methods

The model optimisation routines were also a key consideration in the design of SLAP. One of the main goals was a full autonomation of the fitting process, without the need for manual fine-tuning of input parameters. This is crucial for performing fits on large datasets, containing thousands of objects where only a small fraction is likely to be good matches to the model. Furthermore, we do not wish to introduce any human biases to the fitting procedure, particularly in the case of the ML training sample as the techniques used by us are sensitive enough to recover such biases over the true trends in the data.

In the early stages of the project, we have explored fitting the model using the Maximum Likelihood Estimate (MLE) method. This approach is based on maximising the Likelihood function which, in the frequentist approach, describes the probability of the observed data originating from the underlying model. As the uncertainties in our observations are normally distributed I use the Least Squares (LS) regression analysis which is a special case of MLE. In LS fitting, we minimise the residual, defined as the uncertainty weighted difference between the data and a model, using the χ^2 test as a metric for defining the goodness-of-fit:

$$\chi^2 = \sum_{i}^{N} \left(\frac{O_i - m_i}{\sigma_i} \right)^2 \tag{3.15}$$

MPFIT The MLE fitting approach was implemented in SLAP using MPFIT (Markwardt, 2008), based on FORTRAN's package MINPACK (More et al., 1980). MPFIT is an implementation of the Levenberg–Marquardt non-linear LS fitting algorithm (Levenberg, 1944; Marquardt, 1963). This is a popular and highly optimised example of the class of iterative, gradient descent algorithms that work by traversing the likelihood function, moving in the direction of lower χ^2 (i.e. higher likelihood). The algorithms use a gradient (either analytical or numerical) of the likelihood function to inform the direction and size of a jump taken at each iteration. In the Levenberg–Marquardt algorithm a damping coefficient is introduced decreasing the number of steps taken by the algorithm before converging on a minimum.

While MPFIT was very promising during our testing, we discovered that the quality of our fits was strongly dependant on the choice of the initial parameter guesses. This is a common issue amongst all gradient descent algorithms informed only by the gradient at the measured point. This leads to them finding the local likelihood maximum, nearest to the initial parameter guess instead of the global value. This contradicted one of our strongest demands for the package, as SLAP would require manual modification for the initial parameter guesses, making it impossible to use with a large number of objects.

3.1.3.4 Bayesian Inference

While a number of global optimisation approaches have been trialled, we realised that the complexity and degeneracies of the magnetar model require a fully Bayesian treatment in order to efficiently find the global minimum (or Maximum Likelihood) of the model.

Bayesian Inference is a technique based on the Bayesian approach to probability, derived from Bayes' Theorem which states that for a set of model parameters θ and data $\mathbf{D}$:

$$P(\theta|\mathbf{D}) = \frac{P(\theta)P(\mathbf{D}|\theta)}{P(\mathbf{D})} \tag{3.16}$$

where $P(\theta|\mathbf{D})$ is the Posterior Probability, $P(\theta)$ denotes the Prior Probability, $P(\mathbf{D}|\theta)$ defines the Likelihood and finally, $P(\mathbf{D})$ is the model Evidence.

The Posterior Probability describes the probability of the model θ given the observed data $\mathbf{D}$. The biggest difference between the frequentist and Bayesian view of probability is the inclusion of the Prior Probability which describes our belief in the model before we make the observations $\mathbf{D}$. The Likelihood function here is analogous to the Likelihood function used in MLE. In fact, in the special case where the Prior distribution is uninformative (i.e flat), Bayesian Inference is equivalent to MLE and would yield the same result. The Evidence, $P(\mathbf{D})$, acts as a normalisation constant and is only used in comparing distinct models and not in determining their 'best-fit' parameters. $P(\mathbf{D})$ is usually very difficult to compute as it requires the Likelihood function to be integrated over the entire parameter space. The following paragraphs describe the methods I used for computing the Posterior Probability distribution as well as estimate the model Evidence.

MCMC Markov chain Monte Carlo (MCMC) is an extremely popular and widely used set of techniques for estimating the Posterior distribution. One of its simplest implementations, the Metropolis-Hasting algorithm, iteratively samples the Posterior distribution by drawing a new point from the normal distribution centred at the previous parameter and accepts it if the value has a higher probability. However, what differentiates the MCMC approach from MLE techniques is that a sample can also be accepted if it has a lower probability that the previous point in the chain. The acceptance ratio here is defined as the ratio of the new probability to that of the previous iteration. This allows the 'walker' to sample the entire Posterior Probability distribution provided that the chain a sufficiently long.

In this thesis, I have tested both a custom MCMC implementation as well as the popular and heavily optimised, multithreaded package, Emcee (Foreman-Mackey et al., 2012). While both approaches can estimate the Posterior distributions as well as the best-fit parameters with no external input or hyperparameter fine-tuning, their performance based on a need to evaluate millions of models to provide a full sampling of the Posterior distribution, was however very poor. A light curve fit would often require in excess of 8 CPU hours, despite the heavy optimisations of the model.

MultiNest A recently developed technique for approximating the Posterior Probability distribution, showing a great improvement in efficiency is Nested Sampling (Skilling, 2006). Here, the Posterior distribution is calculated as a by-product of the model Evidence evaluation. While this is usually a very computationally expensive calculation, Nested Sampling uses the properties and relationship between the likelihood and the prior to reducing the multi-dimensional integral into a single dimension, which is simpler to evaluate. The algorithm populates the prior with a relatively small (I used 2000) 'live' points which calculate the Likelihood. The point with the lowest Likelihood is replaced by a new point, geometrically closer to the point of highest Likelihood. The new point is accepted if its Likelihood is higher than the point it originally replaced. Nested sampling provides a near 1000-fold efficiency improvement over the common MCMC methods. This makes the approach of using Nested Sampling sufficiently fast and robust to satisfy the design requirements of SLAP.

In this thesis, I use MultiNest (Feroz et al., 2009, 2011, 2013), a Fortran based implementation of the Nested Sampling algorithm. This is one of the most popular implementations of the technique. It is robust and thoroughly tested in a number of cosmological studies using the CosmoMC package (Bridle, 2002). One of the greatest advantages of MultiNest is its operation in a multi-modal mode where the algorithm returns not only the Maximum-a-Posteriori (MAP) parameters but also positions of other, local, maxima.

3.1.3.5 pyMagnetar

While SLAP was very heavily used throughout this thesis as a tool for modelling SLSNe, putting an emphasis on the optimisations involving model fitting, I have also used it as a tool for building synthetic catalogues of SLSNe. While this was directly possible using the C++ frontend, it is difficult and inefficient to interface the code with the majority of modern astronomy pipelines which are most commonly written in Python. Using the Cython language, I have created a higher-level interface to the code, pyMagnetar. I have also implemented a further level of optimisation by fine-tuning the code to work with a single set of photometric bands (e.g DES or SNLS). As the code no longer needed to consider any arbitrary filters, its performance has increased considerably.

3.2 Modelling CCSN

There has been a recent increase in interest in modelling CCSN driven by the development of large area surveys such as LSST and ZTF. The predicted numbers of transient discoveries exceed our ability to classify the SNe using the conventional, manual techniques. The modern approach using machine learning classifiers require a large number of training samples, distributed evenly amongst all subclasses of SNe. The number of real objects observed to date is not sufficient to act as a training sample alone. It must, therefore, be supplemented by an artificial or augmented sample of SNe, generated from a set of template SN.

Amongst a number of past CCSN templates (Schlegel, 1995; Nugent et al., 2006), Kessler et al. (2009) has been the most commonly used tool for creating artificial samples of SN in recent years. Packaged as part of the SNANA suite of analysis and simulation tools, it is widely used in a number of leading surveys including SDSS, DES and PS1 as well as ML studies of SNe (Kessler et al., 2010; Lochner et al., 2016). Despite its popularity, SNANA's templates have a number of drawbacks (Kessler et al., 2010). In SNANA a single spectroscopic template per SN subclass (Taken from Nugent et al., 2006) is warped to match the photometry of a number of SN light curves observed by SDSS, SNLS and CSP. While generating 43 templates for CCSN (overall subclasses, as per the latest release of SNANA (Jones et al., 2017)), they do not account for the diversity in the SEDs of CCSN nor their evolution. Furthermore, the pseudo-templates, generated from a single spectroscopic master-template, have a narrow wavelength coverage not extending considerably below the rest-frame SDSS u-band filter and, in the majority of cases, above the SDSS i-band.

In order to create a modern set of templates, suitable for ML studies of SNe, we present a new set of tools which move away from the approach of using the master templates found in Nugent et al. (2006). We use all available, high quality photometric and spectroscopic data for CCSN found in the literature in order to create templates that are not correlated with each other. We also use auxiliary UV data to extend the SED to lower wavelengths allowing, for the first time, to simulate these objects in all bands at all redshifts where the SNe are detectable in DES and LSST.

In this section, I describe the main design choices behind both CoCo and pyCoCo, the packages developed to create spectroscopic templates of CCSNe as well as simulate them in a number of surveys. I discuss the models used in modelling the CCSN light curves and those undertaken to create their spectroscopic templates. I then describe the steps taken to extend the spectroscopic templates into both the UV and IR parts of the SED, not covered by the observed spectra.

3.2.1 CoCo

At a basic level, the packages I developed as tools for simulating CCSN are very similar to SLAP, used in the modelling SLSN. Its performance, similarly to SLAP, was a critical part of the code design as we aim to simulate millions of light curves in LSST and DES. We therefore developed the core of the package in C++, and used CYTHON to create a PYTHON front-end interface. I will follow our internal naming for the packages and refer to the backend packages, developed in C++, as COCO and the PYTHON front-end wrapper as pyCoCo.

COCO consists of four core packages: LCFIT used to fit the SN light curves with a number of models, SPECFIT used to match the observed spectra to the photometry, SPECPHASE which assigns the phase to each spectrum and corrects them to a common redshift and finally LCSIM which can be used to SN based on the outputs of the previous three packages. In the following subsections, I will describe these packages as well as the models, decisions and assumptions we made that led to the final product.

3.2.1.1 LCFit

The process of creating the spectroscopic templates of CCSN start by fitting the observed light curves for the SNe with an analytical model able of describing their morphology as well as reliably extrapolating them. This step is required in order to later flux calibrate the observed spectra to match the observed photometry. The interpolation allows us to calibrate the spectra on epochs where there was no photometric data point available. While a non-parametric approach could be used such as Spline Interpolation or Gaussian Process Regression, we required an ability to extrapolate the light curve fits beyond the range of the observed point for the cases where the spectroscopic follow-up either exceeded that of the photometry or, in even rarer cases, preceded it in time.

At this phase of the procedure, the models are fitted using MULTINEST. The photometry is fitted independently for each band. Thanks to the use of a Bayesian fitting routine, the resulting fit gives us the curve of best fit as well as a confidence region for the model. For technical reasons we do not store the best-fit parameters, instead, we store a dense sample curve of best fit and its corresponding region of confidence.

In this thesis, I have trialled and implemented a number of models found in the literature as tools for fitting the light curves of CCSN. In the following sections, I give their brief overview and discuss their benefits and drawbacks in the context of this project. The comparison of the models used in this thesis for an example SN2011hs is shown in Figure 3.5.

Bazin09 The simplest, yet most versatile, model for describing CCSN can be found in Bazin et al. (2009) (Bazin09 from here). This simple model is a combination of a logistic function which describes the rise of the SN and an exponential decay which matches the decline of the light curve (Equation 3.17). This model was successfully used to photometrically identify CCSN-like events in the SNLS. While the simplicity of the model means that it is not able to fully describe the behaviours of all SNIb/c, it provides a good match to those dominated by the radioactive decay of ^{56}Ni as their power source. We have found it to be very powerful in the cases where the observed light curve was sparsely sampled as, even in the most difficult cases, the model can produce a well-constrained solution that matched the expected features of a SN.

$$F(t) = A\frac{e^{-\frac{t-t_{max}}{\tau_{fall}}}}{1+e^{\frac{t-t_{max}}{\tau_{rise}}}} \tag{3.17}$$

Kessler10 A more complex version of the model used in Bazin et al. (2009) was used in Kessler et al. (2010) (Kessler10) as a base for their work on creating a photometric sample of CCSN for the use in the Supernova Photometric Classification Challenge. While the model parameterises SN using an underlying exponential decay and rise, it additionally provides the ability for the model to account for a secondary maximum often observed by SNIa. As CCSN rarely show signs of a secondary maximum, the extra degrees of freedom often improve the early fits around the early rise time phases of the SN where there are other mechanisms in action (e.g. shock breakout, Hydrogen recombination etc.) that inject additional energy into the early light curves.

One drawback of this model and the reason why, on average, we have found it to not improve the quality of our fitting is the common timescale for the decay of the primary and secondary maxima. This does not correspond to the observed behaviour in CCSN where the power sources are not physically linked and therefore act on different dynamic timescales.

$$F(t) = A \times [1 + a_1(t-t_0) + a_2(t-t_0)] \times \frac{e^{-\frac{t-t_0}{\tau_{fall}}}}{1+e^{\frac{t-t_{max}}{\tau_{rise}}}} \tag{3.18}$$

Karpenka12 Karpenka et al. (2012) (Karpenka12) further improves on the model found in Kessler10 by decoupling the onset of the primary and secondary peak. While retaining the same number of free parameters as Kessler10, the improvements in the fitting quality are considerable for the SN Ib/c with a more complex morphology.

$$F(t) = A \times [1 + B(t - t_1)^2] \times \frac{e^{-\frac{t-t_0}{\tau_{fall}}}}{1 + e^{\frac{t-t_{max}}{\tau_{rise}}}} \tag{3.19}$$

This model was successfully used in a project involving SN photometric classification using basic Neural Networks (Karpenka et al., 2012), demonstrating that it is a suitable model for our use.

Firth18 Finally, we considered a new model introduced in Firth et al. (in prep; Firth18), based on the Karpenka12 model with an additional, fully independent of other properties, logistic decay term which can be used to model the shock breakout phase observed in some SN.

$$F(t) = A \times [1 + B(t - t_1)^2] \times \frac{e^{-\frac{t-t_0}{\tau_{fall}}}}{1 + e^{\frac{t-t_{max}}{\tau_{rise}}}} \frac{1}{1 + e^{\frac{t-t_{pre}}{\tau_{pre}}}} \tag{3.20}$$

The additional term introduced in this model makes it only compatible with light curves containing a large number of data points where this pre-peak event will be constrained to null in case of a lack of an observed shock breakout event, or those with a well-defined event. In other cases, the extra degrees of freedom simply act as an additional degeneracy in the modelling and often result in a lower quality fit than using a more basic model.

3.2.1.2 SpecFit

One of the most crucial parts of our procedure for generating templates of CCSN is the matching of the observed spectra to the flux of the photometry. Due to the complexity of spectral data reduction and flux calibration, the uncertainties associated with their measurements can be high, and more problematically, wavelength dependent. The accuracy of the spectral flux is particularly important in the case of high precision surveys such as PS1, DES and LSST, exposing the uncertainties from other sources such as SN simulations (Jones et al., 2017). The process used to correct the flux calibration, referred to as spectral 'mangling', adjusts the spectrum such that the synthetic flux measured by passing the spectrum through filter bandpass response functions matches the observed photometry. I have encapsulated this in the SpecFit package.

In order to adjust the spectrum, a spline is applied to it, designed in a way to smoothly correct the spectra, as shown in Figure 3.6. A spline is a smooth, continuous function defined using a number of control points; a position and amplitude. The wavelength at

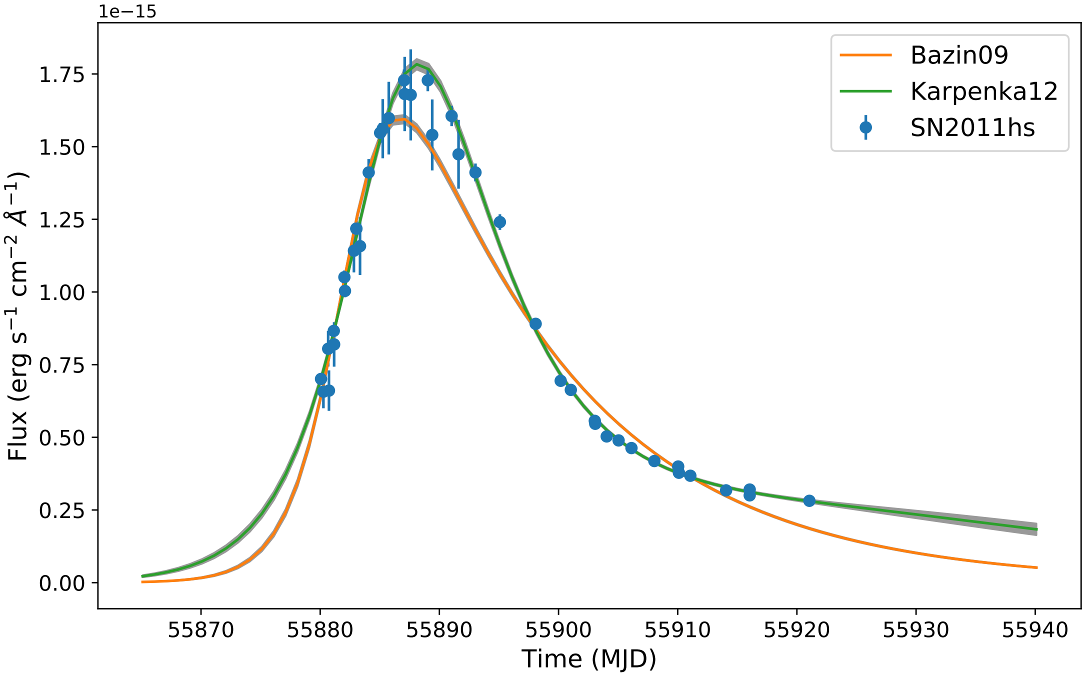

FIGURE 3.5: The light curve of SN2011hs, a SNII, fit with the Bazin09 and Karpenka12 models for comparison. Both models are based on the same exponential decline and logistic rise function. However, Karpenka12 adds an additional term that allows for the change of slope in the light curve decline as observed in this SN

which we place the control points matches that of the central wavelength of the filters while the amplitude is determined using a numerical minimisation routine. We again use MULTINEST as our fitting tool. The choice of the endpoints of the spline is important. In this code, I have placed them at 100Å outside of the wavelength range of the mangled spectrum. The amplitude of these points is not subject to the fitting, instead, they are determined by extrapolating the two most extreme points on either side of the spectrum using a straight line.

While developing the mangling code, we discovered several issues which had to be addressed before reliable results could be obtained. One of the major issues arose due to control points of the splines positioned to close to each other, causing the interpolated function to behave erratically and far from the expected. We have traced this to using filters which are derivatives of each other, such as Johnson's R and SDSS-r, that only vary in central wavelength by ∼50Å. This would not result in a problem if the control points were already correctly calibrated but, due to the nature of the fitting process, the points were fit independently causing large, non-linear degeneracies that cannot be controlled even using routines as powerful as MULTINEST. We were, therefore, forced to remove the overlapping photometry from the mangling. As we focused on preserving the maximum information in the bluer part of the SED, we have retained the band with a lower central wavelength.

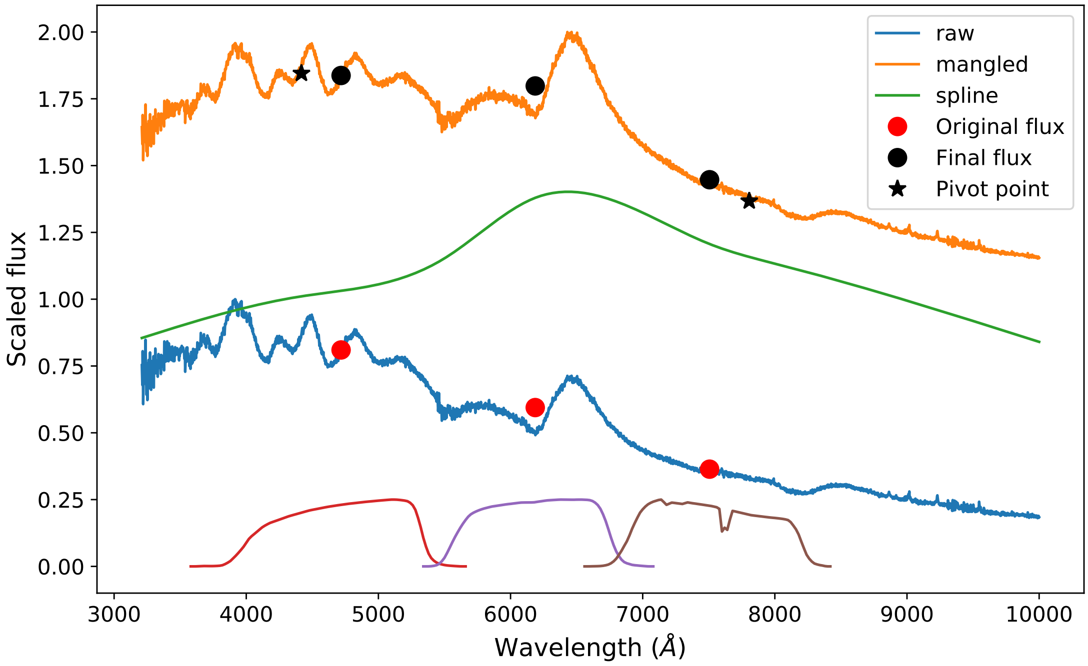

FIGURE 3.6: *top*: An example of an early 'raw' spectrum of SN2011dh. Synthetic photometry is computed from the spectrum in the *gri* bands before. Then, a minimisation routine is used to find a spline function which, when applied to the spectrum, will result in the synthetic photometry matching that observed SN flux producing the 'mangled' spectrum.

Furthermore, we have found that the mangling is not reliable when less than three bands are used to set the control points. This is caused by both upper and lower endpoints being extrapolated using the same two photometric points. Spectra that overlap with only two distinct bands cause degeneracies that are difficult to handle with even sophisticated fitting routines. Finally, SPECFIT saves the flux calibrated spectrum in the ASCII format, scales the spectrum to the observed photometry at the original redshift of the SN.

3.2.1.3 SpecPhase

A major difference between my approach to fitting the SLSNe and CCSN is the treatment of their explosion date (or the start date of the simulation). In the case of SLSNe, we have a well-defined explosion date, set as a free parameter in our model, prior to which we can assume the flux to be null. In the case of the models used in Section 3.2.1.1, their rise is not abrupt but following a logistic function which only tends towards zero at negative infinity, making it impossible to define the explosion date without any adding assumptions.

We must, therefore, define the time at which we insert the light curve in our simulations using a different system. In this case, we use the time of the maximum light of the SN as the point of reference, measured in the rest-frame V-band. The phase is determined in the following way; the spectra are shifted to z=0 (rest-frame). Using the distance moduli for the host galaxies obtained from the NED archives (Tully, 1988). I scale the flux for each spectrum to give their apparent flux at 10pc (e.g. the absolute magnitude). I then synthesis a V-band light curve from the spectral time series and fit it using the same approach as in Section 3.2.1.1. The peak is determined numerically as the maximum of the light curve fit.

3.2.1.4 LCSim

Following the previous steps, we can obtain a set of spectral templates that can now be used to generate a new sample of synthetic SN light curves. The template spectra are shifted to the required redshift, corrected for the distance modulus, then corrected for the host galaxy extinction (before they are redshifted) and corrected for milky way extinction (once at the observed redshift). Synthetic photometry is then generated for the requested bands before a light curve model is fit, allowing for simulated photometry points to be generated at an arbitrary phase.

LCSim is the only package as part of CoCo that does not rely on MultiNest as a minimisations tool. While it would have been optimal from the accuracy and robustness point of view to use it, we have found that its performance was insufficient in order to simulate millions of CCSN, as required. After discovering issues with numerical instabilities in MPFIT (used in Section 3.1.3.3) when computing the derivative of our residual function, we have decided to use a more modern package, Minuit2 (James & Roos, 1975). Designed by CERN and heavily used within the ROOT library (Brun & Rademakers, 1997), Minuit2 utilises more modern numerical libraries which helps it to handle numerical uncertainties better than its Fortran derived predecessors. Minuit2 implements a number of algorithms derived from the broader gradient descend family. In LCSim we use migrad which is the default minimiser in the package and is based on the same concept as the Levenberg-Marquardt algorithm used in MPFIT.

3.2.2 pyCoCo

Following the same design pattern as in SLAP, I created a Python interface for the LCSim package using the Cython intermediate language. The ability to interface the code with Python allowed us to manipulate the simulated light curves directly in the memory without the need to create a time and memory consuming intermediate output, significantly reducing the overheads in the simulation. pyCoCo forms a major role in the modelling of CCSN in Firth et al. (in prep) as well as this thesis (Chapter 5).

3.2.3 SN Ib/c SED UV Extensions

SN Ib/c were the main focus of CoCo. Their simulations are some of the most desired amongst various classes of SN as they are the main source of contamination in the samples of SN Ia due to the similarities in the physics that powers their luminosity. SN Ib/c are, however, relatively rare in comparison to SN Ia or even hydrogen-rich SN. Firth et al. (in prep) collected a sample of ‘good’ SN Ib/c light curves and their respective spectra from the literature. 29 SNe were part of the initial sample before extra quality cuts were applied. The final sample included 17 SNe that were used to generate the templates.

As would be expected from such a diverse sample of objects, a large number of the spectra do not have a very good wavelength coverage, often not exceeding the range of 4000-7000Å. However, the light curves for almost all SN in the sample include the minimum of BVR bands with a number of objects including both redder and bluer bands. It was, therefore, possible to use the extra light curve information as a base upon which we can extend the spectroscopic templates of the SNe. Red extensions were required in order to simulate the low redshift SN in the reddest bands (e.g. DES z-band). These extensions were performed as part of Firth et al. (in prep) and used a black body to extend the spectra up to 10500Å. The flux was then corrected to the photometry by again passing the spectral time series through SpecFit.

In contrast with the red extensions, we could not rely on the observed photometry for the blue wavelength extensions. As we aim to simulate SN Ib/c to redshifts of up to z≈0.8 in the DES deep-fields, we require the templates to extend to ∼2000Å in order to overlap with the observer-frame g-band at that redshift. The required region of the light curve most closely matches that of the Swift-UVOT UVW1 filter (Roming et al., 2005). The Swift satellite launched in late 2004 as a rapid response Gamma-Ray Burst (GRB) detector. Since then, it has observed a number of SNIb/c. The data, however, is not present for all objects giving a need to approximate the behaviour for the objects with no UV data.

Using the data collected by the Open Supernova Catalogue (OSC; Guillochon et al., 2016), I have created a subsample of our template SNe with available UV data. Amongst these, a large number of objects only had UV coverage at the very earliest epochs, likely triggered as a follow-up based on the x-ray detections of the object. Several of these objects, however, did later receive an extended follow-up campaign, giving us light

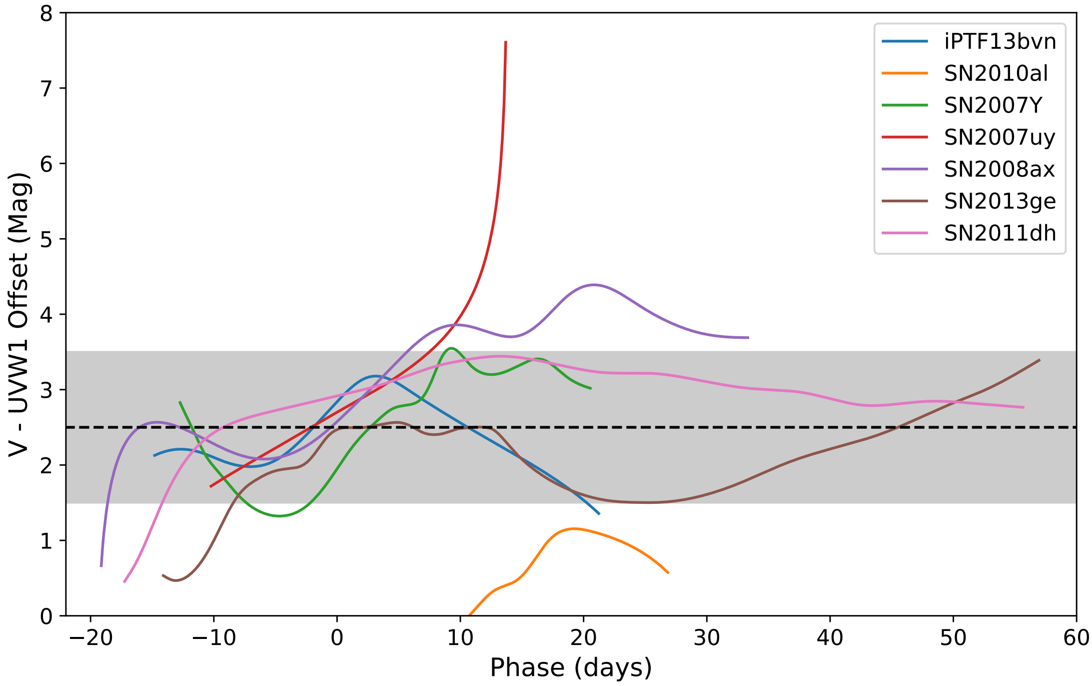

Figure 3.7: The offset between the observed UVW1 and V band filters for all stripped-envelope SNe with the available Swift data. The light curves have been interpolated using Gaussian Process Regression.

curve information past maximum light. For these objects, I have performed light curve interpolating using Gaussian Process Regression (Chapter 3.3). This allowed me to compare the UVW1 light curve to the V-band, as shown in figure Figure 3.7, showing that during the main phase of the SN (excluding the shock breakout), the UWV1 and V band light curves followed a very similar evolution. The UVW1 were found to be 2.5 magnitude dimmer (10 times dimmer in flux). I, therefore, use this property to create artificial UVW1 light curves by offsetting the V-band light curve by 2.5 magnitudes in flux and retaining its overall evolution.

Using the extended light curve coverage, we can extend the spectra following a similar process to that used for IR extensions. As there is little information about the UV spectral evolution of CCSN, I follow the same technique as Firth et al. (in prep) by using a black body to extend the SEDs. We again pass the extended spectrum through SpecFit, matching the spectrum to the synthetic UVW1 photometry.

3.2.4 SN II with CoCo

Although Firth et al. (in prep) only considered SN Ib/c, I also need to simulate SN II in this thesis. For this, I have followed the same methodology with several steps that were optimised to better suit SN II.

All data in this project was obtained using the OSC repository. The data was collected for objects matching the hydrogen-rich SN subclasses including SNII, SNIIP, SNIIL, SNIIn, SNIIb and SN1987A-like. Only the objects with a light curve coverage including the pre-peak and post-peak data, as well as a relatively dense spectral coverage, covering the same regions as the light curve, were included in our sample. I have used the toolkits developed in Firth et al. (in prep) to average any spectra that were taken in rapid succession. I have also removed the regions of each spectrum where no SN light was detected, or the SN was too low to confidently recover the underlying morphology of the SED.

I then removed all spectra with a coverage of less than two photometric bands. I also removed the spectra that did not overlap with the V-band. Following these clearing stages, I again removed the objects that now no longer satisfy the coverage required for our analysis. The above steps retained a sample of 11 objects with sufficient quality for the use as templates for CCSNe.

The light curves for all retained objects were fit with all models described in Section 3.2.1.1. While the more complex models such as Karpenka12 and Firth18 are able to fit the data more precisely, they are unable to constrain light curves with a small number of data epochs. In the process of simulating the light curves, we fit the models to photometry synthesised from the spectra which are sparse for most objects in our sample. Instead of using the more complex models, I fit all SN in the sample with the most basic Bazin09 model which produced a good fit to all light curves in our sample. I note here that this was not expected. SNIIP are associated with a light curve plateau phase which could not be accounted for in this model. However, none of the objects that observe this behaviour had sufficient spectral coverage to pass the previous quality cut. This is not an optimal scenario as a whole class of objects are, seemingly, excluded from the sample. The plateau is, however, more prominent in the redder bands and therefore does not appear as a strong feature in the rest-frame blue bands that form the majority of the observed SED at high redshift where we simulate the majority of our SNe.

A difference between the SN Ib/c and SN II is the approach to extending the light curves in both the IR and UV regimes. In the IR, I found that a number of SN II spectra would fail to fit a black body function. At this stage, such objects were removed from the Firth et al. (in prep) sample. To retain the maximum number of objects I have instead fit the objects using an exponential decline function. As a simple numerical form, this function can correctly fit all objects. It is not necessary for this function to physically correspond to the expected SED as the mangling step corrects this later.

The method used for the UV extensions was also modified as the UV data for the SN II was very limited. It shows that these objects rise as very UV bright but rapidly evolve

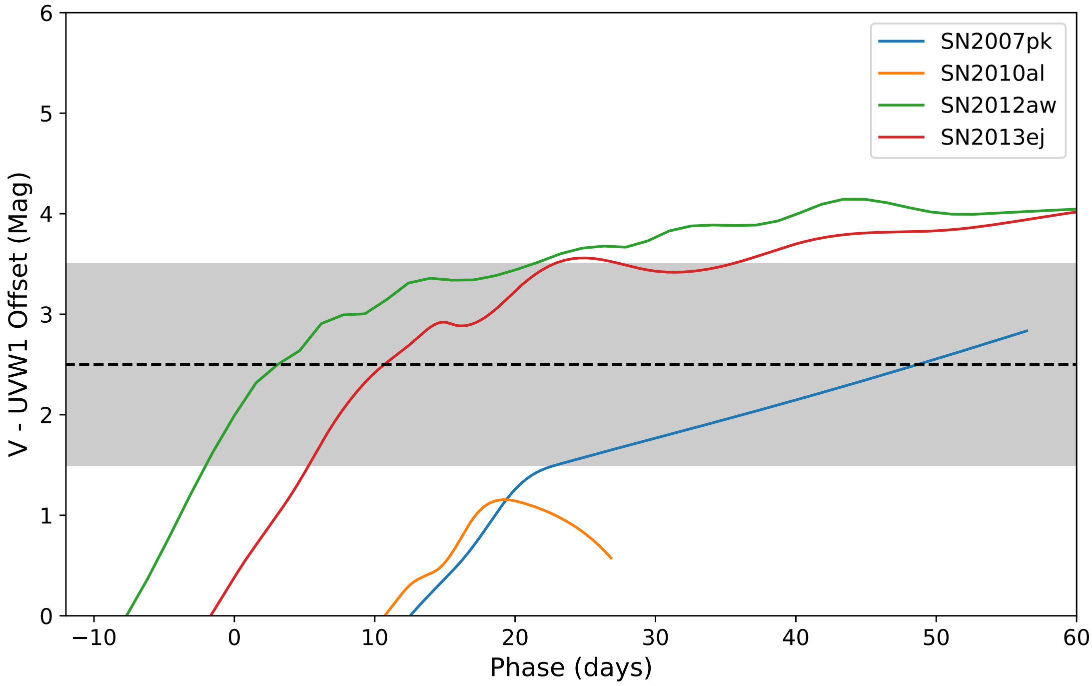

FIGURE 3.8: The offset between the observed UVW1 and V band filters plotted all hydrogen-rich SNe with the available Swift data. The light curves have been interpolated using Gaussian Process Regression.

in colour, quickly losing their UV flux. This meant that the methodology of creating an artificial UVW1 band by scaling the optical bands wouldn't work. The number of objects with a sufficient UV coverage was also insufficient to obtain a relationship between the UV and optical evolution of the SNe. All these issues can be seen in Figure 3.8. As an approximate solution, I have extended the spectra of SN II by fitting their SEDs with a black body model and did not follow it with a mangling step. In figure.

3.3 Gaussian Processing

One of the biggest obstacles, and perhaps the main reason, behind SN classification, still relying on non-ML approaches is the irregular nature of the observing cadences. As a broad simplification, ML techniques rely on recognising repeating sequences or patterns. In order to recognise patterns independently of their position along the time series, they must be uniformly sampled. Without this, any classifiers would bias the result towards a preferential explosion time. Moreover, even in cases where we would be willing to accept this drawback, there is a limited number of algorithms that are designed to work with unevenly sampled data.

Previous SN studies using ML approaches used physically motivated features extracted from light curve model fits. In the most complete study of this kind to date, Lochner et al. (2016) fit the SALT2 SN Ia model to a number of SN classes and used these properties to classify the SNe. I do not follow this approach as the SALT2 model is incapable of reproducing the light curves of SLSN and other peculiar transients. This would result in a classification very strongly dependant on the quality of the light curves i.e SALT2 could produce a SNIa-like light curve if fit to very low SN data based on its priors alone.

My aim in this section is to develop a method for interpolating SN light curves using a non-parametric approach in order to enable the classification of SN using ML models that do not rely on explicit feature extraction. Amongst a number of approaches that I have considered in this thesis, Gaussian Process Regression is an extremely powerful and robust way of modelling the light curves.

3.3.1 Theory

Gaussian Process (GP) (Rasmussen & Williams, 2006) is defined as a set of normally distributed random variables, (x, y), where any subset of them can be drawn from a joint Multivariate Gaussian Distribution, $\mathcal{N}$, defined using the mean of the data, $\bar{y}$, and a covariance function, $K = k(x, x'|\theta)$. The process of interpolating data using GPs is referred to as Gaussian Process Regression (GPR) or Kriging (Krige, 1951; Rasmussen & Williams, 2006; Ebden, 2015).

From the definition of a Gaussian Process we know that the observed data points, y, and the points we wish to evaluate, y_*, are drown from the same Multivariate Gaussian Distribution giving us the relationship between the data points:

$$\begin{bmatrix} y \\ y_* \end{bmatrix} \sim \mathcal{N}\left(\begin{bmatrix} \bar{y} \\ \bar{y_*} \end{bmatrix}, \begin{bmatrix} K & K_*' \\ K_* & K_{**} \end{bmatrix}\right), \tag{3.21}$$

where K is the covariance matrix for the observed data, K_* is the covariance between the new and the observed data, and K_{**} is covariance between the new points. It can be shown (Rasmussen & Williams, 2006) that the probability distribution of data points y_*, given the observed data, y is:

$$p(y_*|y) \sim \mathcal{N}(\bar{y_*}, var(K_*)). \tag{3.22}$$

where

$$y_* \sim K_* K^{-1} y \tag{3.23}$$

$$var(K_*) \sim K_{**} - K_* K^{-1} K_*' \tag{3.24}$$

The above equations can be solved using linear algebra and do not require any optimisation techniques allowing for a very rapid computation for small data sets containing no more than several thousand data points. For larger datasets taking the inverse of the covariance matrix, K^{-1} becomes very computationally expensive using even highly optimised algorithms such as the Cholesky Decomposition. A log likelihood, $log(\mathcal{L})$ of the Gaussian Process can be computed using Equation 3.25 (as derived in Rasmussen & Williams (2006)) and can be used to inform the choice for the hyperparameters, θ, that define the relationship between the data points in the covariance matrix K.

$$\log(\mathcal{L}) = -\log p(y|y_*, K(\theta)) = \frac{1}{2}y^{\mathrm{T}}K(\theta)^{-1}y + \frac{1}{2}\log|K(\theta)| + \frac{N}{2}\log 2\pi \tag{3.25}$$

3.3.2 Covariance Kernels

The true power behind GPs lays in the choice of the covariance function. The kernels are responsible for defining the connection between the points as well as deciding on the span and the degree to which any data point can inform the position of another. I have trialled a number of kernels popularly used in when interpolating one-dimensional time-series data (Rasmussen & Williams, 2006). This included the Squared Exponential (SE), Mateŕn 3/2 (M32) and Mateŕn 5/2 (M52) kernels.

3.3.2.1 Squared Exponential Kernel

The squared exponential kernel is the most commonly used covariance function in GPR. It is defined as:

$$k_{\mathrm{SE}}(x, x') = \sigma^2 \exp\left(-\frac{(x-x')^2}{2l^2}\right) \tag{3.26}$$

where the σ is the amplitude at maximum correlation and l governs the range of influence of the data point on each other. I have suplemented all kernels used in this thesis with a simple white noise kerned:

$$k_{\mathrm{noise}}(x, x') = \delta_{x,x'}\sigma_n^2 \tag{3.27}$$

where the value σ_n only controls the value of self-correlation, e.g the correlated noise on the measurements.

This kernel corresponds to the Normal distribution, giving rise to its popularity. However, we know that the majority of SNe, with an exception of some peculiar classes (Pursiainen et al., 2018), do not have a light curve morphology consistent with a Gaussian distribution. From the modelling of SNe using both radioactive decay and the

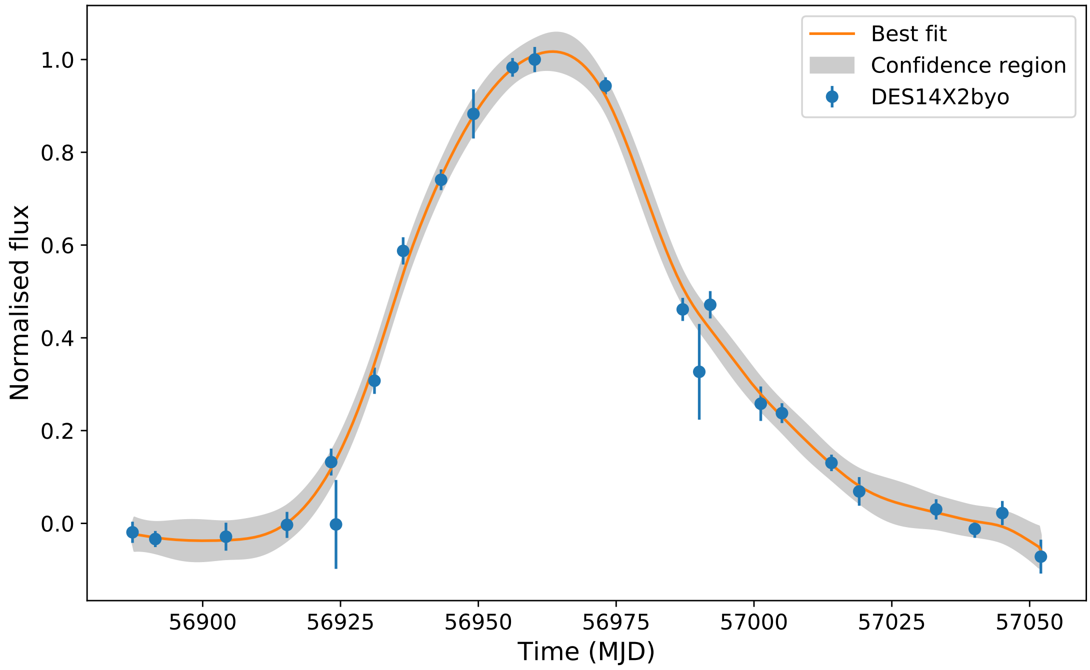

FIGURE 3.9: An example GPR fit to the r-band light curve of a SLSN, DES14X2byo. The fit was performed using the Mateŕn 3/2 covarience function. This fit demonstrates the power of GPR in creating smooth interpolations which take into account, but are not controlled by, outlier points.

Magnetar model, we know that the dependence of the light curve evolution on time is more closely approximated by a linear exponential.

3.3.2.2 Mateŕn Kernels

The Mateŕn family of kernels is a better-suited kernel choice for modelling SNe. It has a linearly exponential dependence on the covariance between data points controlled by a time scale factor, l, as well as a quadratic term. We use the first and second order Mateŕn kernels denoted by $\mu = 3/2$ (Equation 3.28) and $\mu = 5/2$ (Equation 3.29) where the Mateŕn kernel becomes equivalent to the Squared Exponential kernel at $\mu -> \infty$. These kernels have a similar form to the Bazin09, Kessler10 and Karpenka12, combining a quadratic linearly exponential term.

$$k_{\mathrm{M32}}(x,x') = \left(1 + \frac{\sqrt{3}(x-x')}{l}\right) \exp\left(\frac{\sqrt{3}(x-x')}{l}\right) \tag{3.28}$$

$$k_{\mathrm{M52}}(x,x') = \left(1 + \frac{\sqrt{5}(x-x')}{l} + \frac{\sqrt{5}(x-x')^2}{2l^2}\right) \exp\left(\frac{\sqrt{5}(x-x')}{l}\right) \tag{3.29}$$

3.3.2.3 Choosing the Kernel

The choice of a kernel that is suitable for the use with a wide range of transients is not a straightforward one. While from the point of view of SNe alone one could consider the Mateŕn kernels to be the most suitable choice, this is not immediately obvious when considering AGN and other objects with a quasi-periodic light curve variability. For such objects, we would usually combine one of the above-mentioned kernels with a periodic kernel to account for the long-term variability. However, this would be incompatible with the light curves of SNe.

I have applied GPR to a small sample of SNe, randomly drawn from all subclasses simulated in this thesis as well as a number of AGNs. As expected the Mateŕn kernel results in a much higher $\log(\mathcal{L})$ when applied to SNe than the SE kernel. While both M52 and M32 kernels were a significant improvement over the SE kernel, the choice between M32 and M52 was not clear as the best fitting kernels were object-dependent. For the case of AGN, the SE filter and the Mateŕn kernels have all performed differently depending on the object and the level of variability in the light curve. However, as in the majority of cases the M32 filter behaved well. I have therefore chosen this kernel as the basis for all light curve interpolation performed as part of this survey. We have demonstrated the use of the Mateŕn 3/2 kernel in Inserra et al. (2018) where we used GPs to interpolate light curves of SLSNe in order to robustly determine their time of maximum light along with other observable properties.

3.3.3 Interpolating Light Curves

There is a number of packaged and libraries that implement the GP algorithm outlined in the previous sections. In this thesis I have predominantly used the George package written in a combination of Python and C++ (Ambikasaran et al., 2014). This package implements a number of kernels, including those described in Section 3.3.2. Using techniques similar to those applied by me for both CoCo and SLAP, George optimises the linear algebra solvers by implementing it in C++ while producing the interface in Python. This produces a fantastic performance, interpolating a typical DES light curve in ∼10ms.

To optimise the hyperparameters I have used a Python based pipeline utilising standard fitting routines found in the SciPy library (Oliphant, 2007), based on the FORTRAN's LMFIT package discussed in Section 3.1.3.3. MultiNest or other more advanced fitting routines have not been used to perform the optimisations as the performance penalty incurred by their use would render the process computationally too expensive.

This approach was applied in this thesis to all artificially generated light curves as well as the observed DES data. Furthermore, this pipeline was used in Inserra et al. (2018) in order to extract observable properties from a sample of SLSN light curves. It will also be used as a base for the light curve modelling in Angus et al. (in prep) describing the spectroscopic sample of SLSNe in DES.

3.3.4 Blackbody per epoch

One use of the GP interpolated light curves not directly linked to ML is its application in the physical modelling of SLSNe. A number of previous studies have modelled SLSNe by fitting individual epochs of data with a blackbody (Howell et al., 2013; Papadopoulos et al., 2015; Smith et al., 2015; Nicholl et al., 2017), however, due to the surveys often observing different bands on different epochs the evolution of the photospheric radius and temperature are often not very clear. While the previous studies did apply light curve interpolations, they used parametric approaches which may bias the evolution of the photospheric parameters.

Using GPs, we can interpolate the light curves in a non-parametric approach driven only by the data, its uncertainty and our measurement of their correlations based on the covariance function. Figure 3.10 shows an example of the radius and temperature measurement for DES14X3taz, a DES SLSN with a prominent pre-peak ‘bump’. A further advantage of the GP interpolation approach is the treatment and defacto interpolation of the uncertainties for the data points as well as the fluxes themselves giving a confidence region for the measurement of the photospheric temperature and radius. This technique is applied in Angus et al. (in prep) to all spectroscopically confirmed SLSN in the DES sample.

3.4 Summary

In this chapter, I described a number of techniques for analysing and simulating a variety of classes of SNe. I began with SLSNe where I first describe the models used to describe the morphology of their light curves. I discuss the simple expanding black body model for SLSNe before describing the birth and spin-down of a magnetar model, a popular model often used with bolometric light curves. In order to apply this model directly to multi-band photometry, I develop a method of improving the widely used black body approximation for the SED of a SLSN using an absorption template, derived from well-observed examples of the class. I have also presented the tools and statistical techniques

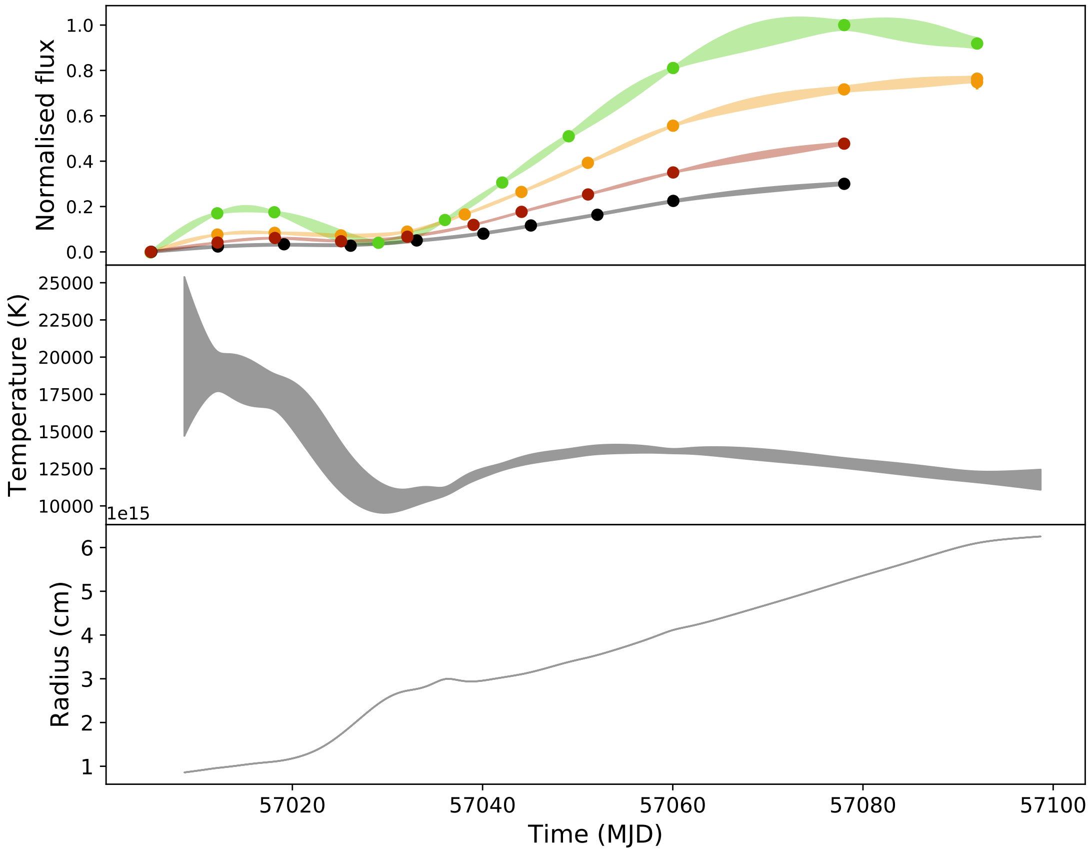

FIGURE 3.10: The *griz* light curve of SLSN DES14X3taz interpolated using GPR. The Planck function was fit to the interpolated photometry in order to determine the photospheric temperature and radius of the SN. Using interpolated data allowed for much higher sampling of the function.

used to perform model fitting on a literature sample of SLSNe as well as simulate them in large numbers in surveys such as SNLS and DES.

I then described the package I developed to perform a similar study of CCSN. I present the steps and packages taken to convert the literature sample of CCSN (both hydrogen-poor and rich) into spectroscopic templates from which we can simulate a large number of similar events in both DES and LSST. This includes packages that allow us to interpolate and extrapolate the light curves of CCSN, match their observed spectra to the model photometry and adjust them to a common phase and flux system. I also discuss the methods (separate for SN Ib/c and SN II) for extending the wavelength coverage of the template spectra in both the IR and UV regimes.

Finally, I discussed Gaussian Process Regression as a powerful technique for a non-parametric approach to the problem of light curve interpolation. I began by describing the background behind Gaussian Processes in the context of our use in time-series interpolation for a later use in ML classification of SNe. I then discuss a number of covariance functions used in this thesis to describe the degree of connection between individual observation. Finally, I discuss an interesting example of the use of GPR outside of the ML where I have demonstrated the power of GPR in the physical modelling of SLSNe

In the following chapters, I endeavour to use the techniques described here in order to calculate the rate of SLSNe (Chapter 4) as well as create a sample of photometrically classified objects in DES (Chapters 5 & 6). All tools described in this chapter form a crucial part of this analysis and show a significant improvement over the previously available approaches as demonstrated by the results I obtained.

Chapter 4

Rate of Superluminous Supernovae at z∼1

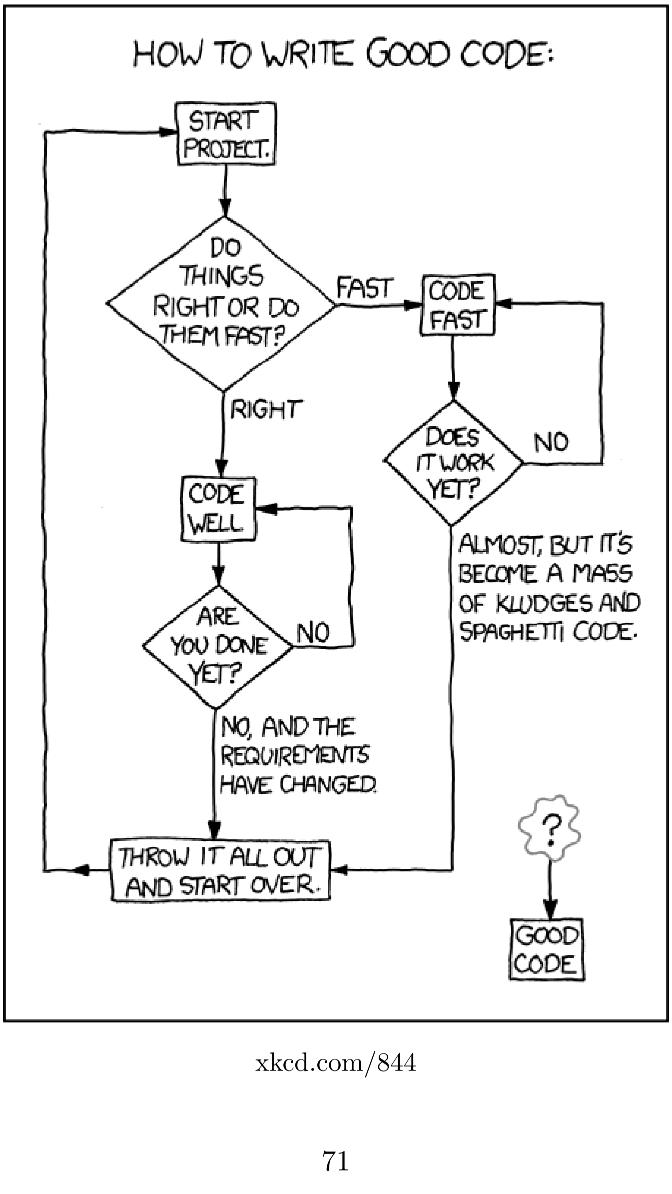

xkcd.com/844

The rate of any transient event is one of its most fundamental properties, providing clues about their origin and evolution throughout the history of the universe. In this chapter, I present the measurement of a volumetric rate of SLSNe at z∼1 measured using the archival SNLS data, providing a unique opportunity to test possible progenitor models. Since their identification, SLSNe have been known to be an extremely rare class of events. The low rate suggests that the origin of SLSNe must be connected with an equally rare progenitor scenario. The motivation behind our measurement is to study the evolution of the rate by bridging the gap between the local and high redshift measurements of the rate.

Prior to this work, there were three published measurements of the rate of SLSNe. A local rate of was calculated using a single SLSN-I event discovered by the Texas Supernova Search (TSS) (Quimby, 2014), giving a value of $\rho_{\mathrm{SLSN}} = 19^{+73}_{-17}$ SNe Gpc^{-3} Yr^{-1} at the volume weighted redshift of z=0.23. The large measurement uncertainty can be attributed to the Poissonian statistics of their small sample, as well as the uncertainty in the detection efficiency driven by the diversity of SLSN population. In contrast to the local value, Cooke et al. (2012) presented a rate of SLSNe at a volume-weighted z∼3 using two SLSNe discovered in the deep stacked SNLS data. They estimate $\rho_{\mathrm{SLSN}} = 400$ SNe Gpc^{-3} Yr^{-1}, however, do not provide an uncertainty estimate which we must assume, making a conservative estimate of 50%. The final of the three measurements was performed by McCrum et al. (2014a) using a sample of spectroscopically confirmed SLSNe in the PanSTARRS. This measurement, however, used a different approach basing the rate of SLSNe on the relative rate and spectroscopic completeness with respect to CC-SNe discovered in the same data set. While I include this measurement for comparison purposes, the values cannot be directly compared.

None of the above experiments measures the rate in the region of z∼1, leading to a gap near the peak of the star formation history of the universe. This region is particularly interesting to us, not only as there is a large number of SLSNe detected at that redshift (e.g Angus et al. (in prep) and Lunnan et al. (2014)), but also as a test for a number of progenitor theories. The rate measured in that volume is fundamental in order to establish whether the rate of SLSNe follows that of the star formation history of the Universe. Demonstrating this could give further evidence to support the models where the birth of a SLSN is connected to a death of a very massive and therefore young progenitor.

SNLS provides a great dataset for this project. With detecting high redshift SNIa as one of its main goals, the SNLS dataset is full of deep and high-quality light curves. The survey has already serendipitously discovered two, high redshift, SLSNe (Howell et al., 2013) while simultaneously having a potential to hide more, not yet identified objects. This work follows a series of similar measurements performed using the same dataset. The rate of SNIa, as well as the point source detection efficiencies, were found by Perrett et al. (2012). The rate of CCSN was measured by Bazin et al. (2009), providing a unique opportunity to compare the rate of SLSNe and CCSN using a deep, homogeneous dataset.

The order of this chapter is as follows. First, I propose a photometric definition of SLSNe based on the modelling of their light curves using the spin-down of a magnetar model followed by a search for missed objects within the SNLS dataset. I briefly introduce the photometric sample of SNLS SLSNe before describing the Monte Carlo simulation used in order to measure the rate and its uncertainties. Finally, I compare the value measured to the previously published results and discuss its significance in terms of the physical origin of the objects as well as their detectability by DES and future surveys. The work presented in this chapter has been published in Prajs et al. (2016).

4.1 Defining a SLSN

The first task in the process of measuring the rate of SLSNe was to develop a method for the photometric selection of optical transients that were to enter our SLSN sample. The earliest definitions of SLSNe relied on their peak luminosity and often defined them as SN with an absolute u-band magnitude of $\mathrm{M}_u < -21$ (Gal-Yam, 2012). This definition is not adequate in our search for two main reasons. Firstly, after that definition was formulated, several examples of events that are spectroscopically similar to SLSNe but that do not pass this arbitrary threshold have been discovered. Some of these events included DES13S2cmm (Papadopoulos et al., 2015) and LSQ14mo (Leloudas et al., 2015b) which both have $\mathrm{M}_u > -21$ despite being spectroscopically consistent with SLSNe and are associated with a very slow light curve evolution. Secondly, a new class of fast and luminous transients with luminosities similar to SLSNe but with a faster light curve evolution as well as different spectroscopic types has recently been discovered (Drout et al., 2014; Arcavi et al., 2016; Pursiainen et al., 2018). Instead of an arbitrary luminosity cut, I use a photometric classification approach based on the modelling of SLSNe using the spin-down of a magnetar model as a simple analytical model that provides a good fit to a sample of confirmed SLSNe.

This approach to classifying SLSNe did have several drawbacks. The use of an analytical model implied that the rate was calculated only for objects which are similar to the sample of confirmed SLSNe, as presented in Section 2.4. It was clear, at the time this work was undertaken, that this would likely not capture all objects of this class. In Chapter 5 I present a more sophisticated and complex approach to this problem, based on an artificial training sample of SLSNe and Machine Learning classifiers, before applying it to DES. In the meantime, however, this work presents a rate of SLSNe based on the best data available at the time that the work was undertaken and measures the rate of a 'classic' or the original sample of SLSN with $\mathrm{M}_u \lesssim$ -21.

4.1.1 Modeling SLSNe

In order to model SLSN, I required two main ingredients: an underlying model for the time-dependent bolometric luminosity of a SLSN and an SED that can convert this bolometric luminosity into time-evolving spectra. This together forms a spectral series from which we can synthesise the photometry in any desired filter and at any desired redshift. This can then be used for comparison to the observed data. For the purpose of this chapter, the exact form or the physical meaning behind the light curve model parameters are irrelevant as, in practice, any model that satisfactorily replicates the observables could be used for this purpose. I briefly recap the model (Section 3.1.3) here, in the context of the modelling of SLSNe in SNLS.

4.1.1.1 Magnetar model

The spin-down of a magnetar model assumes that a collapse of a giant star with an initial mass of $\mathrm{M} > 40\mathrm{M}_{\odot}$ produces a SNIc like explosion whilst giving birth to a magnetar; a highly magnetized neutron star with a rotation period on the timescale of milliseconds (Kasen & Bildsten, 2010; Woosley, 2010; Inserra et al., 2013). The simple toy model assumes a spherically symmetric ejecta and a constant opacity. The free parameters in the model are the time of explosion, t_{expl}, the magnetic field, B_{14}, spin period, P_{ms} and the diffusion timescale τ_M which is directly proportional to the ejecta mass, M_{ej}.

4.1.1.2 Fitting literature light curves

The magnetar model provides a good fit to all the SLSNe that form part of our training sample. Table 4.1 contains the model's best-fit parameters, as well as two additional derived observables which help us to identify the nature of the events without visually inspecting the light curves. These are the peak absolute magnitude in the SDSS u-band filter as well as the rise-time, t_{rise}, of the SN as measured from the explosion to maximum light in the rest-frame u-band. It is important to note here that the absolute magnitude, M_u, are given in the AB magnitude system. The zero-point correction factor between the AB and Vega magnitude system for the u-band filter is: $M_u^{\mathrm{AB}} \simeq M_u^{\mathrm{vega}}+0.9$ (Blanton

Table 4.1: Magnetar model parameters for the sample of 15 published SLSNe.

Name	M_u	$t_{\rm rise}$ (days)	$\tau_{\rm m}$ (days)	B_{14} ($\times 10^{14}$ G)	$P_{\rm ms}$ (ms)	$t_{\rm expl}$ (MJD)
PTF12dam	-21.4	34.72	22.15	0.78	2.85	56044.5
SN2011ke	-21.2	24.84	30.61	3.67	2.13	55647.5
SN2010gx	-21.7	24.56	30.36	3.20	1.54	55247.1
SN2013dg	-21.2	25.37	28.05	3.30	2.75	56412.3
PS1-11ap	-21.8	32.1	20.08	0.79	2.51	55559.0
DES14X3taz	-21.7	47.21	26.16	0.23	1.67	57019.2
PS1-10bzj	-21.2	22.17	18.44	2.65	3.84	55524.0
DES13S2cmm	-20.0	30.7	21.19	1.28	5.29	56509.0
iPTF13ajg	-22.4	31.45	33.41	1.57	1.32	56346.9
07D2bv	-21.1	28.41	36.88	3.40	2.18	54132.4
06D4eu	-21.9	21.48	29.94	3.82	1.00	53956.3

& Roweis, 2006). Therefore, while some of the training samples have $M_u^{\rm AB} > -21$, none have $M_u^{\rm vega} > -21$ which agrees with the previous definition of a SLSN (Gal-Yam, 2012).

4.1.1.3 Defing a SLSN parameter space

Figure 4.1 shows the best-fit magnetar model parameter space. In order to define a region of the parameter space that defines a SLSNe, I enclosed the cluster of our literature points with an ellipsoid. I chose it as the lowest volume, simple geometric body that was consistent with all the SLSN in our training sample. The ellipsoid is defined in terms of the three main fit parameters of the magnetar model, $\tau_{\rm m}$, B_{14} and $P_{\rm ms}$. In the Cartesian coordinate system, a position on any generic ellipsoid can be defined using Equation 4.1.

$$\begin{pmatrix} x \\ y \\ z \end{pmatrix} = \mathbf{A} \begin{pmatrix} R_x \cos(u)\cos(v) \\ R_y \cos(u)\sin(v) \\ R_z \cos(v) \end{pmatrix} + \mathbf{C} \tag{4.1}$$

where **A** is a rotation matrix, **R** is the radius of the ellipsoid and **C** is the position of its center. The following conditions must be satisfied: $-\pi/2 \leq u \leq \pi/2$ and $-\pi \leq v \leq \pi$. I have set up the parameter space such that $\tau_{\rm m}$ lays along the x-axis, B_{14} is along the y-axis and $P_{\rm ms}$ corresponding to the z-axis. Using the Khachiyan Algorithm (Aspvall & Stone, 1980; Khachiyan, 1980), I performed an analytical fit to determine the ellipsoid that best describes the known population of SLSNe, the best-fit ellipsoid to have the following properties:

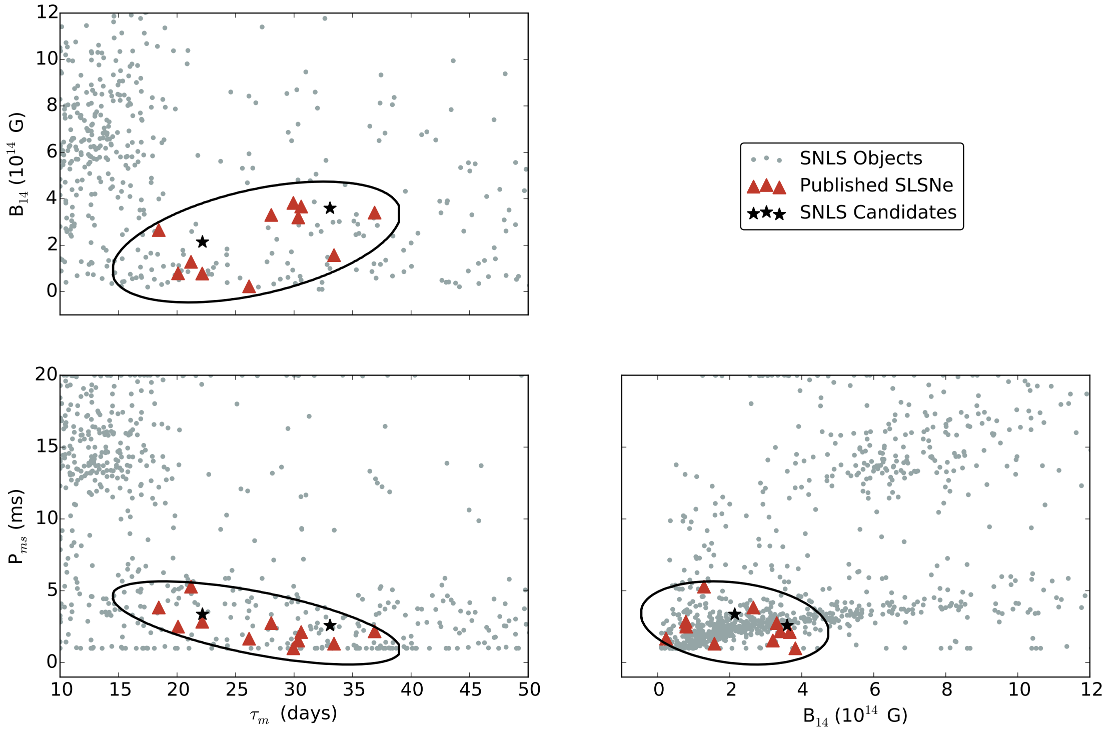

FIGURE 4.1: The $\tau_{\rm m}$–B_{14}–$P_{\rm ms}$ parameter space constructed from the magnetar model fits. The SNLS objects are denoted by grey circles. The ellipses correspond to the two-dimensional projections of the three-dimensional ellipsoid, fitted around the parameter space of the known SLSNe (shown as triangles) to form a region defining them in terms of the model. The SNLS candidates that fall within this parameter space are shown as stars.

$$\mathbf{A} = \begin{pmatrix} -0.184 & 0.575 & -0.797 \\ 0.008 & 0.812 & 0.586 \\ 0.983 & 0.102 & -0.154 \end{pmatrix} \tag{4.2}$$

$$\mathbf{R} = \begin{pmatrix} R_x \\ R_y \\ R_z \end{pmatrix} = \begin{pmatrix} 1.89 \\ 2.17 \\ 11.32 \end{pmatrix} \tag{4.3}$$

$$\mathbf{C} = \begin{pmatrix} 26.76 \\ 2.14 \\ 2.77 \end{pmatrix} \tag{4.4}$$

Figure 4.1 shows the three, two-dimensional projections of this parameter space, populated with our training sample of literature SLSNe.

4.2 Searching for SLSN in SNLS

Having formed a photometric definition of SLSNe in Section 4.1, I now proceed to describe the steps undertaken in order to identify any potential missed SLSNe in SNLS. My approach was based on fitting the magnetar model to SNLS light curves and comparing their best-fits to the parameter space defined by the training sample. In the ideal case, we would first like to test the definition against an independent test sample of objects that were not used in forming the definition. The number of known SLSN events is too small to allow us to split it into a training and test samples. I, therefore, make the assumption that the parameter space in Figure 4.1 is defined by a representative sample of events. This provides a further motivation to seek a more elegant and robust solution for any future search of SLSN such as the one performed on the DES dataset in Chapter 5. Note that both the fitting method and the definition of a SLSN-like event presented in this chapter do not make any assumption about the luminosity of the event. This makes it entirely possible for fitted events to have $M_u > -21$ and still be classified as SLSNe, broadening the definition of SLSN into potentially previously unexplored parts of the parameter space. Furthermore, the inverse is also true where some events with $M_u < -21$, including those with a relatively short diffusion timescale, $\tau_{\rm m}$, giving rise to a faster evolution, are shown to be inconsistent with SLSNe. This natural consequence of the technique used here is that it leads to a purer sample of SLSNe than an arbitrary magnitude cut.

4.2.1 Magnetar model fitting

With the model and definition of SLSNe in place, I then applied the same technique to the sample of SNLS transients. SNLS detected 4949 transient objects in total (Perrett et al., 2010). This included many objects that were visually designated as active galactic nuclei (AGN) and variable stars, as well as supernovae. In order to perform the fitting on the sample, I first matched each object with a redshift where known. 1694 objects in the transient catalogue have spectroscopic redshifts, either from spectra of the transients or of the host galaxy (Perrett et al., 2012). The redshift association here is trivial as the spectroscopic measurements directly target either the SN or its host galaxy.

As previously described in Section 2.1.5, where a spectroscopic redshift is not available, I use photometric redshift estimates. SNLS transients were associated with potential host galaxies by selecting the nearest galaxy within a radius of 1.5". This provided photometric redshift information for a further 1527 events. As the photometric redshift estimates are less precise than their spectroscopic counterparts, I do not use them directly. Instead, I iterate over a range of redshift values spanning the photometric redshift uncertainties between the lower to upper uncertainty band in steps of $\Delta \mathrm{z} = 0.04$.

At this stage of the analysis, 1728 candidates remain with no redshift information. Due to the difference in depth of the SNLS deep stack compared to that of the science images we expected fewer objects to be considered as 'hostless' in the sample since SNLS should be able to measure photometric redshifts for all but the very faintest host galaxies. I carried out an inspection these objects both visually and using simple statistics (including the number of detected bands, number of detections per band and the time elapsed between detections) and found that a large number of these objects were, in fact, likely to be false detections that incidentally matched the SNLS real-time detection criteria (Perrett et al., 2010). This inspection showed that only 292 of these objects have multiple detections in multiple bands and are therefore likely to be real. For this remaining sample, I iterate over a broad range of redshifts ($0.2 \leq \mathrm{z} \leq 1.6$ in steps of $\Delta \mathrm{z} = 0.1$) but otherwise treat them identically to objects with a known redshift.

Once the events were associated with their respective redshifts, I then fit the SNLS sample to the magnetar model. During the fitting process, I apply the same quality cuts as for the SLSN training sample. I have excluded objects with less than two detections in at least three bands between the best-fit explosion date and maximum light, and a further two detections in at least three filters between maximum light and +30 days. For the purpose of this work, I consider a detection to be $\geq 5\,\sigma$ in the real-time photometry. Amongst the 4949 SNLS transients only 2097 pass the final data quality cuts. Their best-fits to the magnetar model are shown in Figure 4.1.

4.2.2 Candidates

While the magnetar model is flexible, capable of fitting a variety of light curve morphologies, it is not a good fit to for the majority of the SNLS objects. A simple χ^2 test is sufficient to remove a large number of these poor fit quality objects. I apply a conservative cut at a χ^2 per degree of freedom (χ^2_ν) of 20. I chose such a large value of χ^2_ν in order to retain all SLSNe, including these that might be associated with pre-peak 'bumps' (Nicholl & Smartt, 2016; Nicholl et al., 2015b; Smith et al., 2015). Such objects are well represented by the magnetar model in the 'main' part of the event, but it cannot account for the extra undulations. Thus the goodness-of-fit is not ideal when taking into account a light curve for the whole season, not reduced to fit the period of the SN.

Of the SNLS objects that pass our data quality and χ^2_ν cuts, four lay within the parameter space of SLSNe as defined in 4.1. This includes the two spectroscopically confirmed

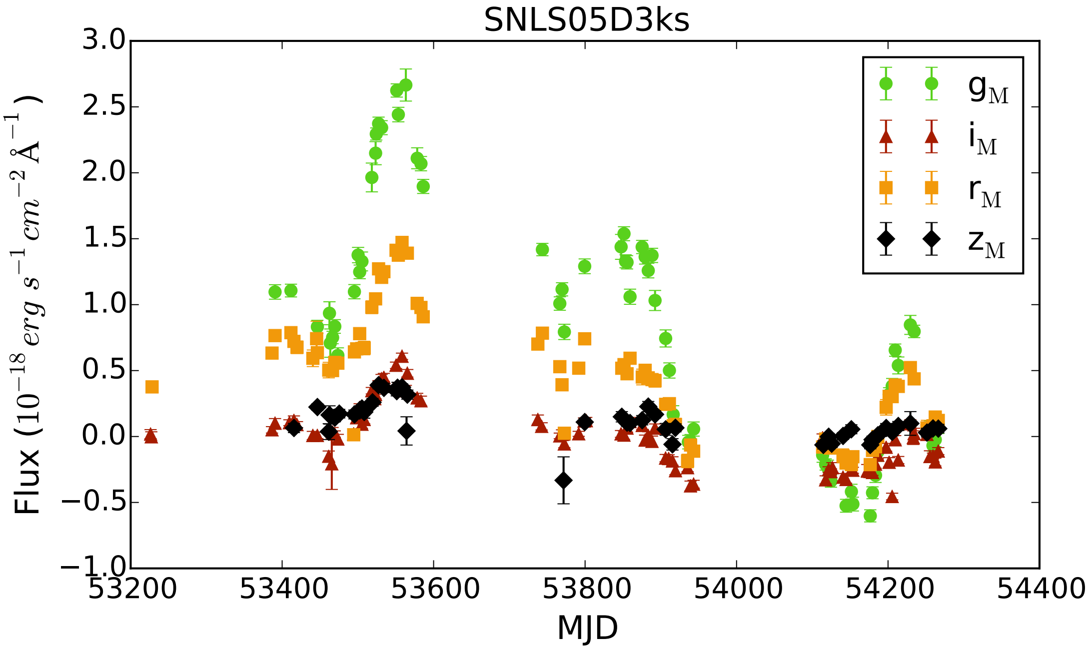

Figure 4.2: The g_M, r_M, i_M, z_M multi-season light curve of SNLS-05D3ks. This transient is found within the SLSN parameter space (Figure 4.1), but does not pass visual inspection as it shows clear signs of multiple maxima.

events from Howell et al. (2013) that were part of our training sample. The other two were SNLS-05D3ks and SNLS-07D3bs, I measured the multi-season light curves using the custom PTFPHOT pipeline (described in Chapter 2) to allow us to visually inspect the objects and search for signatures of any long-term variability or detections prior to, or sufficiently after, the putative supernova event. This process of visual inspection eliminates SNLS-05D3ks which shows clear multiple maxima spanning three years as seen in Figure 4.2 (), leaving us with just a single, new SLSN-like candidate: SNLS-07D3bs.

4.2.3 SNLS-07D3bs

SNLS-07D3bs is identified as a SLSN candidate between $0.6 < z < 1.2$ based on its host galaxy photometric redshift estimate. The best-fit magnetar model for the object is obtained at z = 1.0. SNLS-07D3bs was spectroscopically observed on the 17th April 2007 using the Keck/LRIS instrument. This data was never published as no spectral classification was obtained at that time. The data was however presented in a PhD thesis by Fakhouri (2013).

At the time the observations of SNLS-07D3bs were made, the SLSN class was not yet recognised and no SLSN spectral templates were available for comparison with the data (For the same reason, the SLSNe previously identified in SNLS by Howell et al. (2013) were not identified as objects of interest until several years after their initial detection).

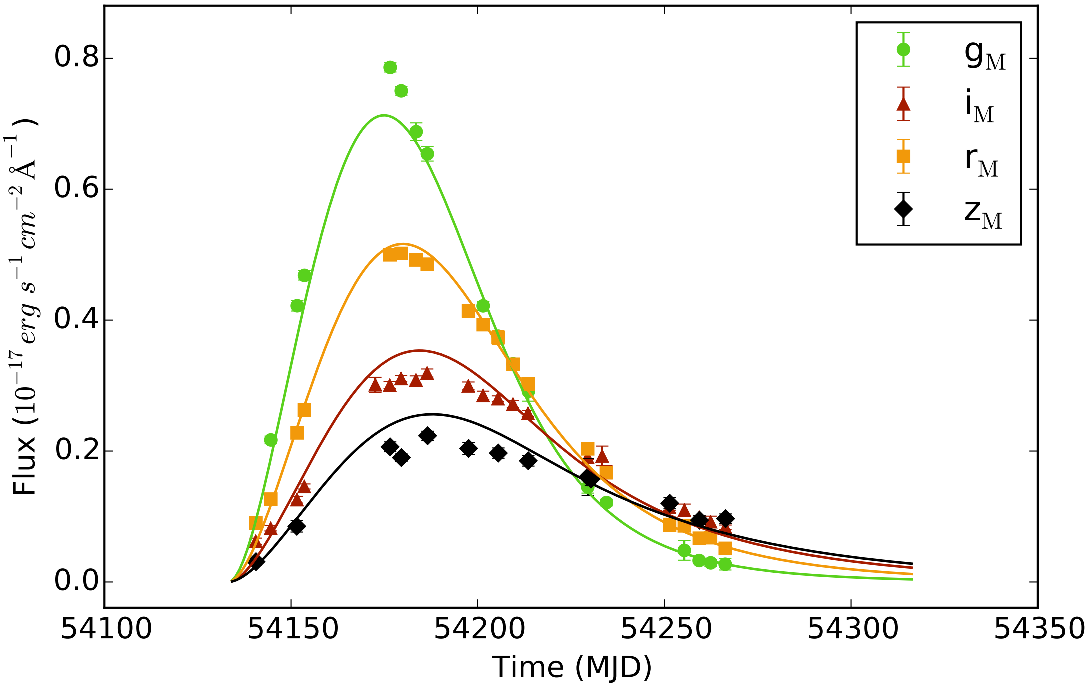

FIGURE 4.3: The g_M, r_M, i_M, z_M light curve of SNLS-07D3bs overplotted with the best-fit magnetar model at $z = 0.757$. The candidate shows a good agreement with the model.

Using the SUPERFIT spectrum identification tool (Howell et al., 2005), the spectrum of SNLS-07D3bs was re-analysed by fitting all available SN templates at a broad range of redshifts outside of the photometric estimate. The data are noisy with a signal-to-noise ~ 7 as observing conditions were quite poor. Despite this, I find the best spectral match to be to the SLSN iPTF13ajg at $z = 0.757$ as can be seen in Figure 4.4. While this is clearly an uncertain spectral classification, there is no evidence from the spectrum that the object is not a SLSN, particularly as the best match is an event of that type. The magnetar model also provides a good fit at that redshift as seen in Table 4.2. The host galaxy, located at RA=14h 21m 50.466s, Dec=+53° 10' 28.58", is detected in the SNLS deep stack images (Ilbert et al., 2006), but is very faint, with AB magnitudes of (u_M, g_M, r_M, i_M, z_M) = (26.61 ± 0.49, 26.13 ± 0.16, 25.67 ± 0.13, 25.18 ± 0.11, 25.19 ± 0.37). Combining the spectral and magnetar model fitting, as well as a faint host galaxy, matching the properties expected of most SLSNe, provided us with sufficient evidence to consider SNLS-07D3bs to be the third SLSN detected by the real-time pipeline of SNLS.

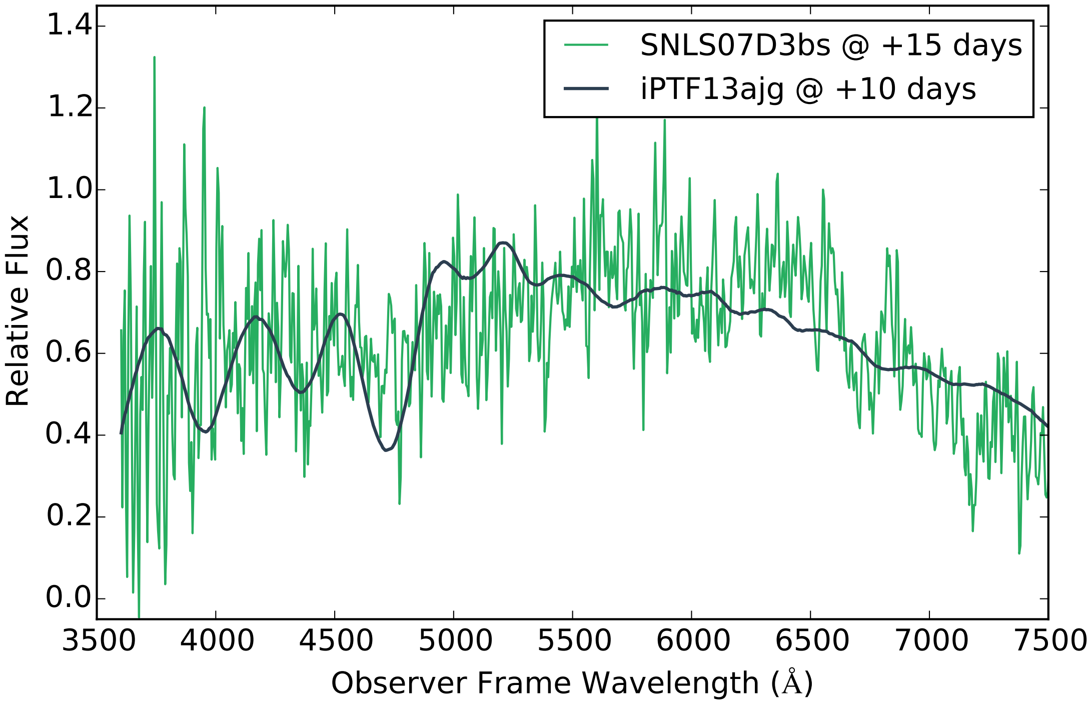

FIGURE 4.4: The spectrum of SNLS-07D3bs from Keck/LRIS, taken 15 rest-frame days after maximum light. The signal-to-noise of the spectrum is low preventing a definitive classification; however, the spectrum is consistent with a SLSN at around $z = 0.76$. Weak galaxy emission lines are consistent with $z = 0.757$.

TABLE 4.2: Magnetar model parameters for the new SNLS SLSN candidate: SNLS-07D3bs.

Name	M_u	$t_{\rm rise}$ (days)	$\tau_{\rm m}$ (days)	B_{14} ($\times 10^{14}$ G)	$P_{\rm ms}$ (ms)	$t_{\rm expl}$ (MJD)
SNLS-07D3bs	-20.9	27.2	23.7	2.28	3.81	54132.5

4.3 The rate of superluminous supernovae

In the previous sections, I have outlined our approach to making a suitable definition for SLSNe before applying it to a sample of detected by the SNLS. This resulted in identifying a sample of three SLSNe including two previously known objects and a new, previously unclassified example; SNLS-07D3bs. In this section, I describe the method used to calculate the volumetric rate of SLSNe, $\rho_{\rm slsn}$, implied by these detections. First, I describe the method used for this calculation and the reasoning behind our use of a Monte-Carlo simulation over a purely statistical approach. I then discuss the reasoning behind our choice of the search volume before presenting the rate calculation and the result.

4.3.1 Defining a rate

ρ_{slsn} can be defined as a sum over the number of SLSNe, N, found in a given comoving search volume, V, over a search duration, t, weighted by the inverse of the detection efficiency, ϵ_i, of detecting each event. This can be summerised using Equation 4.5:

$$\rho_{\mathrm{slsn}} = \frac{1}{V} \sum_{i}^{N} \frac{(1+z_i)}{\epsilon_i t_i}. \tag{4.5}$$

The factor $(1+z_i)$ corrects for time dilation. The detection efficiency ϵ_i is a statistic describing how each SLSN should be weighted relative to the whole population. In other words, $1-\epsilon_i$ gives the fraction of similar SLSNe that exploded during the search period but were missed by the survey due to, for example, search inefficiencies. The detection efficiency is a vital, and simultaneously the most difficult part, of the computation.

4.3.2 Detection efficiency

The full treatment of a detection efficiency for any survey is a very complex problem with many aspects of the survey to be considered including the cadence, image quality, limiting magnitude amongst other. Frohmaier et al. (2017) shows a recent example of such a comprehensive study performed with the aim of calculating the local volumetric rate of SNIa in PTF. Our SLSN detection efficiencies are based on a similar analysis by Perrett et al. (2010), who carried out a study of the detection efficiencies and selection biases of SNIa in SNLS and subsequently calculated a rate of those events in Perrett et al. (2012). In this study, several million fake SNIa were placed in the SNLS science images, with the correct temporal evolution, and passed through the SNLS real-time detection pipeline. The recovery efficiencies of these SNe Ia could then be estimated. Although these results were produced using a particular model of a particular supernova type, at a more basic level they also provide the recovery efficiencies of point sources in the SNLS data as a function of magnitude in every i_M-band image that SNLS took, and it is these more basic data that we use in this study.

4.3.3 Method

In this work, I reverse the common approach to supernova rate calculations, such as the ones used by Perrett et al. (2012) and (Frohmaier et al., 2017). Instead of calculating the rate of SLSNe starting with the number of detected objects, I calculate the probability that a given initial value of ρ_{slsn} leads to an eventual detection of three SLSNe in the survey. This method is capable of producing a non-Gaussian uncertainty estimate as a by-product of the calculation as the result is presented in form of a probability distribution (Figure 4.6). The uncertainties can be simply quoted as the 1σ confidence region of this distribution.

To simulate the SLSN population in SNLS, I use a Monte Carlo approach. I 'explode' fake SLSNe randomly within the SNLS search period and search volume, and create artificial SLSN light curves on each epoch corresponding to the SNLS observations, including the effect of $1 + z$ time dilation. As a result, it is possible to estimate the i_M apparent magnitude on each epoch, which is then compared to the point-source recovery statistics on that epoch to give the probability of detection. I combine all of these individual probabilities to give us an overall detection probability per object.

4.3.4 Search volumes

The effective SNLS search areas for each field, from which the search volumes can be calculated, was found accurately in Perrett et al. (2012) giving an effective total search area of $3.56\,\mathrm{deg}^2$. The volume is calculated by considering the redshift range to which our search was sensitive. The four observing fields cannot be considered as identical as there is a small variation in the detection efficiency amongst the fields. The observing season in the D3 field was longer in comparison to the other fields while D1 and D2 had on average, marginally deeper exposures.

At the low-redshift end, the search volume is set by the redshift at which a SLSN would become saturated in the SNLS data. At the high-redshift end, the volume is set by the redshift at which we are no longer able to recover a SLSN event, i.e. a SLSN would fall below the detection limit of the survey. Figure 4.5 illustrates the redshift range over which the search for SLSNe is sensitive to in SNLS, showing the recovery efficiency as a function of redshift for the three events identified in Section 4.2.2. For events at $\mathrm{z} < 0.2$, the efficiency drops rapidly due to saturation effects setting $\mathrm{z} = 0.2$ as the lower redshift limit. At the upper redshift limit, I choose $\mathrm{z} = 1.6$. Although some events similar to SNLS-06D4eu are detectable at $\mathrm{z} > 2$, the fainter events like SNLS-07D3ds would become undetectable in some of the SNLS search fields at $\mathrm{z} < 1.6$.

4.3.5 Monte Carlo simulation

I begin each Monte Carlo simulation with an input ρ_{slsn} value. From this, I calculate the number of SLSNe that would have occurred within the SNLS search area over the redshift range to which we are sensitive ($0.2 < \mathrm{z} < 1.6$) in bins of $\Delta\mathrm{z} = 0.01$. I assume

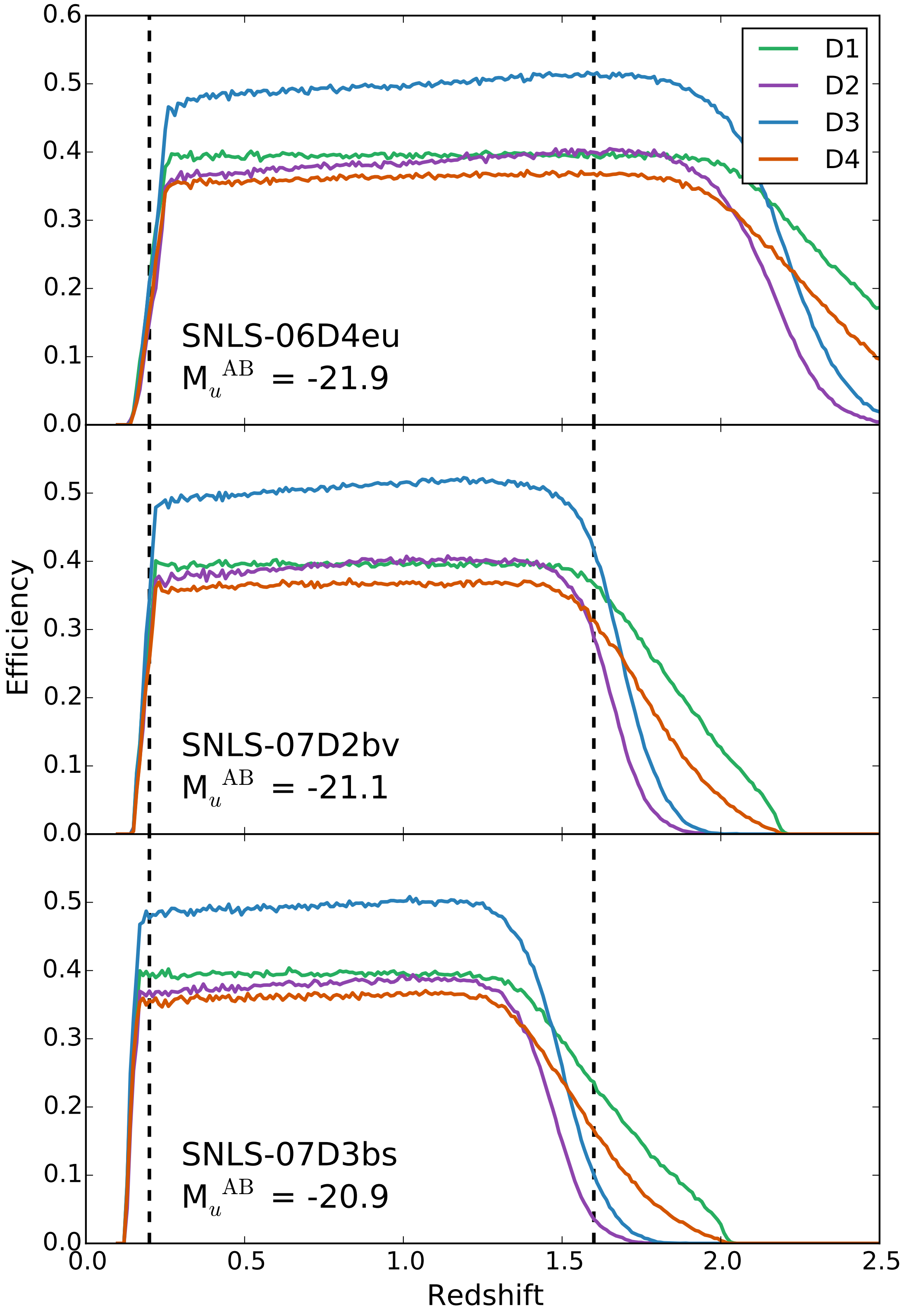

FIGURE 4.5: The redshift range to which our SLSN search is sensitive to, as a function of the four SNLS search fields. The figure shows the recovery efficiency of three different SLSNe as a function of redshift, with each line corresponding to a different search field. The efficiency includes the same data quality cuts as used in the training sample in Section 4.1.1.3 and the SNLS candidate selection in Section 4.2.2. The vertical dashed lines at z = 0.2 and z = 1.6 illustrate the final redshift range used in our Monte Carlo rate calculations.

that this rate does not evolve within the redshift range considered in our simulation. However, this assertion is later tested in Section 4.3.6. The artificial SLSNe are then assigned a random spatial position (and consequent Milky Way extinction), redshift, host galaxy extinction and physical parameters drawn from the magnetar model parameter space derived from our training sample (Figure 4.1). A random explosion epoch during the SNLS search period is assigned to each event. From this, the synthetic photometry was calculated on every epoch corresponding to a SNLS observation.

Using the point-source detection efficiencies of Perrett et al. (2010), I calculate the probability of detecting each SLSN on every epoch of i_M data and combine the probabilities to give the total probability of discovering each object. In order to be considered detected, I enforce that each artificial SLSN must pass the same data quality cuts as both our training sample in Section 4.1.1.3 and our real sample of SNLS candidates in Section 4.2.2. I repeat the entire simulation 100,000 times over an input $\rho_{\rm slsn}$ range of $5 \leq \rho_{\rm slsn} \leq 500\,{\rm SNe\,Yr^{-1}\,Gpc^{-3}}$.

Figure 4.6 shows the probability of three SLSN events being detected in our simulations as a function of the input rate. A log-normal distribution is fitted to the simulation results and used to smoothly determine the peak of the distribution as well as the 1σ confidence regions. From this, we find the rate of SLSNe at $z = 1.13$, which is the volume-weighted centre of the $0.2 < z < 1.6$ range, to be $\rho_{\rm slsn} = 91^{+76}_{-36}\,{\rm SNe\,Yr^{-1}\,Gpc^{-3}}$.

4.3.6 Rate assuming a SFR distribution of SLSN

As SLSNe are a likely consequence of a collapse of a giant star with an intrinsically fast stellar evolution, it is expected that the rate of SLSNe should follow closely that of their birth, i.e the cosmic star formation rate. An expected consequence of this would be that a larger proportion of SLSNe are found at high redshift compared with a non-evolving population. I investigate the consequence of this effect on our final rate by repeating the Monte Carlo simulation, instead of drawing the SLSNe from a redshift distribution that follows the cosmic star-formation history as taken from Hopkins & Beacom (2006) and described in more details in Section 4.3.6. For the value pivoted at z=1.13, as in the case of the flat distribution, I find $\rho_{\rm slsn} = 98^{+82}_{-39}\,{\rm SNe\,Yr^{-1}\,Gpc^{-3}}$. This is very close to the original result and, considering the uncertainties, a negligible difference. Thus our final rate averaged over the redshift range we have considered, is not sensitive to the assumed rate evolution in our simulation. One possible explanation of this is that the relative uniformity of our detection efficiency as a function of redshift within our search volume negates the effects of the redshift evolution (Figure 4.5).

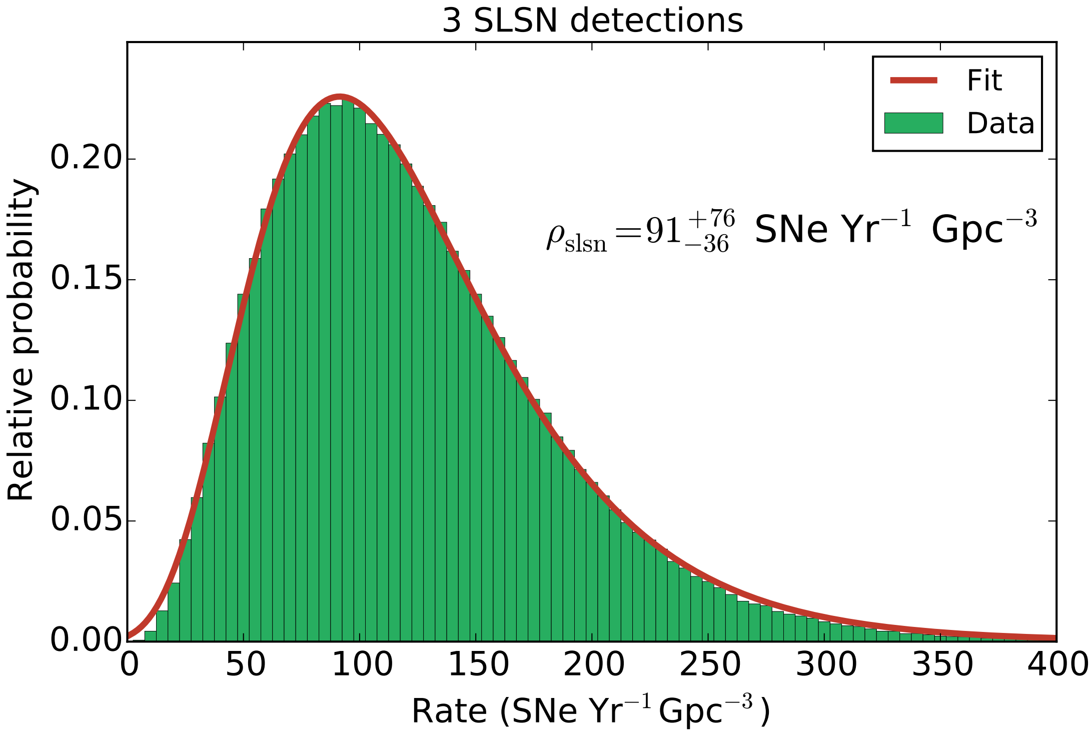

FIGURE 4.6: The probability distribution of the volumetric rate of SLSNe for the three SLSN candidates over the duration of SNLS at $0.2 < z < 1.6$, as determined by our 100,000 Monte Carlo simulations. A log-normal distribution is fit to the data (red line) to estimate the peak of the probability distribution and the uncertainties, quoted as the 68% confidence region.

4.4 Discussion

Having calculated the rate of SLSNe at an intermediate redshift, it is now interesting to compare the value to other measurements and study its evolution as a function of redshift.

4.4.1 Rate Evolution with Redshift

Figure 4.7 shows the SLSN rate calculated in this chapter compared with the values published by Cooke et al. (2012), Quimby (2014) and McCrum et al. (2014a). The volumetric rate increases as a function of redshift with the extent of this observed evolution consistent with the evolution in the cosmic star-formation history observed over the same redshift range (Hopkins & Beacom, 2006). This is, perhaps, an unsurprising result, as SLSNe are thought to originate from the death of very massive and hence short-lived stars. However, it is important to note here, that we are not able to discriminate between the evolution that follows the star formation history, and one with

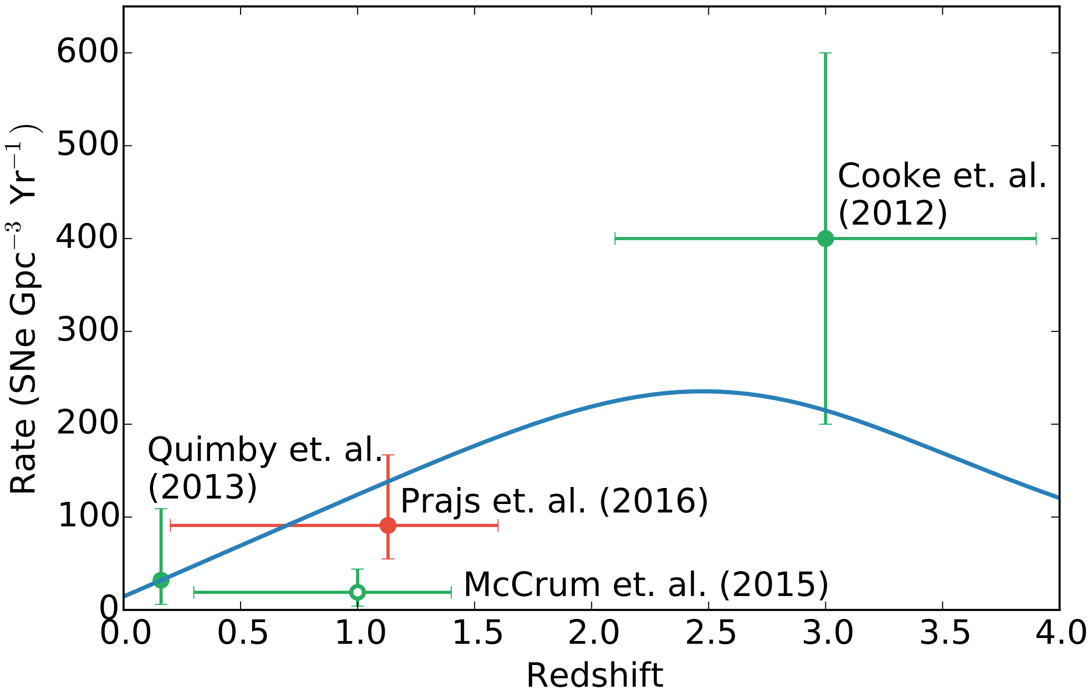

Figure 4.7: The evolution of the volumetric SLSN rate as a function of redshift. I compare my measurement to those by Cooke et al. (2012), Quimby (2014) and McCrum et al. (2014a) for comparison. The McCrum et al. (2014a) result is marked by an open circle to highlight that it may not be directly comparable with the other measurements as it is derived by a comparison to the rate of core-collapse supernovae and is not a direct measurement. The observed evolution is consistent with that of the SFH over the same redshift range; I over-plot in blue the parametrisation of the cosmic SFH of Hopkins & Beacom (2006), normalised to the low-redshift SLSN-I rate obtained by Quimby (2014).

the same evolution up to $z = 1.5$ but followed by a peak at a much higher redshift; the $z > 1.5$ measurement is quite uncertain.

In fact, a higher-redshift peak of the rate may be expected as SLSNe almost exclusively explode in galaxies that are low-mass, compact dwarfs (Neill et al., 2011; Lunnan et al., 2015), and that are metal-poor and strongly star-forming (Chen et al., 2013; Lunnan et al., 2013; Leloudas et al., 2015a). One popular interpretation of this is that the low metallicity must play a role in the formation of SLSNe, which is consistent with the low metal content inferred from their UV spectra (Mazzali et al., 2016). This scenario would also predict a volumetric rate evolution that follows both the cosmic SFH and cosmic chemical enrichment. The possibility of testing the origins of SLSNe and the role of metal enrichment to their formation gives one of the strongest motivations behind the future studies of their rates at $z > 2$.

4.4.1.1 Comparison to the rate of CCSN

Comparing the rate of SLSNe to that of CCSN is another interesting test which can inform us about their origin. Using SLSNe discovered by the Pan-STARRS medium-deep survey over $0.3 \leq z \leq 1.4$, McCrum et al. (2014a) measure the relative rate of SLSNe to be between $3^{+3}_{-2} \times 10^{-5}$ and $8^{+2}_{-1} \times 10^{-5}$ that of the core-collapse supernova rate, $\rho_{\rm cc}$. We use the SNLS $\rho_{\rm cc}$ measurement at $z \sim 0.3$ of $1.42 \pm 0.6 \times 10^{-4}$ SNe Gpc $^{-3}$ yr $^{-1}$ (Bazin et al., 2009), and extrapolate it to $z = 1.13$, assuming it tracks the cosmic SFH, increasing the rate by a factor of 2.62. Our own absolute SLSN rate can then be expressed as rate relative to that of core-collapse SNe, which we find to be $2.2^{+1.8}_{-0.9} \times 10^{-4}$ of the $\rho_{\rm cc}$. This is higher than, but consistent with, the relative rate of McCrum et al. (2014a).

4.4.2 Host Galaxies of SNLS SLSNe

The host galaxies of SLSNe play a key factor in their study. Besides playing a factor in determining their origins they also provide an observable that could act as a further confirmation for a photometrically selected object. Figure 4.8 shows the distribution of SLSN host-galaxy stellar masses as measured by Lunnan et al. (2014). We use the ZPEG photometric redshift package (Le Borgne & Rocca-Volmerange, 2002) with the SNLS multi-waveband g_M,r_M,i_M,z_M host galaxy photometry to estimate the stellar mass for SNLS-07D3bs. We are not able to derive host galaxy stellar masses for SNLS-06D4eu and SNLS-07D2bv using the SNLS deep stacks due to the galaxies faintness and the lack of infrared (which correspond to the rest-frame optical) data. We instead use values obtained by Leloudas et al. (2015b) and Schulze et al. (2016). The host stellar masses for all three of our candidates agree with the published SLSN-I host stellar mass distribution as shown in Figure 4.8.

4.5 Summary

In this chapter, I presented the steps undertaken in order to calculate the rate of SLSNe at z∼1 using the archival SNLS light curve data. The first step in this process was to define the SLSN based on their photometric properties. I used a sample of literature objects and the spin-down of a magnetar model to form a definition based on selecting a region of its parameter space occupied by SLSN.

Upon fitting all SNLS transients with the model and comparing it to the definition of SLSNe, I found two potential candidates. Upon closer visual inspection, one object was

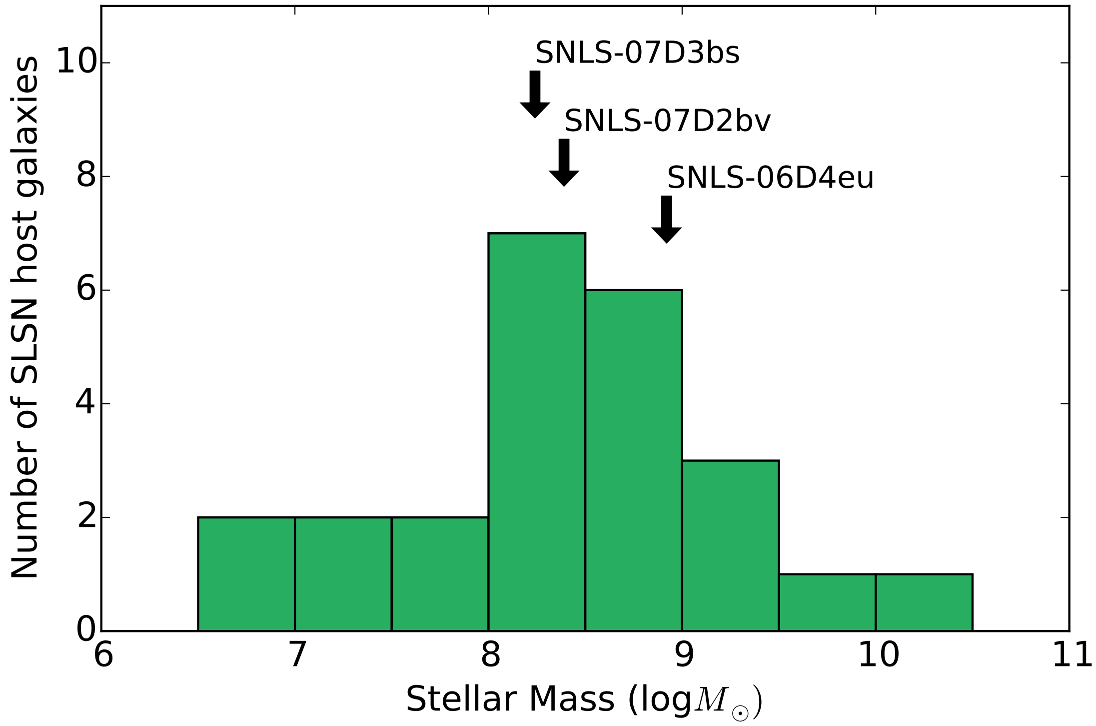

FIGURE 4.8: The stellar mass distribution of SLSN host galaxies plotted using the data from Lunnan et al. (2014), showing the consistency of SNLS07D3bs with the rest of the population. The lack of detections for the hosts of the high redshift candidates is consistent with being associated with low mass galaxies, found below the detection limit of SNLS at their redshifts.

most likely an AGN while the second remained as a likely, previously unclassified SLSNe. Using archival spectra, I found its redshift to match that predicted from the magnetar model fitting confirming my photometric classification.

Using the newly discovered object as well as two previously published, spectroscopically confirmed SLSNe, I built a Monte Carlo simulation of SNLS aimed at determining their most probable rate that would lead to the detection of three objects in the SNLS over the duration and volume searched. I measured the vale to be, $\rho_{\rm slsn} = 91^{+76}_{-36}\,{\rm SNe\,Yr^{-1}\,Gpc^{-3}}$ or $2.2^{+1.8}_{-0.9} \times 10^{-4}$ of the $\rho_{\rm cc}$, the rate of CCSNe. Comparing this to previous, similar results I found that the evolution of the rate of SLSNe is consistent with that of the evolution in the cosmic star formation history, confirming that the origin of these objects is likely an young population of massive stars.

Chapter 5

Classifying Superluminous Supernova using Machine Learning

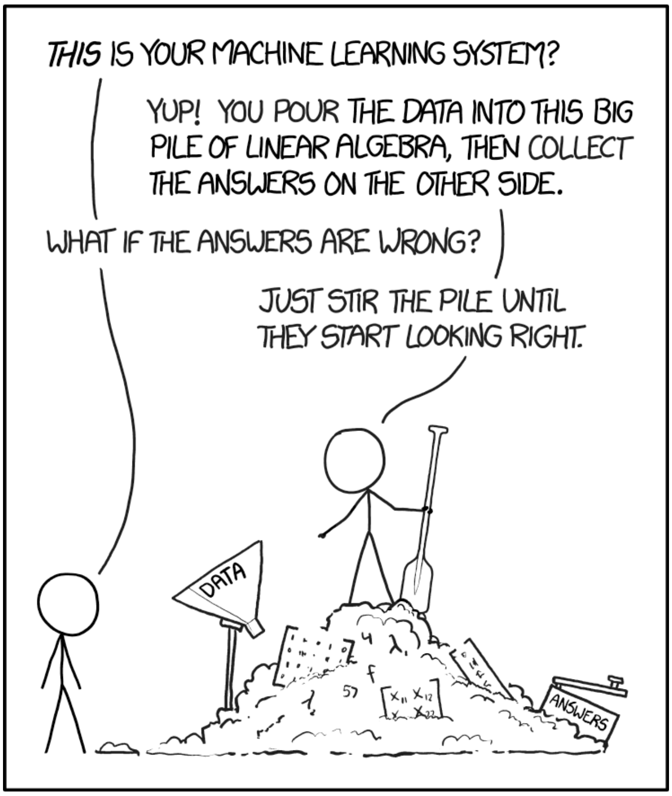

xkcd.com/1838

SN classifications, focusing particularly on the selection of SLSNe, formed the underlying theme of this thesis. In Chapter 4, I established a definition of SLSNe in terms of the parameter space of the spin-down of a Magnetar model, later used to photometrically classify one SLSN in the SNLS archival data. In this chapter, I begin by describing the application of this previously successful technique to the DES dataset, performed in real-time during the seasons two and three of DES. This included both the manual scanning of SNe and combining it with the Magnetar model fitting. While successful in identifying several candidates, and later spectroscopically confirmed, SLSNe, a number of misclassifications highlighted a need for a more robust approach.

In recent years the field of astronomy entered a new data analysis renaissance, utilising Big Data tools and Machine Learning techniques to extract more from archival data and prepare for the arrival of new surveys such as Gaia, ZTF, LSST and SKA that are expected to produce staggering amounts of data, exceeding everything that we were familiar with in the past decades. Beside creating difficulties in their analysis, the streaming, handling and storing of the data is also a serious issue requiring state-of-the-art facilities and tools. Following in the footsteps of this revolution, I endeavoured to apply some of the latest ML techniques that are proven in other fields as well as in real-world applications, to the problem of SN classification.

To date, there has been a number of studies aiming to classify SNe with the help of ML. In this thesis, I am focusing only on the studies classifying the light curves of SNe and not point source classification pipelines such the once used recently in DES (Goldstein et al., 2015) and Suburu (Saxena et al., 2018). Amongst a number of similar works (Karpenka et al., 2012; Möller et al., 2016; Charnock & Moss, 2016) the most thorough and in-depth study is presented in Lochner et al. (2016). In their work, a number of models are used to extract a broad range of light curve features. They also provide a comparison of a number of Supervised ML algorithms and discuss their merits in terms of SN classification. While thorough in their analysis, their approach is not ready for deployment in a real survey. The training sample used in their analysis is the SPCC dataset containing a sanitised sample of SNe only. In a survey such as DES, we are faced with sample heavily contaminated by other classes of transients.

The use of the SPCC dataset by Lochner et al. (2016) containing only 2000 SNe, weighted to match their expected spectroscopic classification rates, is one of their greatest drawbacks. In this thesis, I aim to provide the first SN classification approach utilising a large (tens of thousands of objects for each subclass), artificially generated sample of objects. With the size of the training sample, I tackle the common issue with overfitting for the less common subclasses of SNe. Furthermore, by placing the SNe uniformly throughout the DES observing season and at a wide range of redshifts, I produce realistic survey imperfections, including objects which suffer from season edge effects and low S/N.

One of the greatest differences between all previous studies and this thesis is the family of ML algorithms used. Lochner et al. (2016) used the SALT2 model and wavelet decomposition, in a process commonly referred to in ML as Feature Extraction or Feature Engineering, to extract a set of parameters that describe the light curve. These are then fed into the ML algorithms to produce their classifications. In this thesis, I use Convolutional Neural Networks (CNN), a powerful technique which dominates the world of commercial ML solutions. CNNs, described in detail in Section 5.4.1, use the data directly as they build their own bespoke feature sets as part of the learning process. The use of such a complex ML tool is only possible thanks to the extent of the training sample along with the data augmentation described in Section 5.3.

In this chapter, I describe the process of creating an artificial training sample of SNe for a majority of their dominant subclasses, based on the tools developed in Chapter 3, as well as AGNs and noise spikes which form the majority of transients detected by DES. Following from this, I describe the steps taken to apply the survey noise model to the otherwise smooth, simulated data before interpolating and augmenting it with the help of GPR, described in Section 3.3. Finally, I discuss the use of the CNN framework to provide a photometric classification for all transients detected by DES in the first four years of its operations.

5.1 Traditional Approach to Searching for SLSN in DES

Before applying the ML framework to the problem of selecting SLSN, I have used the magnetar model approach originally developed in Chapter 4 for the use of the SNLS data. This gave us some encouraging results, providing the classification for several SLSNe in the DES data, however, the subsequent discoveries of a number of objects that do not fit the known models, including cases such as DES15S2nr, demonstrated the need for a different approach.

5.1.1 Magnetar Model Fitting

A major difference between the approaches used to identify SLSN in DES and that of SNLS is the completeness and the stage at which the data enters the analysis pipeline. In Chapter 4 I applied the techniques retrospectively to archival data. This, outside limited cases suffering from season edge effects, gave me a sample of near complete light curves that could be modelled with a much higher confidence rate. In DES, I attempted to model the light curves during their early rise phases. This was a constraint dictated not only by our desire to classify the objects at the earliest possible phase (as early time spectra of SLSNe are still not sufficiently abundant) but also due to the computational resources required to fit all the light curves in real-time. Despite a number of optimisations applied to our fitting routine (Section 3.1.3), I was limited to fitting data detected within the last three to four observing epochs. As it is not possible to constrain such a complex model with less than three epoch of multi-band data, I have delayed the analysis of each object until the first epoch where at least three observations, in a minimum of three photometric bands, are available. If the object remained active (i.e detected in the latest of the three epochs), I attempted to fit the magnetar model to it and compare the result against the definition of SLSNe. I have subsequently repeated this step, up to the maximum of four times, when new data became available. At that stage, if the object did not match our definition in any of the epoch of fitting it was discarded.

5.1.1.1 Problems

A number of problems revolving around this approach were uncovered during the DES runs that resulted in some number misclassifications of SLSNe, both as true-negatives and false-positives.

'Bumpy' SLSNe One of the drawbacks of the rules put in place in order to optimise the fitting process and reduce the number of false detections being passed through the classification pipeline is the rejection of some objects, most predominantly DES15C3hav, which show a slowly evolving pre-peak bump close to the detection limit of the survey (Angus et al; in prep). In the case of DES15C3hav, the early activity was only detected in two consecutive epochs before the S/N of the light curve dropped considerably for a number of weeks prior to the rebrightening at the onset of the main SLSN event.

Similarly, while no such cases have been identified, it is also likely that a pre-peak bump, similar to that found in DES14X3taz (Smith et al., 2015), would have been excluded by these cuts as its initial seven epochs do not give a good fit to the magnetar model and do not fit the definition of SLSNe.

Faint SLSNe One of the most interesting discoveries made about the population of SLSNe is the abundance of objects which, while spectroscopically consistent with the published population of SLSNe, are found at absolute luminosities lower than previously expected, as faint as M∼-19. From Inserra et al. (2017) and Nicholl et al. (2014, 2017), we know that the evolution of SLSNe, both in terms of the rise and decline time, is strongly linked with their luminosity resulting in the different morphology of the fainter events. As no such objects were known at the time, they were not present in the sample used in Chapter 4, resulting in a strong bias of the magnetar model definition against such objects. This resulted in a number of fainter SLSNe (for example DES14C1rhg) to be overlooked.

Lack of late-time data Perhaps one of the most important issues with this approach is the assertion that it is possible to model a SLSNe using its rise-time data alone. It was shown in Inserra et al. (2013) and Inserra et al. (2017) that SLSNe most strongly characterised by their late-time light curve. This became apparent amongst the DES sample of SLSNe upon the discovery of DES15E2mlf, the most distant spectroscopically confirmed SLSN at the point of its classification (Pan et al., 2017). The visual inspections, the search described in this section as well as the standard DES SN template fitting, have strongly suggested that the object is a SN Ia at z∼0.3. With a rapid rise and a relatively bright host galaxy, a SLSN classification appeared counter-intuitive; however, our subsequent analysis in Pan et al. (2017) showed that at high redshift we are sampling the UV regions of the SED where the evolution of SLSNe are a lot more rapid due to rapid cooling of the photosphere in the early phases. Similarly, the host galaxy was found to be consistent with a heavily star-forming galaxy, often associated with SLSNe, explaining the excess UV luminosity.

5.2 Training sample

In any ML project, the data sample used to train the classification model is its most important element. Regardless of the algorithm used, without correct and representative samples, the model will not be able to accurately label new data and often may result in overfitting. An ideal training set would be large, when compared to the number of distinct classes, containing unambiguously labelled objects, and be indistinguishable from the unlabelled test sample that we wish to classify. In reality, this is difficult to achieve and often involves manual scanning and classification of the training sample by the user (e.g., the manual scanning of point source detection in DES (Goldstein et al., 2015, and similar studies)).

In the case of SN light curves, the building of the training samples is very difficult. The data comes from a very wide range of sources as the observations are taken using different telescopes, instruments and filters. The raw numbers of classified SNe are also insufficient with only several thousand objects classified today (Alsabti & Murdin, 2017).

In this thesis, I produce an artificial sample of objects that fit all of our requirements from first principles. For each class of object, I determine the parameter space for their respective models that can be used to create a large quantity of perfect light curves in the DES photometric bands with an arbitrary cadence. I then apply the DES cadence and noise model to them, creating simulated DES-like events that closely resembles the sample of real objects.

5.2.1 DES Noise Model

The noise model applied to the data in this chapter is based on the routines implemented in the SNANA package (Kessler et al., 2009). SNANA is a powerful package designed as a tool for producing realistic light curve simulations. In previous projects, it was used to simulate the SPCC dataset (Kessler et al., 2010) as well as to generate a sample of SN Ia used to determine observational biases in the DES SN cosmology study. However, due to its complex, it is difficult to extend SNANA with new models.

In DES, SNANA forms the backbone of the SN analysis and is used to extract the image quality logs from the science and reference frames; including the zero points, PSF and sky backgrounds amongst others. Internally these logs are referred to as the SIMLIB files. I follow the same procedure as implemented in SNANA to determine the uncertainty associated with an observation, given its MJD, observing field, filter and the CCD number. The final flux is then drawn randomly from a normal distribution centred at the simulated flux, with a variance equal to the estimated uncertainty. To demonstrate the effectiveness of this approach, Figure 5.1 shows the comparison between the r-band light curve of an example SN Ia observed by DES and a simulated light curve generated based on a SALT2 model (performed using the SNCosmo package (Barbary, 2014)) fit to the original object. The S/N ratio of the observed and simulated light curves fall close to unity, demonstrating their agreement.

5.2.2 SN Ia

Amongst the various SN classes simulated as part of this thesis, SN Ia is unquestionably the most well-studied and understood class of objects. Thanks to two decades of use as cosmological probes, there exist a number of packages able to model and simulate these objects with a high accuracy. Furthermore, the parameter spaces of SN Ia as well as peculiar outliers to the class (SN Ia-91bg and SN Ia-91T) are well understood, giving us a firm base on which we can build their simulated samples.

While there are no limiting factors preventing us from performing our own simulations, starting with any implementation of the SALT2 model (e.g SNANA, SNCosmo or otherwise), and passing these through the DES noise model (Section 5.2.1), this would, in

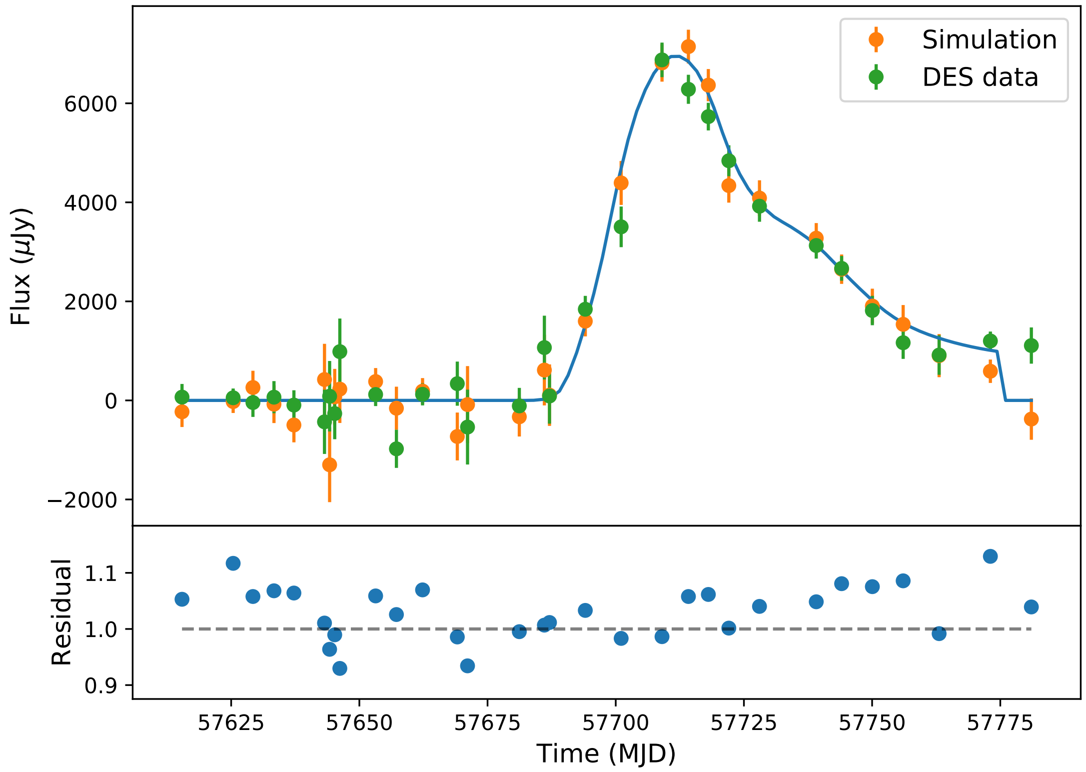

Figure 5.1: *Top*: r-band light curve of an example SN Ia observed by DES and a simulated object created to replicate the original data point. *Bottom*: the ratio of the S/N for the observed and simulated data light curves shown to be in agreement.

essence, replicate the sample of fake SN Ia injected into the science images as part of the real-time data reduction pipeline. In DES, these objects are used to estimate the image quality and generate the SIMLIB files making them equivalent to light curve that would be generated through SNANA.

The light curves of SN Ia that are injected into the images are generated using the extended SALT2 model as used in Betoule et al. (2014). The upper redshift range was set as z=1.4 ensuring that the sample is not limited by the simulated redshift. We expect that DES is able to detect SN Ia up to redshift z∼1.3. The fake SNe are injected such as to match the rate evolution measured by Perrett et al. (2012). As a downside of using a predetermined sample of simulated objects, we do not have any control over the number of objects entering it. However, 45,000 objects passing the detection criteria form a sufficiently large sample of SN Ia. Figure 5.2 shows the redshift distribution for our SN Ia training set.

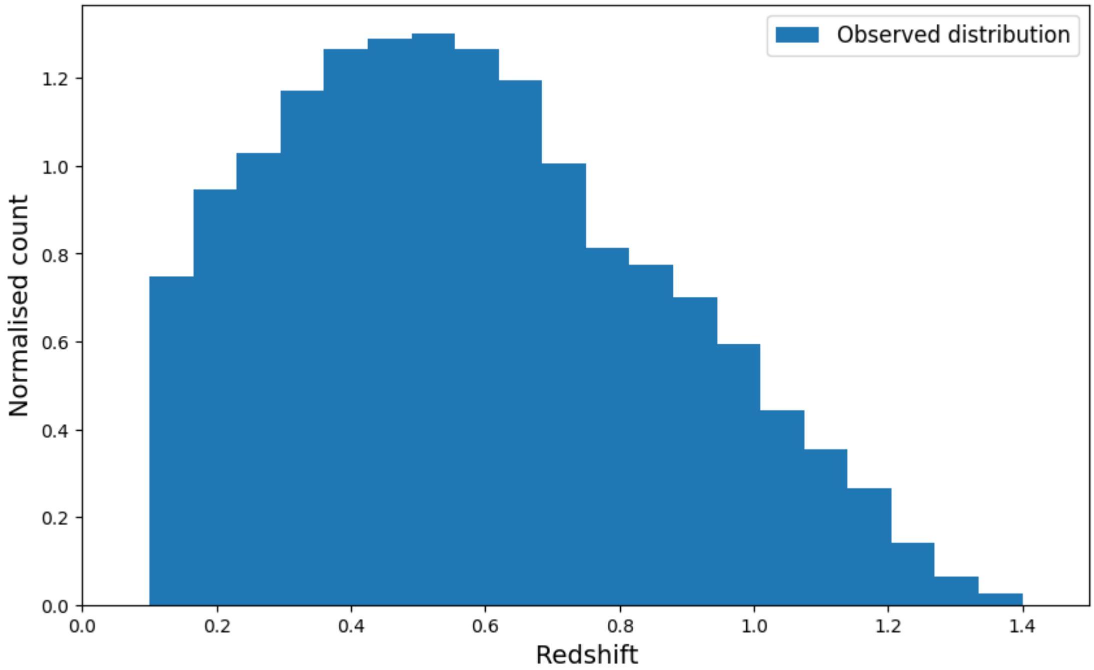

FIGURE 5.2: The redshift distribution of SN Ia that form part of our training sample.

5.2.3 Core-collapse Supernovae

In the local universe, Core-Collapse Supernovae (CCSN) are more numerous than SN Ia, with an approximate fraction of 70% CCSNe to 30% SN Ia (Alsabti & Murdin, 2017). However, CCSN are a fainter with an average brightness only a tenth of the SN Ia luminosity that results in a survey such as DES being able to only detect them up to the z∼0.6 as compared to z∼1.3 for SN Ia, giving a much lower observed rate. However, note that the training of CNNs requires that each distinct class of objects entering the classification model must be equally represented. We treat hydrogen-rich and stripped envelope CCSNe separately.

5.2.3.1 SN Ib/c

In Chapter 3, I presented CoCO, a method for creating templates as well as simulating SN Ib/c, based on the spectroscopic templates shown in Table 5.1. Due to the small number of good spectral templates, the spectral subtypes of the templates do not match their measured relative abundance and, I use the Li et al. (2011) measurement of the local rates of CCSNe to correct their abundances. The decision to follow their observed abundances is based on our lack of interest in subclassifying transients based on their similarity to a specific SN template.

Table 5.1: Sample of SN Ib/c used within CoCo as template for their class. The variation in the peak luminosity of the SNe results in different upper redshift limit at which the objects are detectable by DES. The SNe with slower evolution and greater luminosity are detected more often in the survey resulting in a higher number of accepted samples.

SN Name		
SN1993J	0.79	3322
SN1994I	0.70	975
SN1996cb	0.78	2151
SN1998bw	0.80	16416
SN2002ap	0.80	2938
SN2005bf	0.80	8259
SN2005hg	0.80	1942
SN2006aj	0.80	11988
SN2007Y	0.57	428
SN2007gr	0.67	954
SN2007uy	0.64	905
SN2008D	0.28	196
SN2008ax	0.43	766
SN2008bo	0.46	390
SN2009iz	0.80	1553
SN2009jf	0.80	4044
SN2010al	0.80	14784
SN2011bm	0.80	24213
SN2011dh	0.73	2659
SN2011ei	0.39	410
SN2012ap	0.54	707

I generate the light curves in the redshift range of $0<z<0.8$, drawn using a volume-weighted, non-uniform random distribution based on the cosmic star formation rate (Hopkins & Beacom, 2006). To introduce a level of diversity into the sample, I apply host galaxy reddening to the templates (Milky Way extinction is not necessary as DES observed very low extinction fields). I use the Cardelli et al. (1989) law with $R_{\rm v}$=3.7 (corresponding to the Milky-way value) and the E(B-V) values drawn randomly from the modulus of a Normal distribution centred at zero with a variance, μ=0.2. I also have used a similar (but unmodulated) distribution to apply an offset to the peak magnitudes of the SNe. This is further aimed at introducing a scatter into the training sample as the low number of available templates, despite being placed at different redshifts and explosion dates, could produce repeating samples of objects that could lead to overfitting.

From the simulations, we measure the detectability of each template as a function of redshift (see Table 5.1) as well as the detection frequency of the whole population as a function of redshift shown in Figure 5.3. As expected SN Ib/c are detectable only up to z$\sim$0.8, a distance significantly lower than that of SN Ia (Figure 5.2).

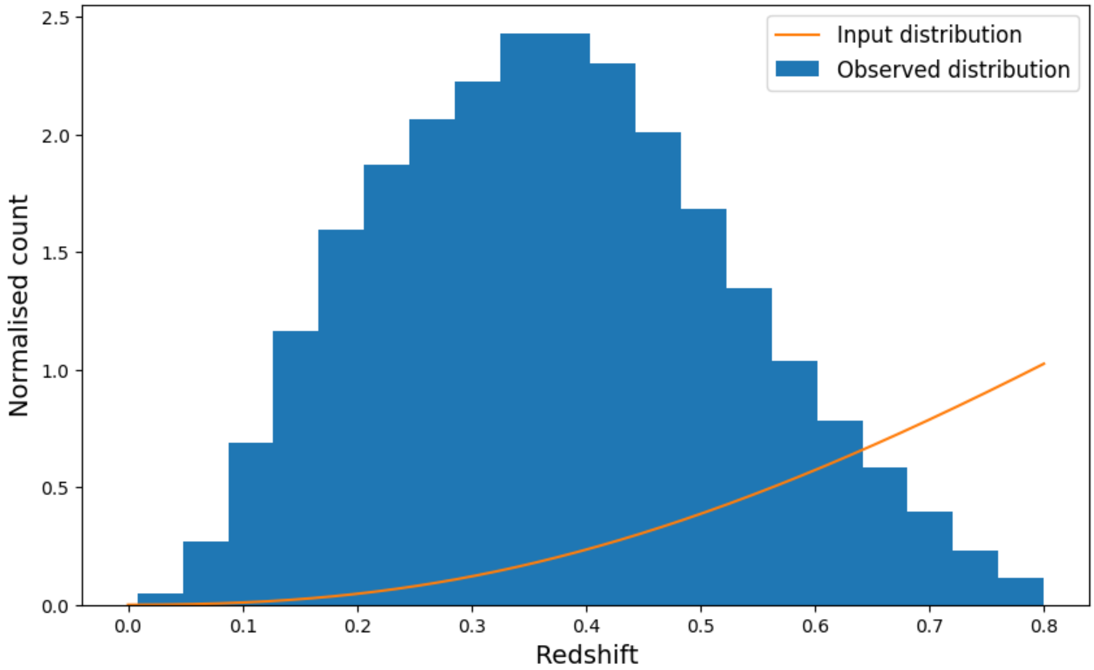

FIGURE 5.3: The input distribution of artificially generated SN Ibc vs their detection count as a function of redshift. As expected, the detection fraction of SN rises initially with the increase in the volume of the sampled universe before declining at higher redshift due to a decrease in their detectability.

5.2.3.2 Hydrogen-Rich SN

The method used for building the training sample of SN II followed that of SN Ib/c. I used the template sample, generated using the CoCo package, in Table 5.2. The only significant difference in the process of generating the sample was the simulated redshift range, which was increased to z∼0.9 as I found during our testing that using z<0.8 would result in a number of objects being detected at the upper redshift limit.

5.2.4 SLSN

The simulations of SLSNe were one of the most challenging topics of this thesis. The low numbers of known examples of this class, combined with the uncertainty surrounding their definition and the engine powering their luminosity makes their modelling a challenging task. For the purpose of a classification study such as the one presented in this thesis, we must not only replicate all previously observed objects but also make a reasonable, but not overly constraining, a prediction for what yet unknown SLSNe may appear as and represent as a class. Until recently, this would not have been possible as our understanding of the models of SLSNe and their parameters was not sufficient. However, several works including Chapters 4 & 3 of this thesis as well as Inserra et al.

TABLE 5.2: Sample of SN II used within CoCo as template for their class. This sample is smaller than its sister sample of SN Ib/c due to the lower quality of their spectroscopic data.

SN Name		
SN1999el	0.40	4052
SN2000cb	0.36	4127
SN2000eo	0.78	20895
SN2002gd	0.26	1924
SN2006V	0.45	7178
SN2007pk	0.75	18822
SN2009E	0.30	3538
SN2010al	0.90	30882
SN2011hs	0.26	792
SN2012ec	0.36	5176
SN2013ej	0.36	4114

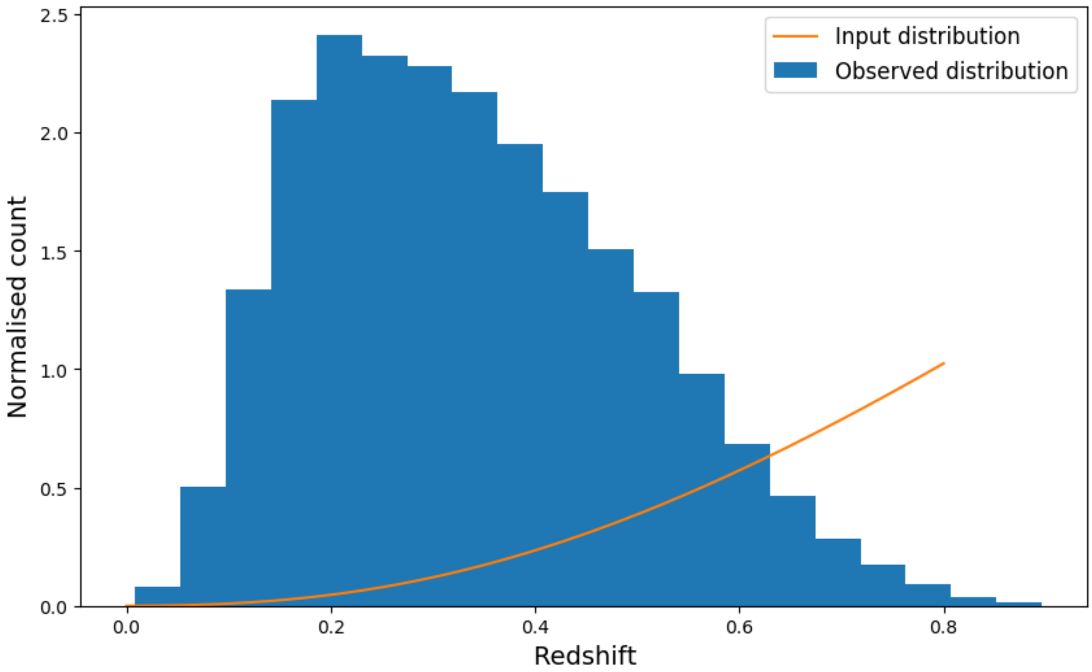

FIGURE 5.4: The input distribution of artificially generated SN II vs their detection count as a function of redshift. The distribution is skewed due to the bimodality in the detectability of the training sample shown in Table 5.2 thanks to a small number of objects with a much higher intrinsic luminosity than the rest of the sample.

Table 5.3: Definition of borders in the parameter space of 4OPS defining SLSNe in this thesis. The line represents the enter of the defining region which is constrained by within the 3σ confidence region parallel to the line.

x-Axis	y-Axis	Intercept	Gradient	1σ
ΔM(400)$_{30}$	M(400)$_0$	-21.62	0.75	0.62
ΔM(400)$_{30}$	M(400)$_0$ - M(520)$_0$	-21.02	1.14	0.59
M(400)$_{30}$ - M(520)$_{30}$	M(400)$_0$	-0.3	0.16	0.14
M(400)$_{30}$ - M(520)$_{30}$	M(400)$_0$ - M(520)$_0$	-0.22	0.35	0.08

(2013); Nicholl et al. (2013, 2017) and Angus et al. (in prep) showed that the spin-down of a Magnetar model is able to provide a good approximation for all SLSNe with an acceptable level of accuracy.

The greatest step towards simulating SLSNe was achieved in Inserra et al. (2017) where we established a new definition of this class that is versatile and robust enough to produce a sample that matches all observed objects but at the same time is limited in the span such that it does not overlap with other classes of SNe. This definition is based on Four Observables Parameter Space (4OPS), defined in narrow (800Å and 1000Å wide respectively) box filters centred at 4000Å and 5200Å, by: the peak in the 4000Å band light curves, colour between the band at peak and +30 days post maximum, and the drop in magnitude between the peak and +30 days in the 4000Å band. Inserra et al. (2017) finds that SLSNe form linear correlations in this parameter space, with a narrow scatter shown in Figure 5.5. I use this property to determine the magnetar model parameters which correspond to the definition of SLSNe.

I simulate a large number of SLSNe using the magnetar model and compare them to the 4OPS definition. The magnetar model parameters are drawn randomly from a uniform top-hat distribution, bound at $10 < \tau_M < 150$, $0.1 <$ B$_{14}$ < 20.0, $0.01 <$ P$_{ms}$ < 10.0. These limits were informed by the definition of SLSNe used in the rate calculation described in Chapter 4, but were expanded to ensure completeness and, at the same time, limit the number of computationally expensive simulations that needed to be performed. Furthermore, I introduce a modification to the 4OPS definition of SLSNe, similar to that in Angus et al. (in prep), where the parameter spaces are expanded by one magnitude of scattering while retaining the original slope of their relationship. This was aimed at including fainter objects such as those found in the DES spectroscopically confirmed sample (Section 2.2.5), that were not available at the time the relationship was constructed. The modified limits are presented in Table 5.3 and can be seen in Figure 5.5 along with the regions where objects drawn from the magnetar model.

In Figure 5.6, I show the distribution of magnetar model parameters that produce objects that match the 4OPS definition of SLSNe. Perhaps the most interesting result is the luminosity function that results from uniformly drawing objects from the magnetar

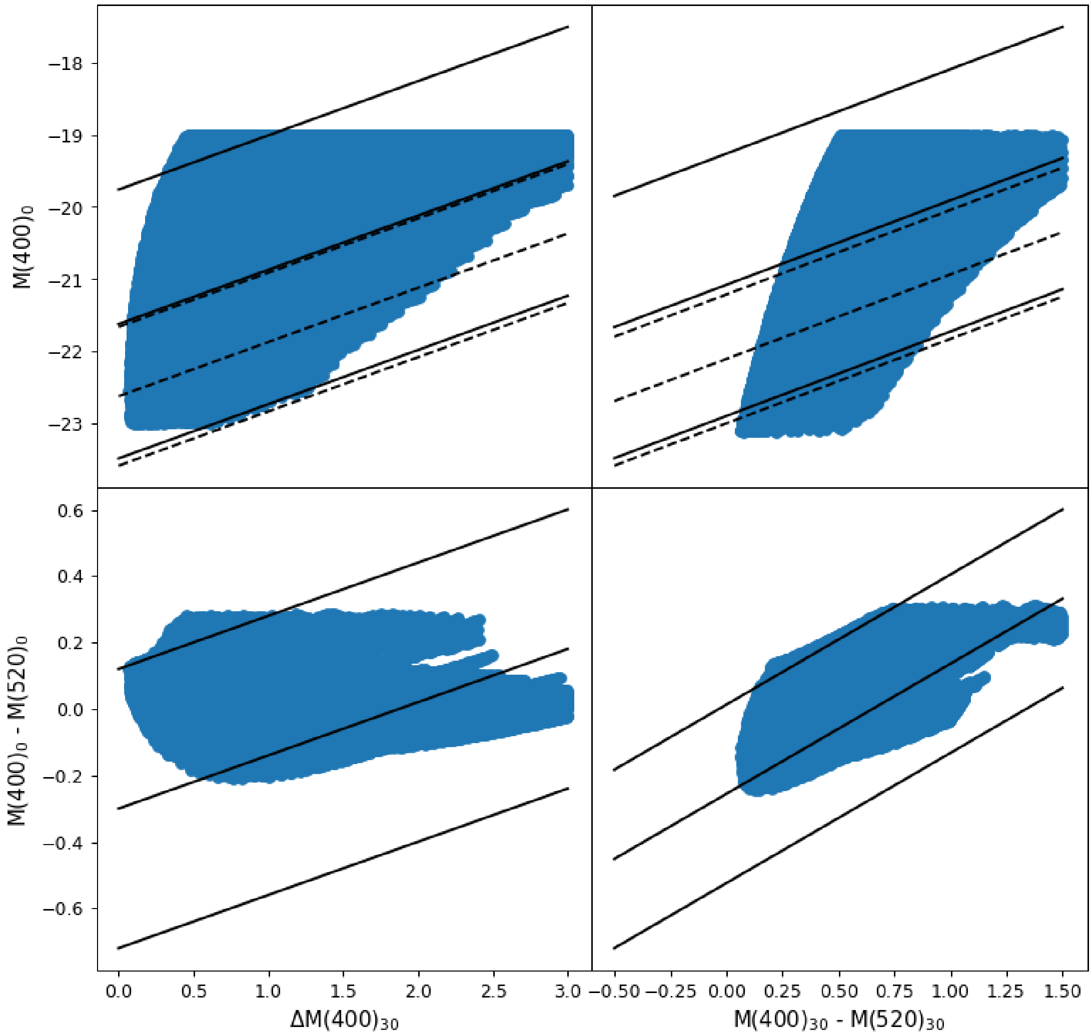

FIGURE 5.5: The 4OPS parameter space used to identify SLSNe. The solid lines represent the regions used in this work while the dashed lines are the original values found Inserra et al. (2017). The shaded area corresponds to the regions where SLSNe, generated using the PYMAGNETAR pipeline, that are compatible with the 4OPS definition.

model parameter space, shown in Figure 5.7. With no external inputs, the function matches that observed by De Cia et al. (2017c) in the PTF sample of SLSNe, showing a rapid increase in the number of fainter objects. I use the sets of magnetar model parameters that match the SLSN definition to generate their training sample. In total, ∼100,000 SLSN were generated at a range of redshifts with 0<z<3, drawn from a volume-weighted distribution following the SFR of the universe (Hopkins & Beacom, 2006) similarly to that used for simulating CCSNe (Figure 5.8).

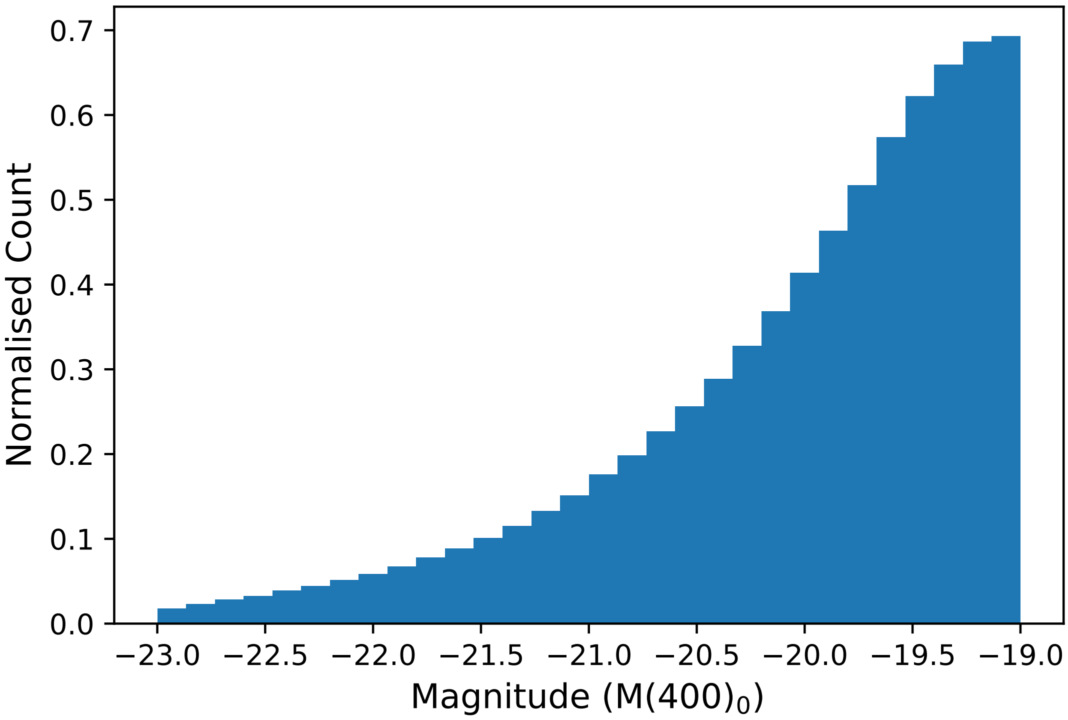

FIGURE 5.6: Distribution of peak magnitudes for SLSN generated using PYMAGNETAR. The parameters used to generate the light curves have been drawn uniformly from the magnetar model parameters space and were first compared to the 4OPS selection criteria before being used.

5.2.5 AGN

Active Galactic Nuclei (AGN) are the largest contaminant in the DES transient sample. This is partially due to their physical morphology and, in greater measure, the design of the survey. AGNs are most commonly associated with long, quasi-periodic, variable light curves that are often easy to identify based on their historical variability. As no long-term observations, matching its depth, are available for the DES SN fields making each first AGN detection its discovery. Prior to the first season of DES, a set of science verification images were taken as templates for the image subtraction pipeline used to detect new transients. AGNs that have undergone rebrightening in the first season were detected as potential supernova candidates. If the templates remained unchanged for the duration of the survey we would see a decrease in the contamination each season. Furthermore, we would be able to remove most of these transients retrospectively by selecting objects with detections in multiple seasons. The survey did, however, change the templates each year in the first three seasons of its operations to increase the quality of the images used as templates. In the final two seasons, the data from Y2 was used as templates. Additionally, the data for the first season was also later reanalysed using Y2 images as a template. A caveat of DES that caused us particular issues is that negative

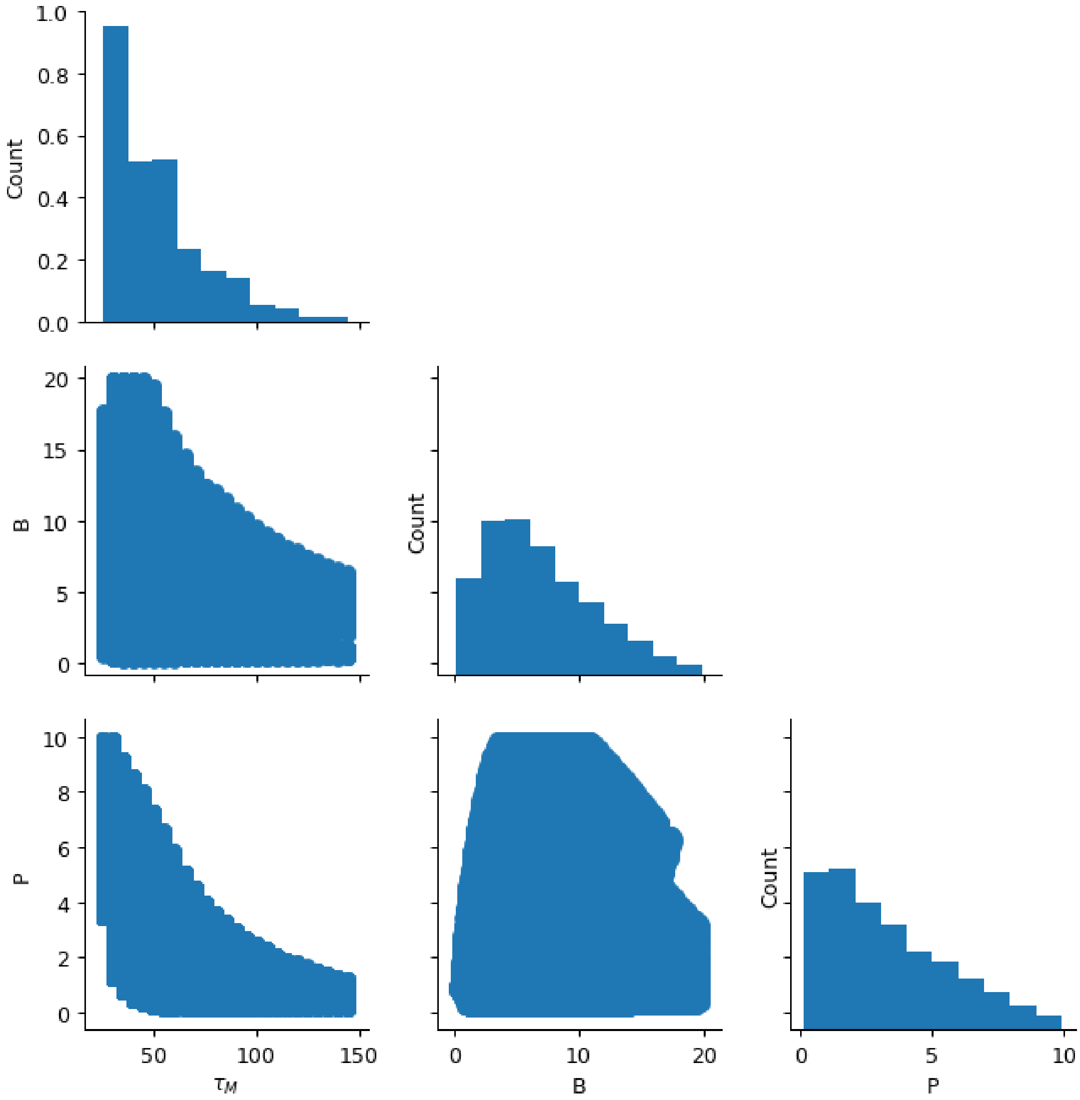

Figure 5.7: Distribution of magnitudes model parameters that result in a SLSN-like event that matches their 4OPS definition (Inserra et al., 2017).

'detections' are not considered as detections within the transient selection algorithms. As a result, each DES season contains a large number of objects which are selected as new transients despite showing strong visual signs of prior, albeit 'negative', variability.

In the cases of SLSNe, this is particularly troubling as their slow evolution can be sometimes confused with an AGN with a quasi-period of approximately one year if only single DES seasons are considered. It is, therefore, imperative that AGNs are correctly represented in the ML training sample used in Section 5.4.1. For this purpose, I use the existing simulations of AGNs, in the DES observing bands, presented in Hönig et al. (2017). While these simulations were originally aimed at evaluating the possibility of using AGNs as cosmological probes, using a technique referred to as Reverberation Mapping, they were suited perfectly for this project. The simulated light curves did

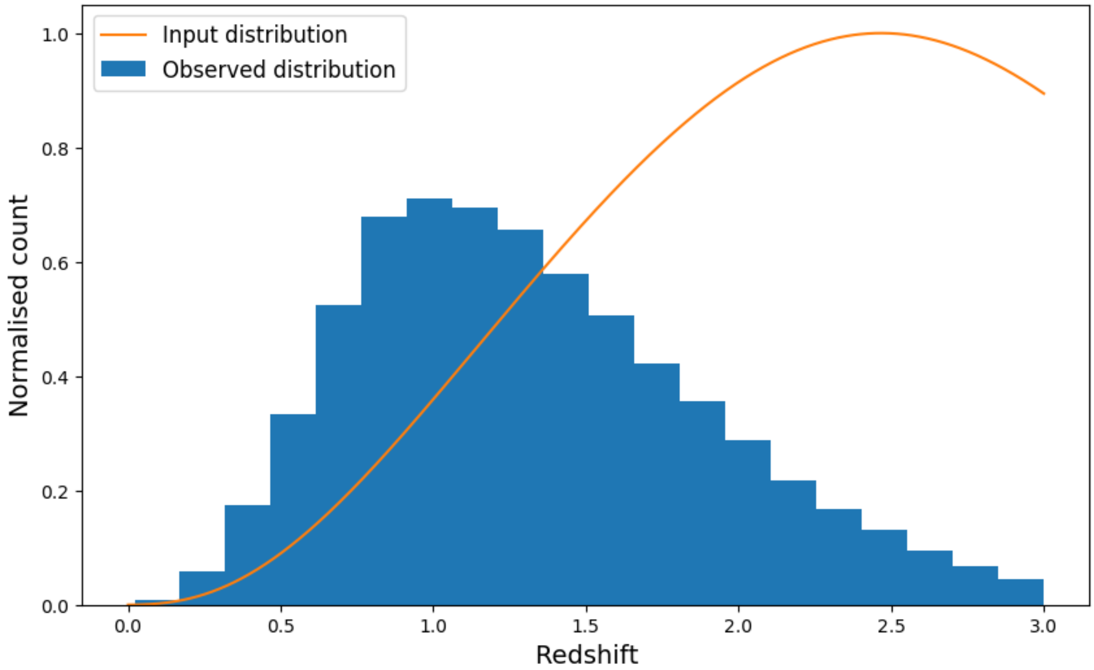

FIGURE 5.8: The input distribution of artificially generated SLSN vs their detection count as a function of redshift. The superior luminosity of these objects compared to other CCSNe is apparent when comparing their detectability ranges. This also motivates further our search as we know that DES should be able to detect SLSN up to z$\sim$3, while the most distant object to date was confirmed at z=2.0

not include any survey noise, were densely sampled (one-day cadence) and had a span exceeding four years. In total 100,000 simulated objects were available for this study including those placed at redshifts outside the detectable range for DES. I have therefore placed each object at random start dates and fields, before applying the survey noise using the method described in Section 5.2.1, resulting in ~60,000 detected AGNs.

5.2.6 Noise

Visual inspection of the DES light curve data shows that a limited number of objects, originally recognised as a real transient according to the DES transient selection criteria (Chapter 2), do not appear to be physical in origin. There appear to be two main origins for these objects: bad image subtractions and spurious noise detections. Despite a sophisticated, ML powered, transient selection pipeline (Goldstein et al., 2015), some objects (often elongated and with negative subtractions; Figure 5.9) can pass the ML cuts, albeit with a low score. In some cases, likely dependant on the observing conditions, this may occur in several epochs separated by less than 30 days, giving the object a 'real transient' flag.

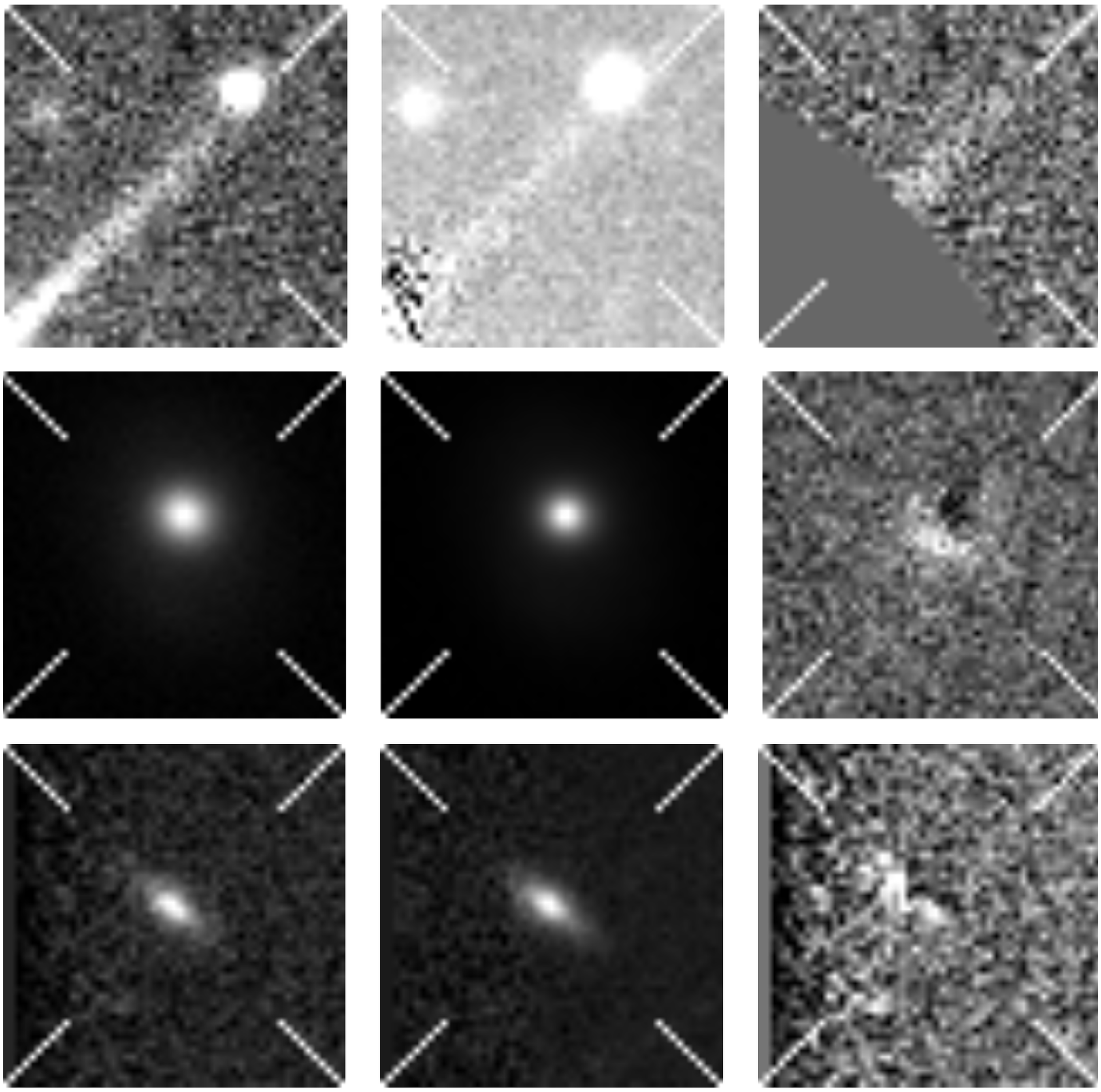

Figure 5.9: Examples of bad subtractions of DES images. *Left* shows the science images, *center* represent the image subtractions templates and on the *right* are the subtracted images showing defects.

Another channel that can result in the misclassifications of candidates is the detection of slow-moving, near earth object. Such objects are most commonly detected at the same position only in two or three consecutive bands. In subsequent epochs, they are, in normal circumstances, no longer detected at the same position resulting in the object being rejected. However, in some rare cases, bad subtractions or random noise spikes exceeding the 5 sigma detection limit, within 30 days cut can result in a 'real transient' flag.

To model these objects, I use a very simple approach of inserting a number of sharp, δ-function like spikes in the data that correlate between the filters and are separated by less than 30 days to account for the misidentifications. The spikes are selected between 19<mag<22 in order to test the different behaviours of the GP interpolations used in the next step of this analysis (Section 5.3). The absolute value of the peak does not play an important role in the classification process as the data is normalised before entering the CNN. Similarly to other classes of transients, ∼100,000 objects have been simulated across all fields.

5.2.7 Missing classes

While in this thesis, I have created one of the most thorough training samples of SNe for the purpose of a ML classification study, it still cannot be said to be complete. There are a number of classes of known transient objects which I was unable to account for in this work. Some objects such as kilonovae, associated with gravitational waves as their optical counterparts, evolve too rapidly to be using the cadence of DES. Omitting these (undetectable) events does not bring any difference to the final result of our classification. However, one class of objects which could have an effect on our final classification are the newly discovered class of rapidly evolving SNe Drout et al. (2014); Rest et al. (2018). Recent work by Pursiainen et al. (2018) showed that these objects are relatively common within DES with 72 detections in the first four seasons of its operations. While there are now early, tentative signs (Pursiainen et al., 2018) that these objects are powered by a SN shock interacting within a thick an extended wind (Piro, 2015), similar to the model used in modelling of the 'bumps' found in SLSNe Section 3.1.3.2. It is this particular connection that would be interesting to explore, however, the modelling of these objects is still in its infancy. The model parameter spaces defining them, their SED models and other similar aspects developed for SLSNe over the last several years have not yet been studied for these fast-evolving SNe.

The omission of rapidly evolving SNe from our sample will result in these objects being mislabelled in our classifications. It would, however, be unlikely that any of the objects that we have not included in the training sample would get mislabelled as a SLSNe due to their significantly faster evolution. I test this assertion in Chapter 5 using the ground-truth sample of objects identified by Pursiainen et al. (2018).

5.3 Data Augmentation

Before the training sample of SNe created in Section 5.2 can be used to build a CNN classification model, it has to first undergo a number of augmentation steps. The data passed through the CNN must be uniform in terms of the number of data points as well as their separation, regardless of the field and season the data originated from. To achieve this, I must first select a suitable length of observations and cadence that overlaps the most closely with that observed by DES. Furthermore, I apply a flux correction required to normalise the effect of using a varying subtraction template in a different season. Finally, I use GPR to interpolate and augment the data such as to meet the requirements of CNN.

5.3.1 Choosing the observing block

I define the observing block, for the use in our classification study, as the span of time (measured in days) that is the longest period over which all DES seasons observe all of its fields. Due to the observing conditions and scheduling, the DES observing periods vary between the seasons and fields. The difference between the longest and shortest observing window in DES measures 40 days.

Selecting the observing block is more complex than simply selecting the length of the shortest season. Figures 5.10-5.13 show the cadence of DES in Y1-4 in all fields and bands. Instead, this is done in two stages: first I find the span that covers all the filters: from the first point where all the filters are observed, to the last point where all the filters are observed. I then remove the points at the beginning of the season in cases where the gap in the data is longer than 10 days. This is a common consequence of observations being missed due to the atmospheric conditions. Data does not have to be similarly removed at later stages of the light curve as the GPR interpolation can account for large gaps as long as they are supported by a number of points either side of the intermission.

From these measurements, I determine the optimal observing block to be 149 days in duration. The span covered by the block in each season and filter is shown in Figures 5.10-5.13. Due to the improved quality of the light curves in the second part of each season, I place the observing block as late in time as possible.

5.3.2 Choosing the cadence

Upon deciding the length of the observing block used in the simulations, the next step is to choose the cadence of the interpolated observations. As GPRs are used to augment the data, essentially any cadence can be used. As there are no rules or precedencies set out in the literature that discuss the optimum treatment of the augmented data, I must make an informed decision. The factors which balance the decision is on one side to represent the data without the loss of any information observed by the survey, while at the same time not introducing too many points which, essentially, duplicate the information.

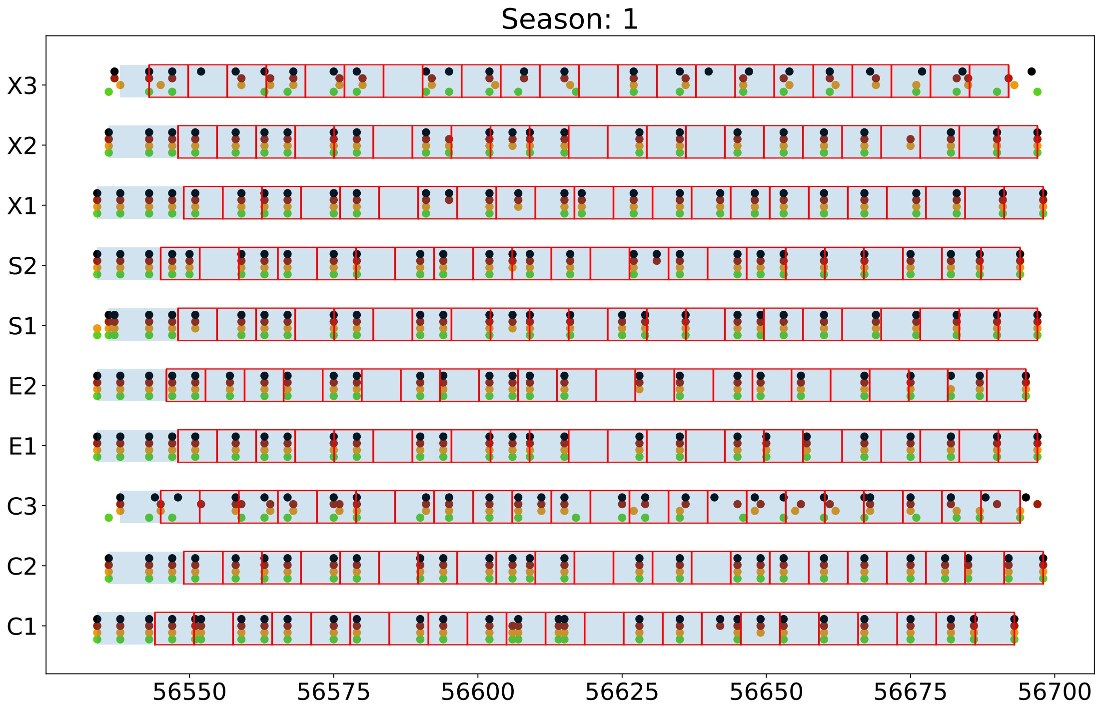

Figure 5.10: The cadence and observing block of the first season of DES

The observed cadence of DES is not uniform and varies through the season due to the observing conditions. Early in the season, the cadence is shorter as the observing weather conditions don't allow for the observations of the wide DES fields leading to a shorter DES cadence as the deep and shallow fields are given more observing time. On the opposing end, the cadence stabilised as the season progresses and settles at the designed 7 days. This is seen in Figure 5.14 resulting in a bimodal distribution with an average cadence of 5 days. With a lack of any other factors, I use this value as the base for the cadence used in Section 5.3.4.

5.3.3 Applying Flux correction to Real Data

Before the GPR can be applied to the data, a final correction is the effect of DES exchanging the image subtraction template between seasons. As the focus of the DES SN team is predominantly the study of SN Ia, the decision was made to maximise the quality of single-season light curves. As the image quality improved throughout the initial two seasons of observations, the templates have been updated each year. While optimal for the study of short transients, where only a single season is of interest, for slowly evolving SNe (and AGNs) this causes an issue where the supernova light curve is present in the template resulting in decreased flux in the subsequent season. This is a particular problem for SLSN, where their evolution can often be slow enough to be

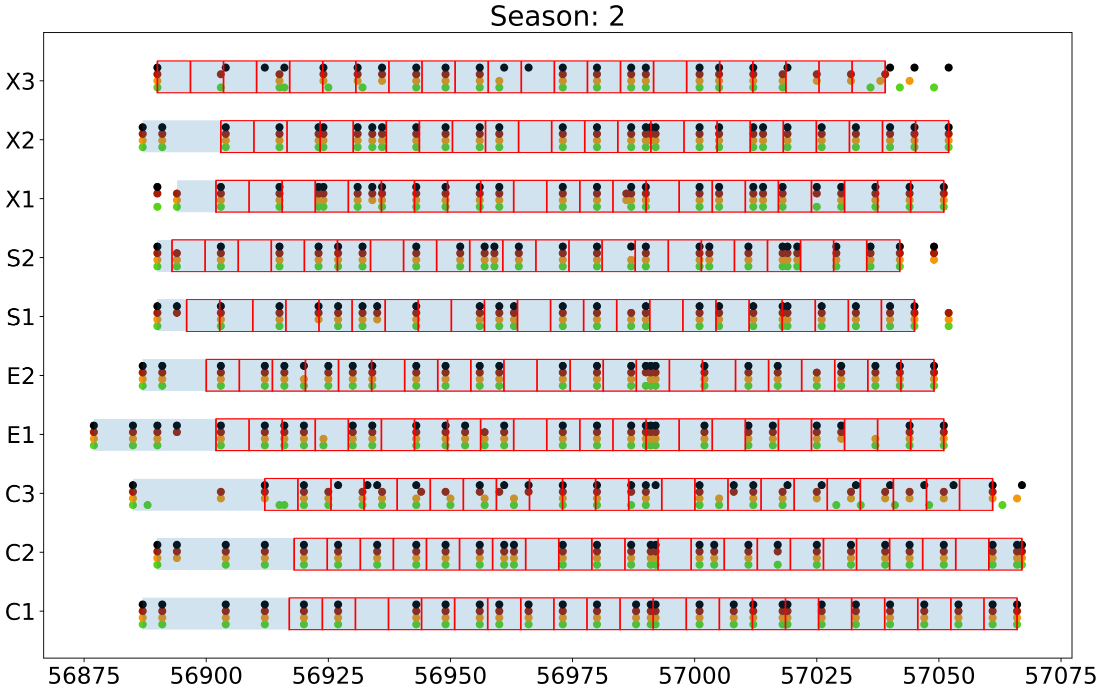

FIGURE 5.11: The cadence and observing block of the second season of DES

detectable in multiple seasons in DES (Angus et al.; in prep). This could potentially be a factor leading to the misclassification of SLSNe and hence cannot be ignored.

While the optimal approach to this would be to perform the image subtraction and source detection with a single template, this would be computationally prohibitive due to the scale and complexity of the raw DES data. As an alternative, I used the DES analysis logs to determine the observations that have been used in the creation of the template images. In these frames, I measure the median flux of the object and use this value to correct the offset. As a simple test for this approach, I use a light curve of a SN Ia that exploded early in the second season of DES. In the uncorrected DES light curves, this results in a flat but negative light curve in the third season.

5.3.4 Applying GPs

The size and extent of the training sample used in this thesis are one of the two advancements made towards classifying SNe in DES using the ML approach. An equally important step, crucial for the use of CNNs, was the use of GPR (Section 3.3) as a tool for light curve interpolation and augmentation. CNN performs pattern recognition using a set of convolutional kernels with a fixed size, therefore requiring the data to be evenly sampled. This has tremendous benefits as it does not require any feature extraction steps and uses every data point in the classification process. While the observed data cannot be used directly with this technique due to its non-uniform sampling, using a

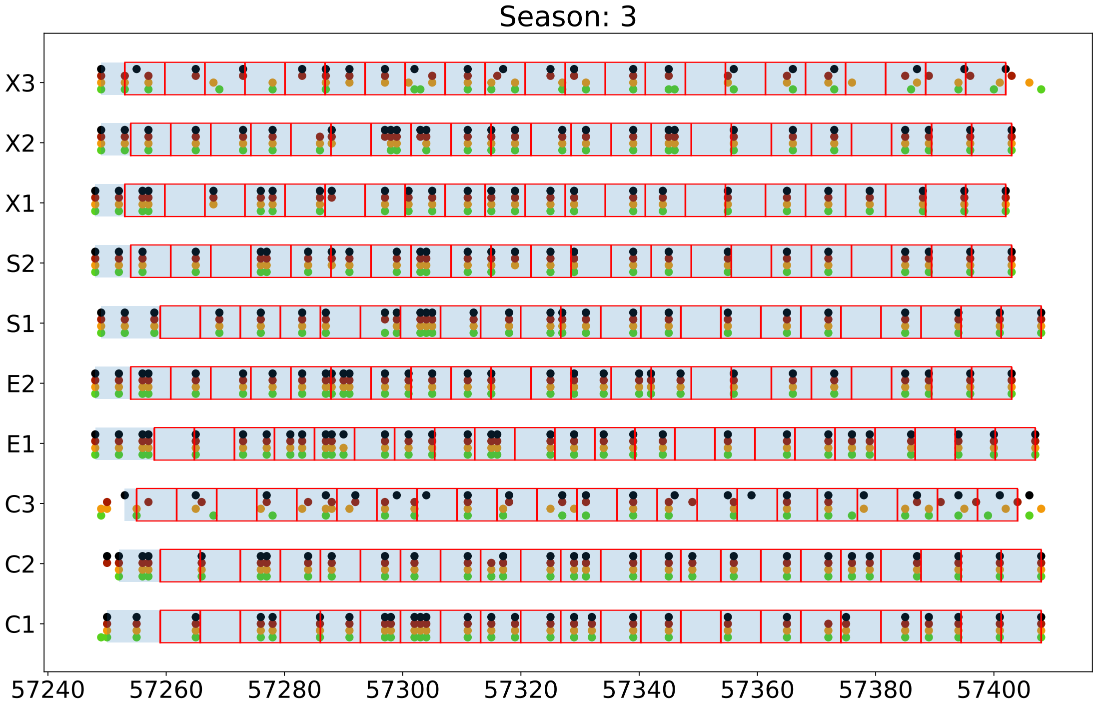

Figure 5.12: The cadence and observing block of the third season of DES

GP interpolated light curves removes less information about the data than a parametric model. Simultaneously, it does not introduce any correlations between the distinct bands, both in terms of the flux and the onset of the SN.

I apply the method described in Section 3.3 to interpolate the light curves using the Matern 3/2 covariance functions. I perform the interpolation over the period selected in Section 5.3.1 using the base cadence found in Section 5.3.2. After testing the CNN in Section 5.4.1, I found that using a cadence which doubles the original 5 days, to 2.5 days, improves the accuracy of the model. The motivation behind the doubling of the cadence was to allow a gradient for each point to be calculated closer to the point itself as opposed to between the points. The extra points act as control points in this scenario.

5.4 Classifications

In this section, I bring together all blocks built in this thesis required in order to perform a photometric classification of DES transients. I feed the sample of artificially generated transients, augmented and matched to the DES cadence and observing conditions, into supervised ML algorithm, building a model for the classifications. I then apply it in two steps; first, I separate SNe from other transients and then attempt to classify them based on their subtypes.

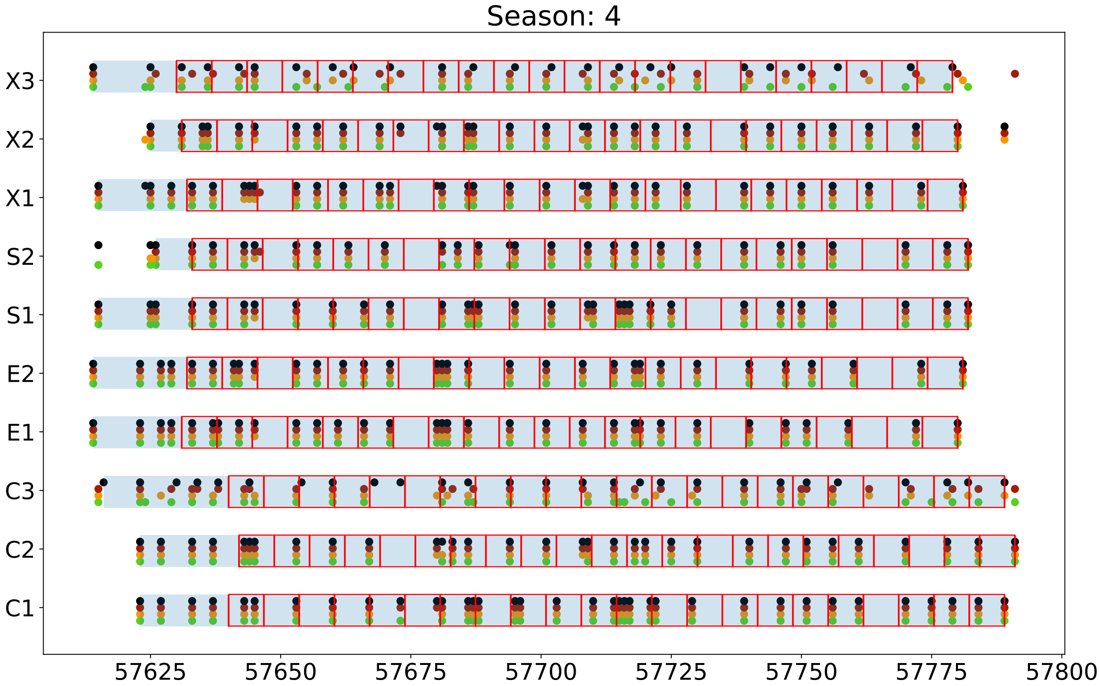

FIGURE 5.13: The cadence and observing block of the fourth season of DES

The construction of the artificial DES training sample of transients was a major step towards performing their comprehensive classification study using the ML approach. In recent years, the use of ML expanded far beyond the purely academic uses within the field of Computer Science. The world around us is currently being shaped by Artificial Intelligence (AI) augmented technologies, driven in large measure by Artificial Neural Networks (ANN) and their derivatives such as Convolutional Neural Networks (CNN) and Deep Learning.

The process of selecting transients for spectroscopic follow-up is an example, albeit not explicit, of SN photometric classification. This task has been performed manually, via the visual inspection of the light curves, for decades in every SN survey. In recent years a number of attempts have been made to devise a pipeline for photometric classification of SN based on the clustering of light curve model parameters. However, this problem can be approached from a more fundamental point of view using AI. Computer vision, a prominent branch of AI, has been successfully applied to countless examples of classification tasks where humans demonstrated a superiority over the early classification methods. Projects such as ImageNet (Russakovsky et al., 2015) were able to produce models capable of identifying a number of everyday entities (humans, vehicles, animals, household items) with an accuracy exceeding that of an average human. While the scarcity of the training samples available to us in comparison to projects such as ImageNet does not allow us to use an equally complex model, this is not required as

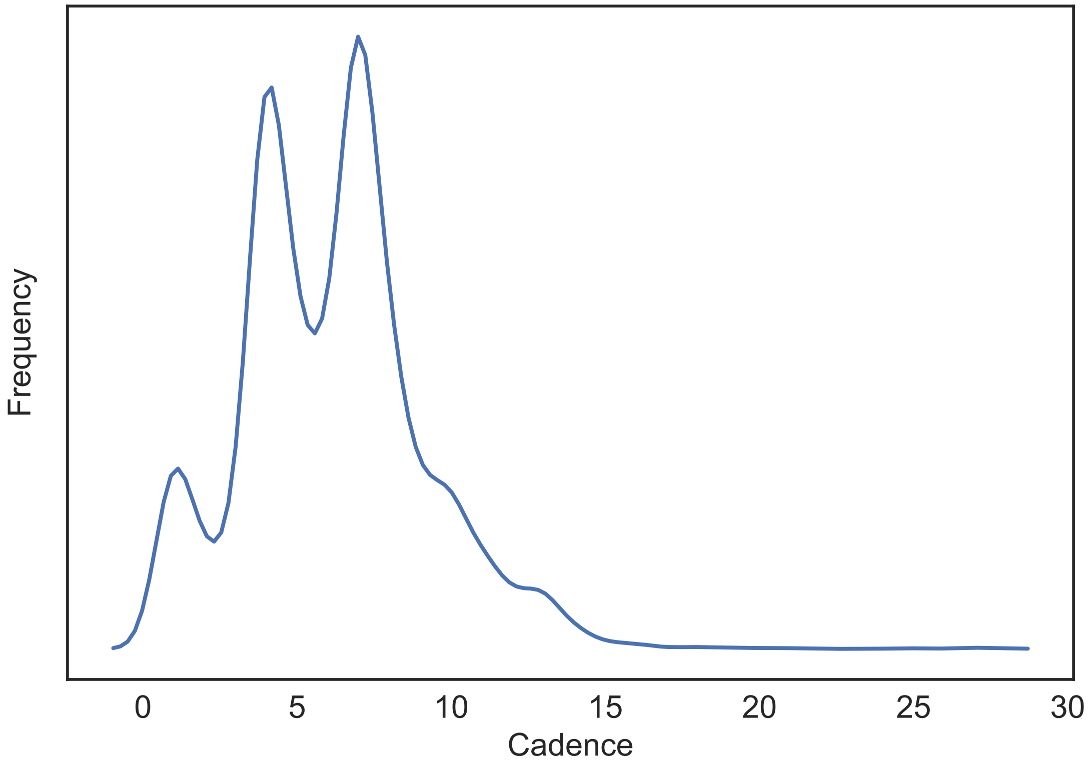

FIGURE 5.14: Kernel Density Estimate (KDE) plot showing the cadence of DES across all seasons, field and bands. The bi-modality of the distribution can be attributed to the balance between the designed DES cadence of 7 days, occurring only in the perfect conditions, and the actual cadence of 3 days observed in the early parts of each season.

the complexity and diversity of our transient data is not as high as that of an everyday object.

In this section, I describe the use of Convolutional Neural Networks (CNN) as an AI tool used to first identify SN light curves in the DES data and subsequently classify them into their respective subclasses with the overall aim of producing a photometric sample of DES SLSNe.

5.4.1 Convolutional Neural Networks

CNNs are currently one of the hottest topics in the world of AI and ML. While their widespread use is novel and a result of the increase in the performance of computer devices, the theory behind them dates back to the early work on Artificial Neural Networks (ANN; McCulloch & Pitts, 1943) and replicating the human ability to learn from an external stimulus.

5.4.1.1 Artificial Neural Networks

All principal components of an ANN are fundamentally based on the human brain contain neurons, represented by nodes and activation functions. The nodes, usually arranged in a network of layers, are connected by a set of weight that corresponds to the biological synapsis. The aim of an ANN is to perform a non-linear transformation between the input parameters and the output values.

ANN is formed through a network of fully interconnected layers, containing activations functions that, in essence, calculates the weighted sum of the inputs and creates an output that acts as an input for the next layer. The choice of activation functions is extremely important to the performance of an ANN. The most commonly used form; the sigmoid function produces an output near to one for inputs that are accepted and zero for the rejected values. The Rectified Linear Unit (ReLU), another commonly used activation function, acts in a similar way but produces a linear output that tends towards infinity above a certain activation value.

The choice of the number of layers is dictated by the complexity of the problem tackled by the network. Between the input and output layers lays a number of hidden layers. While the input later must match in size the dimensions of the input dataset and the dimensions of the output must match the number of individual classes present in the training set, the hidden layers can have an arbitrary shape. The process through which the networks calculate the weights is referred to as Backpropagation which performs a form of a stochastic gradient descent to optimise the loss (or residual) function. There is numerous implementation of the loss functions and backpropagation algorithms, however, in this work, I chose to use the defaults found in the TensorFlow package: ‘cross-entropy’ and ‘Adam’ respectively.

5.4.1.2 Convolutional Neural Networks

Convolutional Neural Networks (CNN) is a type of Deep ANNs where at least one layer is a convolutional layer. These layers are designed to work similarly to edge and shape enhancing features found in popular image processing software, but instead of relying on predetermined forms learn to best match the structure of the objects found in the training sample. An important feature of CNNs is additional Pooling layers which extract the enhance information from the convolved data through a process of dimensionality reduction. The most commonly used Max Pooling layer works by passing a sliding window, of length n, over the data convolved with the filters, with length m, and selecting the highest valued pixel to create new output data with length $n - m + 1$

5.4.2 SNe vs AGN vs Noise

While CNNs are extremely powerful in their ability to classify images, regardless of what they contain, they often rely on huge training samples in order to learn their discriminating features. In the case of DES transient data, we are still not operating on a sufficiently large dataset despite the work on enhancing the sample. However, it is possible to simplify the classification problem to reduce the number of training samples required to produce a good classification score.

5.4.2.1 Choosing the training sample

As the first step in the analysis of the DES sample, I separate the task of classifying SN from that of identifying real SN transients amongst the background of spurious detections and AGNs also detected by the survey. As the training sample for each class must be of similar shapes, I use all of the $\sim$ 60000 fake AGN generated in Section 5.2.5 as well as a random sample of 60,000 spurious noise examples. The matching SN sample must contain examples of all SN in approximately equal proportions. I therefore use 20,000 SN Ia, 10,000 SN Ibc, 10,000 SN II and 20,000 SLSN all drawn randomly from their respective simulated samples (Section 5.3).

5.4.2.2 Reshaping the data

Due to their complexity, CNNs rely heavily on fine-tuned optimisers for minimising the model's loss functions. As a result, the data must satisfy a number of strict criteria in order to comply with these constraints. While most of them, such as the need for the data to be linear, is naturally satisfied by the training dataset, we must observe a number of the constraints, including the upper and lower limits on the flux which must be in the range of positive and negative unity.

As the final piece of book-keeping, the data for all training samples must be concatenated into a single, multi-dimensional matrix, shaped such as to separate the features which are dimensionally independent of each order. In order to allow for the models described in the following section to extract both the colour and morphological evolution of the transients, each season of data is represented by a 4×46, two-dimensional vector, corresponding to the number of photometric bands and epoch per band respectively. This central block of data is built for each season independently, as the large gap between the observing blocks means that the data cannot be treated as continuous.

5.4.2.3 Designing the network

The design of a neural network is driven through a process of trial and error as there are no clear formalisms available as a guideline for the process. While some early work is being undertaken at Google in the area of automating the design of the networks for maximum performance, this is a very computationally expensive task and therefore prohibitive for us. In the case of this thesis, I am instead relying on my domain knowledge of the distinguishable features of transients to optimise the performance of the learning process.

The CNNs presented in this chapter underwent many iterations with a wide spread of layers of complexity. In all instances, the first point of access in the model is a convolutional layer containing 30-80 independent filters each between 3-9 epochs wide. These filters are applied to every season and band independently. A max pooling layer is applied to the data at this point as a way of emphasising the features highlighted by the convolutional filters before a second convolutional layer, orthogonal to the first layer, is applied to the data in order to measure the colour at each epoch. At this stage, an average pooling layer is used again extracting the two most prominent features in the colour space for each filter.

After comparing a large number of iterations of these hyperparameters, I found that using 50 filters spanning 5 epochs in the first layer and 30 filters in the second layer produced the highest accuracy model. Perhaps counterintuitively, iterations, where I combined these filters together into a single two-dimensional filter, did not provide higher accuracy. A low number of orthogonal filters provides a freedom for the features to be learned independently and prevent them from relearning the same features. One could imagine a situation where a similar light curve shape may be associated with a different colour evolution for a different class of transients. This highlights the importance of allowing the CNN to build its own features out of the simplest building blocks without overcomplicating the design by constraining the model.

5.4.2.4 Training the model

The combined training sample build in Section 5.4.2.1 is passed through the network using a batch size of 5000 objects with 100 epochs, or individual runs of the backpropagation algorithm. CNNs are often trained on smaller batches of data to accelerate the learning process and help to prevent overfitting. As a general rule of thumb for the choice of the number of the fitting epoch, the fitting is stopped when the model approaches convergence as an excessive number of epochs would allow the model to ‘learn’ the test sample leading to overfitting.

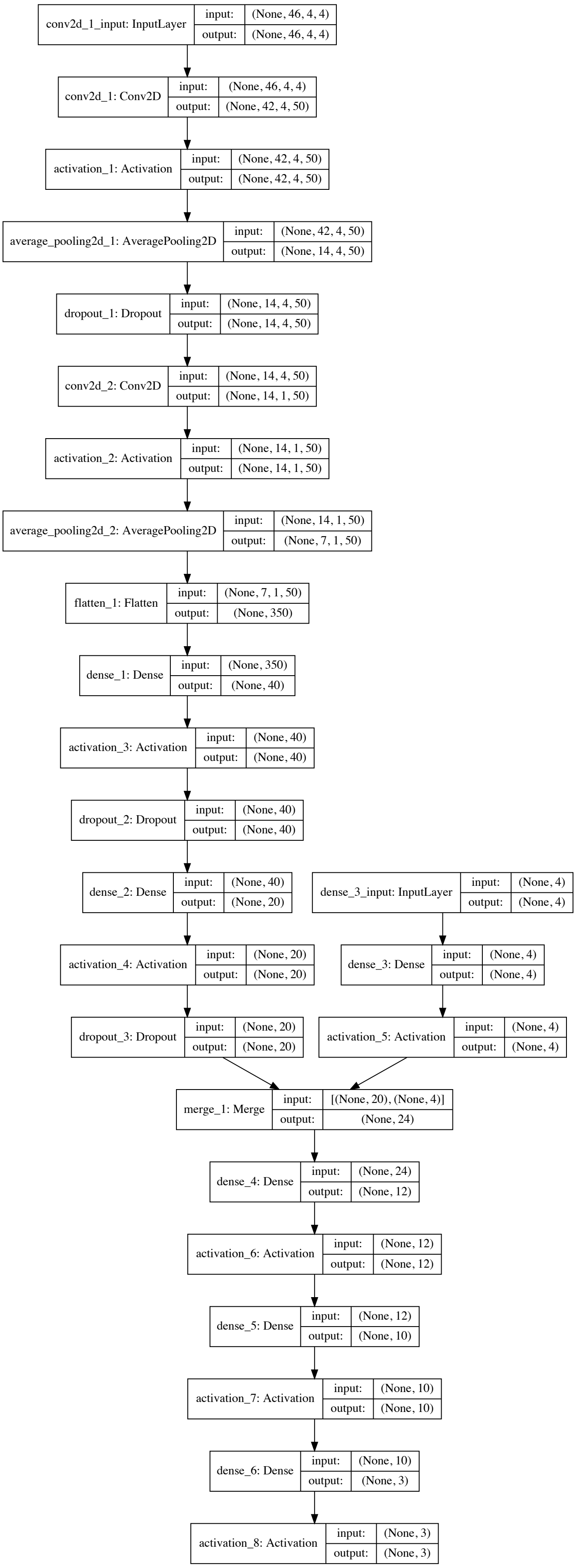

FIGURE 5.15: The CNN used for classification of SN vs AGN vs Noise. Each layer is labelled with its function within the network as well as its input and output dimensions.

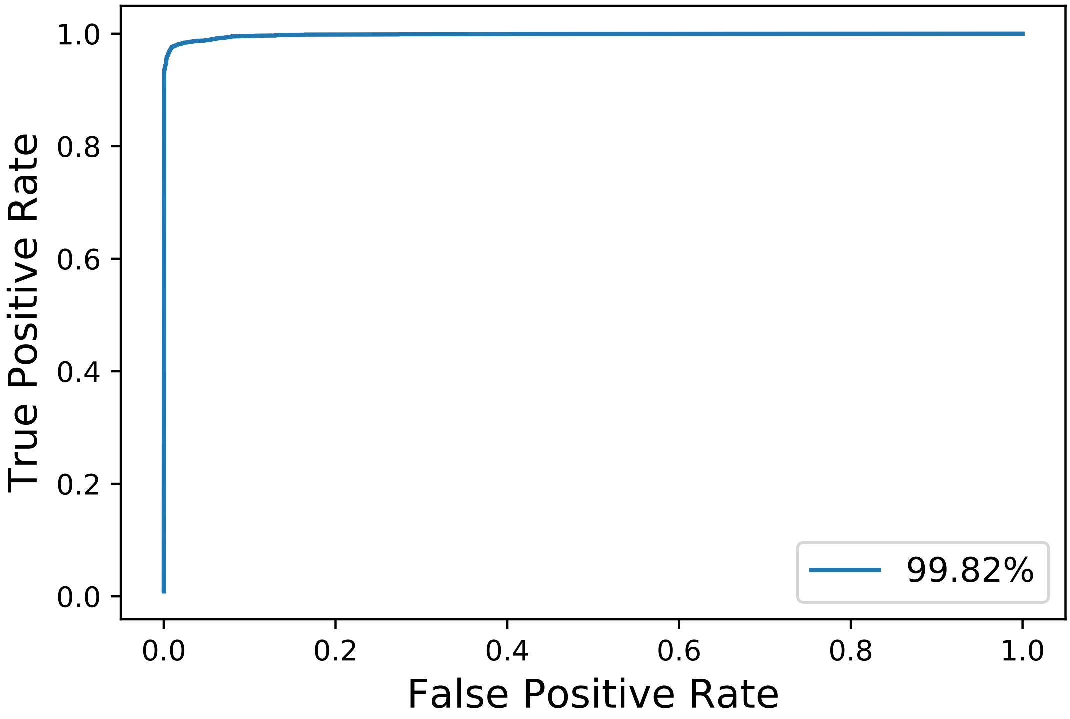

FIGURE 5.16: ROC curve and the AUC showing the accuracy, reflecting the high quality of the SN vs AGN vs Noise ML model introduce in this section.

My best model, as described in Section 5.4.2.3, converges rapidly to the accuracy of 99.7%. Figure 5.16 shows the Receiver Operating Characteristic (ROC) which is the most commonly used metric of the accuracy of the classification model. The Area Under Curve (AUC) for the ROC has used an indicator that for each individual object's the probability of being a true positive vs a true negative. For this model, I have measured it to be 99.97%.

5.4.2.5 Selecting SNe

After the numerous preparation steps, we can now obtain classifications for each real, unlabelled DES transient. 19,500 objects were sanitised and reshaped using the same method as the training sample before being passed through the classification network. Amongst this sample, 6000 objects received a classification of 'most-likely' being a SN, e.g their probability was highest for this label.

To test the classification model and determine a probability threshold that would ensure a high purity of the sample, I use the samples of spectroscopically classified SNIa, CCSN, SLSNe and AGN as a ground-truth sample. Regardless of their subclass, all confirmed in the sample were correctly classified using our CNN and all AGN were also correctly accounted for. Furthermore, 99% in the worst cases, with an average exceeding 99.99%

for the majority of transients. This result confirms that the high degree of accuracy could not be attributed to overfitting or errors in the analysis but was, in fact, the true representation of the quality and ability for the CNNs to differentiate these classes of transients. The high level of accuracy suggests that a similar project performed on data with lower quality or more incomplete light curves could still result in a positive result paving way for similar methods to be applied in the future astronomical surveys including LSST.

Using the classification probability values measured for the confirmed objects, I set a conservative threshold of 98% to select objects which are to enter the next stage of my analysis. This retained 5273 objects which are an approximate match to the numbers of SN discoveries expected in DES (Bernstein et al., 2012).

5.4.3 Classifying SNe

Upon the classification of 5273 transients found in the first four years of operation of DES, the next step of the analysis is to attempt to divide these objects into their respective subclasses using only their light curve data. This task is perhaps one of the greatest challenges facing SN surveys to date, with no project ever accomplishing this with a high degree of confidence without as a modelling prior.

The classification of SN in the absence of the distance prior requires us to focus purely on the morphology of the light curve including its colour and temporal evolution and apparent luminosity as the only available sources of information. These differences may be very subtle for a number of SN classes, most predominantly SN Ia and SN Ibc, and we, therefore, do not expect to be able to produce a classification model matching the accuracy of that used to identify SN candidates in DES.

5.4.3.1 Data preparation and network selection

The training sample used in the classification of SNe is similar to that used in the previous section, albeit consisting of SN light only. In order to provide a fair representation for each subclass of objects, I use an equal sample of SN Ia, CCSN and SLSN in each case 45,000 objects from the training set. In the case of CCSNe, I use an even contribution from both the sample of SN II and SN Ibc. The data is also sanitised and reshaped using the tools as used in Section 5.4.2.1

To build the SN classification model, I use the approach developed in Section 5.4.2.3 as the benchmark, modifying that network to suit this more complex problem. Perhaps the most important change was the introduction of the magnitude as one of the input parameters. In the selection of SNe, performed in Section 5.4.2.3, this was not necessary as the light curve evolution, normalised to one for each object, provides sufficient information to distinguish between these very distinct classes of objects. In the case of SNe, the difference is very subtle relative to the previous model with the luminosity as a function of the colour likely being one of the strongest indicators for each subclass. The absolute luminosity is measured as the maximum flux in each band across all seasons of data. This provides only four additional data points and is, therefore, introduced late into the network in order to provide more weight in determining the final classification (Figure 5.17).

Another important change in this iteration of the CNN was an increase in the number of convolutional filters responsible for measuring the colour of the SN. Through a number of iterations of the model, I found that an increase from 30 to 50 unique filters improves the classification rate by $\sim$3% without overfitting the model.

Finally, one of the biggest improvements in the model came from modifying the activation function to follow the Tanh distribution over ReLU, introducing an improvement of $\sim$5%. Interestingly, the same behaviour was not previously observed in the SN identification network, where the use of Tanh or Sigmoidal activation functions hinders the classification rate. One possible explanation of this comes from the fact that the differences between the objects in the training samples in the SN identification sample are so large that they require a more flexible and forgiving activation function such as ReLU, while the similarity of the SN subclasses requires a very sensitive, high gradient function to be used. The benefit of the Tanh over a Sigmoid is the scaling between the negative and positive unity as opposed to zero and one, which allows for objects with small negative values.

5.4.3.2 Training the model

Using the training sample and the CNN developed in Section 5.4.3.1, I built a SN classification model that, with an accuracy of 90%, is one of the most successful SN classifiers to date, despite its independence from any distance priors. At the stage of classifying a purified sample of SNe, our result can be directly compared with Lochner et al. (2016). Our AUC measured at 97.9% for SN Ia marginally exceeds that of the best result found in Lochner et al. (2016). However, this does not tell the full story as the best model found in their work sufferers largely from overfitting and the more correct value, found using a larger (albeit non-representative of all subclasses) sample is closer to $\sim$85%. The accuracy of our classifier is again a testament to the power of CNNs, demonstrating that a similar model could be used in future surveys such as LSST.

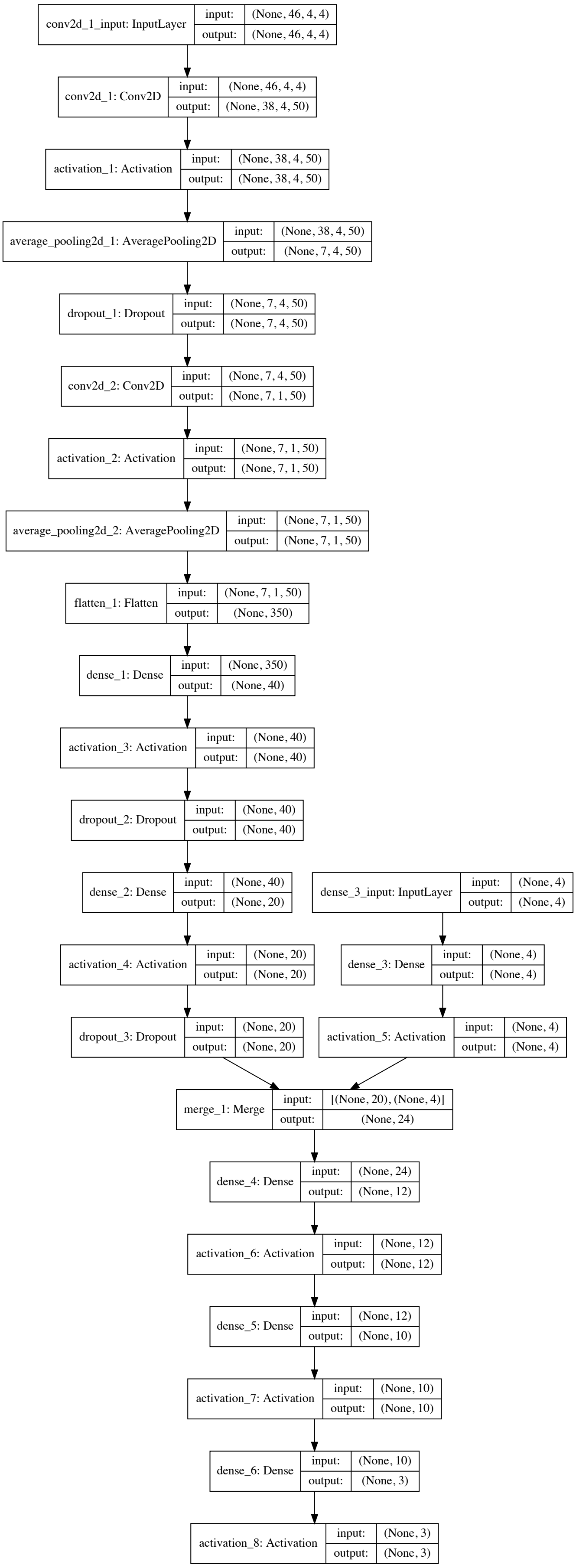

Figure 5.17: The CNN used to subclassify DES SNe amongst their spectral subtypes. This network relies on 'Tanh' activation functions and makes use of the information about the apparent luminosity of the SN, differing from that used in Section 5.4.2.3

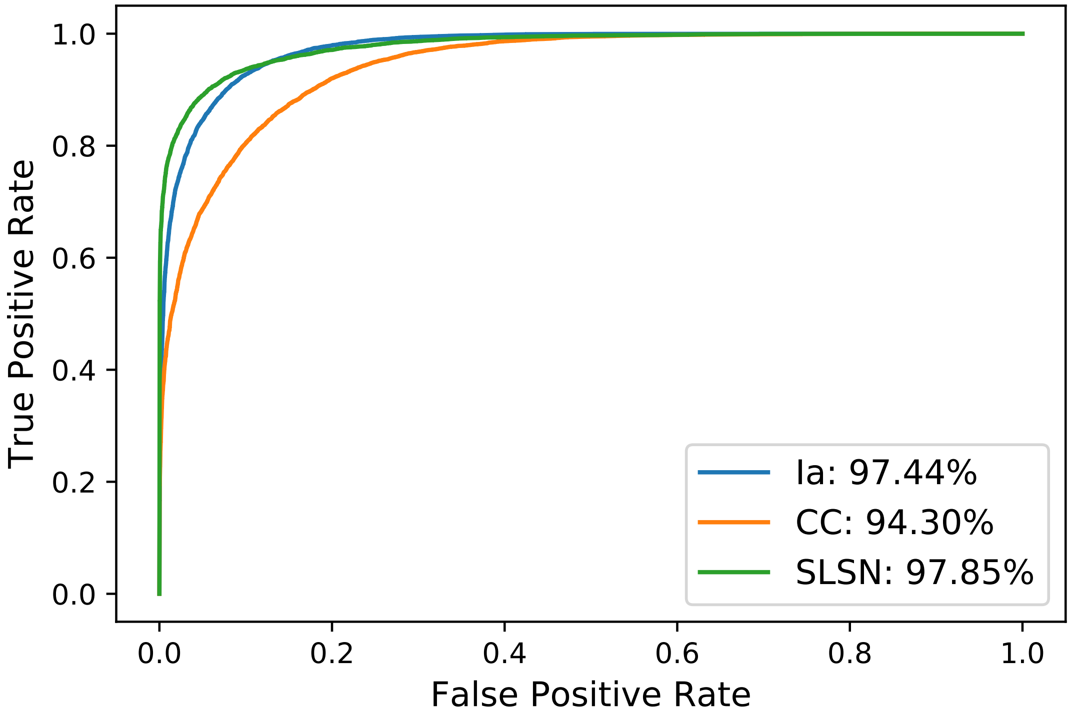

FIGURE 5.18: The ROC and AUC measured for the SN photometric classification model shown separately for each class of SN present in our training sample.

5.4.4 SLSNe in DES

Before the SN classification model can be applied to the sample of DES SN candidates, identified in Section 5.4.3.2, it must first be tested against the ground-truth sample of spectroscopically confirmed objects detected by DES. While the model shows that a high degree of precision, it is possible that mistakes in the creation of the artificial training sample could lead to some subclasses not being represented correctly in the classification model.

5.4.4.1 Ground-truth sample

Amongst the sample of 250 spectroscopically confirmed SN Ia, 243 are correctly in this work. This, in fact, exceeds the value expected from the raw accuracy figures, which are likely explained by the spectroscopically confirmed objects being easier to classify than some objects that may lay at the detection limit of the survey.

With this positive result, I apply the same method to SN Ib/c and SN II. Here the results begin to shed a light on a major issue uncovered in this section. While a majority of the SN Ib/c have been correctly identified, a number of SN II have been misidentified as SLSN. The visual inspection of these objects shows that they are exclusively SN IIP, with

Table 5.4: Percentage probability of the spectroscopically confirmed DES SLSNe as found in the ML photometric classification presented in this chapter.

SN Name	SN Ia	CCSN	SLSN
DES13S2cmm	0.04 %	89.18 %	10.77 %
DES15X3hm	5.65 %	7.40 %	86.95 %
DES14X3taz	1.71 %	2.25 %	96.04 %
DES15S2nr	0.01 %	0.54 %	99.46 %
DES14C1fi	0.00 %	0.11 %	99.89 %
DES14X2byo	0.01 %	0.10 %	99.89 %
DES15C3hav	46.10 %	10.38 %	43.52 %
DES14C1rhg	0.87 %	96.90 %	2.23 %
DES14S2qri	2.92 %	90.66 %	6.43 %
DES14E2slp	0.28 %	1.85 %	97.87 %
DES15E2mlf	0.00 %	0.23 %	99.77 %
DES15X1noe	3.63 %	52.81 %	43.56 %
DES15S1nog	19.93 %	14.05 %	66.02 %
DES16C3cv	0.00 %	0.04 %	99.96 %
DES16C2nm	0.00 %	0.05 %	99.95 %
DES16C2aix	0.05 %	46.19 %	53.76 %
DES16C3dmp	9.60 %	3.51 %	86.89 %
DES16C3ggu	85.20 %	11.52 %	3.28 %

particularly slow descent times. This is a subclass of objects which was not represented in the training sample due to the lack of sufficient data. At the current time, using the data available in the literature it is not possible to expand our training set with examples of SN IIP.

As a final check, I test the sample of DES SLSNe and find that 12 of the 18 objects are fully recovered by the model. While at the first glance, this appears to be in contradiction with the predicted accuracy of the classifier, two of these objects are known to be only tentatively classified as SLSN (DES15C3hav, DES14C1rhg). Three objects are known not to be a good match to the magnetar model under any assumptions tested in Section 3.1.2.2 (DES13S2cmm, DES14S2qri). It is harder to postulate why DES16C3ggu and DES15X1noe are not part of the sample.

5.4.4.2 SN classification

I applied the final classification model to the 5273 objects real DES objects, previously identified as SN candidates. At the 50% accuracy threshold, 3192 objects were identified as SN Ia which matches the expected values found in (Bernstein et al., 2012), 1389 objects were identified as CCSN which again does not exceed our expectations. The remaining 509 objects were identified as SLSN.

This exceeds the numbers expected from the rate of SLSN and is known to be contaminated with long duration SN IIP. However, as the classification model was shown in Section 5.4.4.1 to be able to identify a number of known SLSN with a high degree of accuracy (Table 5.4), we have a strong degree of belief that there are in fact numerous SLSN hidden in this contaminated sample that may be recoverable using further analysis.

5.5 Selecting SLSN Candidates

There is a number of techniques I can employ to help sanitise the sample to select true SLSNe candidates. In this section, I use the available redshift information to select objects exceeding the commonly used magnitude threshold as well as perform visual inspection searching for objects similar to SLSNe.

5.5.1 Removing Confirmed Contaminants

The first and the most straightforward step of the analysis is to remove the objects from the sample with a previous spectroscopic classification or strong photometric classification. Using the DES spectroscopic classifications excluded a total of 36 objects with 12 known to be SLSNe, 20 identified as 'SN II' and two SN Ia. An interesting observation is that I classified 20 out of 45 'SN II' as SLSNe which is likely to include a large proportion of SN IIP as DES does not subclassify the class of hydrogen-rich SNe.

The next step is to reject the objects which have previously been identified as likely SN Ia or CCSNe. DES uses a combination of light curve model fitting techniques to identify potential targets for spectroscopic follow-up. While the models for CCSN are not well developed and often lead to misclassifications, the SN Ia selection was based on the SALT2 model and therefore provides a good estimate of whether the object is a likely SN Ia. For all SLSNe in the spectroscopically confirmed sample, these probabilities have been very low, with the highest values, measured for DES15X3hav at $< 1\%$. I use a conservative cut at 10% probability for each model to exclude these objects, resulting in a sample of 194 potential SLSNe remaining.

5.5.2 Selection Using Redshift

One of the strongest methods of identifying SLSNe is the estimation of their absolute luminosity. This is possible for a large number of objects in the sample thanks to the extensive spectroscopic follow-up carried out by DES by the 4m AAT instrument.

Table 5.5: Sample of SLSN candidates with a spectroscopic redshift measurement placing them above the luminosity threshold most commonly associated with SLSNe.

SN Name	redshift	M_{max}
DES13C1nln	0.804	-20.36
DES13E1aftw	0.663	-20.11
DES13X1ayr	0.797	-20.97
DES13X1csy	0.844	-20.60
DES13X2eti	0.868	-21.10
DES13X3aajk	0.294	-19.88
DES13X3xyh	0.495	-19.84
DES14E1hek	0.653	-20.04
DES14X1qzi	0.694	-20.24
DES14X2eb	1.231	-20.99
DES14X3zq	0.992	-20.08
DES15C1ljb	0.894	-20.44
DES15C1rq	0.702	-19.87
DES15E1lwi	0.790	-20.23
DES16E1cjc	0.622	-19.89
DES16S1bzz	0.555	-20.35
DES16S2fqy	0.556	-19.94
DES16X2ewe	0.306	-19.88
DES16X2uq	0.666	-20.47

Using the AAOmega multi-fibre spectrograph, DES observed all detected object with no constraints on their photometric classification for a number of years after their discovery, stacking their spectra to increase their SN with the aim of measuring the redshifts for all DES transients based on the narrow emission features associated with their host galaxies. After four years of observations, the redshifts have been obtained for galaxies as faint as $m_i \sim 24.5$.

Amongst the remaining sample of SLSNe candidates, 95 objects have an AAT spectroscopic redshift measurement. Combining this with the observed light curves I select all objects with absolute luminosity, $M <$ -19.5 in the brightest photometric band and visually inspected the resulting sample to find 19 objects that meet this criterion (Table 5.5). Furthermore, I use the host galaxy photometric redshift estimates to select a further sample of seven candidates that meet the same criteria (Table 5.6).

5.5.3 Final Sample Selection

The visual inspections of the remaining sample of potential SLSNe, with no redshift information, showed that there are no clear features that would allow for the separation of the true SLSNe from SN IIP. Majority of light curves are found not to be complete or have a too low quality to allow for a selection method relying on the detection of the

Table 5.6: Sample of SLSN candidates with host galaxy photometric redshift estimates. These are not as reliable as the spectroscopic measurements but combined with their visual inspections, these appear as potential strong candidates.

SN Name	redshift	M_{max}
DES13E1nkg	1.09	-22.21
DES13X3obu	1.32	-21.06
DES14C1fs	0.74	-21.01
DES14C3aba	1.33	-21.22
DES15S1flm	0.91	-21.04
DES16X1bhk	1.12	-21.19
DES16X3cer	1.16	-23.20

characteristic plateau associated with SN IIP. A colour vs luminosity selection method has also proven unsuccessful due to the degeneracy between the redshift and colour for these two classes. As shown by the example of DES16C2nm, high redshift SLSN appears very similar to classical SNe at lower redshift due to their bright UV luminosity, with a SED drop off at a much lower wavelength.

In the light of this, I chose to only present the sample of candidates with a strong distance prior as part of this thesis. While this is not ideal, it provides a pure, unspeculative sample that gives us a better understanding of the population of DES SLSNe and doubles the side of the training sample that can be used to develop further techniques that in the future may be used to produce a complete sample of DES SLSNe.

5.5.4 Sample Properties

Looking at the samples (Appendix A) of SLSNe presented in tables 5.5 and 5.6, there is exidence for a discrepancy between the number of SLSN detected in the first season of DES and the remaining seasons. This is particularly curious as is the opposite behaviour to that of the spectroscopically confirmed sample. There are two likely causes of this bias; the AAT spectroscopic redshift measurements are still taking place and it is expected that they are, at this stage, only complete for the DES targets and will continue to be improved for the next several years resulting in a higher number of Y1 objects entering our sample. Further to this, the first DES season resulted in only one discovery of a SLSN in comparison to 6 in each subsequent season, leaving a larger pool of yet undiscovered prior to this work.

5.6 Summary

In this chapter, I described the approach used in building a training sample of transients resembling the sample of real transients observed by the DES. I used the SNANA generated sample of SN Ia. The CoCo and SLAP packages, developed in Chapter 3, were used to create samples of CCSN and SLSNe respectively. Furthermore, I use a sample of AGNs generated for a similar study in Hönig et al. (2017) and a basic model of spurious noise detections to generate a DES-like sample of real transients and their contaminants. I use the approach similar to that found in SNANA to apply the survey noise to the modelled light curves before augmenting them to a uniform cadence using GPR, previously discussed in Section 5.3.

This training sample was used to develop a classification pipeline for photometrically identifying a sample of real SN candidates in DES. This was performed in conjunction with the state of the art CNN algorithm. A similar approach was subsequently used to create a SN photometric classification tool. Our testing suggests that it is one of the most powerful tools of its kind currently available. I applied it to the DES dataset identifying 3192 SN Ia, 1389 potential CCSN and a sample of 500 SLSN, although we understand that this sample is heavily contaminated by SN IIP which were not included in the original training sample.

Using a large catalogue of spectroscopic and photometric redshift measurements for the DES transients, I finally present a sample of objects which match the luminosity of SLSNe. While this sample is already larger than that of the spectroscopically confirmed objects, it must still be seen as incomplete as it struggles to identify any high redshift SLSNe.

Chapter 6

Conclusions

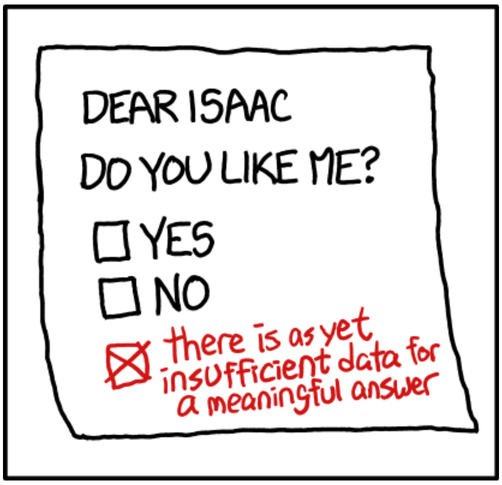

xkcd.com/1448

In this thesis, I aimed to demonstrate the ability to photometrically classify SLSNe amongst large samples of transients detected by modern, wide-field astronomical surveys. In order to achieve this, I combined our understanding of this class of objects with state-of-the-art Machine Learning and light curve modelling techniques to both define and predict their behaviour in a number of surveys. All this was performed with the aim of broadening our understanding of SLSNe as a population. The main results are summarised below.

6.1 Modelling SN light curves

In Chapter 3, I described the methods for modelling of CCSN and SLSN. I discussed the analytical models as well as the tools built to implement them. I have learned a number of lessons regarding the problems with modelling of both classes, as outlined in this chapter. I also describe the Bayesian approach to the problem of model optimisation and introduces Gaussian Process Regression as a tool for non-parametric, probabilistic light curve interpolation.

6.1.1 Modelling SLSNe

The simulations of SLSNe at any chosen redshift or bandpass were essential for this thesis. In Section 3.1.3, I demonstrated an approach to producing a high-quality SLSN SED model based on the black-body approximation of its continuum, combined with a spectral absorption template. The templates, focusing on the UV regions of the SED, significantly increased the redshift range at which it is possible to confidently model these objects. I combined this with the evolution of the bolometric luminosity of SLSNe based on the birth and spin-down of a magnetar model, modified to include a variable opacity term. I showed that this treatment of SLSNe correctly accounts for their light curve morphology including the late time evolution which is difficult to capture using other models.

6.1.2 Modelling CCSN

While CCSN are a better-understood class of transients than SLSNe, their simulation tools are still underdeveloped, especially when compared to those used for the modelling of SN Ia. Here, I developed a set of tool for simulating CCSNe, including both their hydrogen-poor and rich subclasses. I provide a self-contained solution, starting with the archival photometric and spectroscopic data for a number of nearby objects of these classes. After a number of models are trialled, I use an approach similar to Bazin et al. (2009) in order to provide an interpolation model used to flux calibrate the observed spectra in the process referred to as mangling. Based on this approach, I built CoCo, a tool for generating spectral templates and simulations of CCSNe.

The approach used in this thesis works on the principle of placing a spectral template at any required redshift, then passing it through a bandpass filter to measure the synthetic flux at the phases of the spectra before fitting a light curve model to them to obtain flux at any arbitrary point. Due to the wavelength limitations of ground-based spectroscopy, the SED had to be extended in both IR and UV regimes. I used a combination of auxiliary *Swift*-UVOT data and the modelling of their continuum as dust extinct black-bodies to achieve a wavelength coverage reaching as low as $\sim 1500\AA$, sufficient to obtain the flux of a CCSN in the DES *g*-band at their detection limit of z∼0.7.

6.1.3 Light Curve interpolation using Gaussian Processes

Throughout this thesis, I used GPR as a method for light curve interpolation. Upon comparing a number of popular covariance functions, I determined that the Mateŕn 3/2 kernel best suits the light curve data familiar to this work. I found it to be the best overall match to all classes of SN detected by DES and a good fit to highly variable objects such as AGNs, that form a large fraction of the transients observed by DES. This approach has been shown to successfully fit all transients in the artificial and well as DES transients samples, demonstrating its robustness.

6.2 Rates of SLSN

Chapter 4 of this thesis focused on measuring the rate of SLSNe at the intermediate redshift of z∼1. This was motivated by the low numbers of similar measurements, despite being a crucial piece of the puzzle of the origin on SLSNe. In this work, I provide one of the most accurate measurements of the rate, allowing us for the first time, to probe its evolution with redshift as well as the connection to other rare classes of transients.

6.2.1 Defining SLSNe

Starting from the SLSN model, based on the spin-down of a magnetar, I postulated a definition the SLSNe. After fitting the literature sample of these objects with the model, I found all SLSNe to concentrate in a small region of the P_{ms}-B_{14}-τ_M parameter space, clearly separated from a majority of transients detected my SNLS. I parametrised this region using an ellipsoid that tightly encapsulates the entire training sample, giving a definition of SLSNe in terms of the parameter space of the magnetar model.

6.2.2 Search for SLSN in SNLS

I used this proposed definition of SLSNe to search for the presence of new, previously unclassified objects in the SNLS. Upon fitting the entire archival sample of transients, taking either their precise spectroscopic redshift (where available) or a range of host galaxy photometric redshift estimates, I find that only two new objects fall within my definition. While one of them shows clear signs of multiseason variability, the second object, SNLS07D3bs, was found to be a strong SLSN candidate. My modelling suggested a good match to the class at $0.6<z<1$. Using a low SnN, archival spectrum of the object we were unable to confirm the classification, however, we used narrow line features to determine the true redshift of the object as z=0.74, confirming that the object is consistent with the luminosity of a SLSN.

6.2.3 Rate of SLSNe at z∼1

With three SLSN candidates found in the SNLS, I performed a Monte Carlo simulation of the survey, replicating its transient detection behaviour. This reversed the common approach of calculating the rate of SNe by weighing each object by its detection efficiency and observed volume. Instead, I simulated SLSNe before applying the survey noise and measuring each objects detectability in the survey. In the simulations, I iterated over a range of rate values, measuring the resulting number of SLSN detections. I then transpose these results to give me the probability of detecting 3 objects as a function of the input value. I found the rate of SLSNe, at z∼1, to be $91^{+76}_{-36}\,\mathrm{SNe\,Yr^{-1}\,Gpc^{-3}}$ or $2.2^{+1.8}_{-0.9} \times 10^{-4}$ of the CCSN rate. This is consistent with similar publications and tentatively demonstrates that the rate of SLSNe follows that of the cosmic star formation rate.

6.2.4 Connection between SLSNe and ULGRBs

An interesting question probed in Prajs et al. (2016) is the connection between the classes of SLSNe and ULGRBs. LGRB are known to be connected to ordinary, stripped-envelope SNe which, under certain circumstances, result in the formation of a collapsar, or a jet forming young black hole powered by the infalling ejecta. Thanks to the advances in GRB observation provided by the *Swift* satellite, we now know that some LGRB are observed to emit γ-radiation bursts lasting up to 10,000s (Levan et al., 2014). A correction has been recently drawn between this class of ULGRBs and SLSNe, thanks to the discovery of GRB 111209A. Observed simultaneously as SN2011kl, a SN with a luminosity, light curve morphology and spectroscopic characteristics similar to other lower luminosity SLSNe (Greiner et al., 2015).

ULGRB are known to be rarer than ordinary LGRBs with their exact rate difficult to estimate due to the *Swift* observations and GRB triggering mechanism being optimised to detect short transients, likely leading to a loss of many potential candidates. In Prajs et al. (2016), we have approximated the rate of ULGRBs based on the estimates of the key components of the measurement. Taking 10 years of *Swift* observations, detecting ULGRBs up to z∼ 1.3 with a 17% sky coverage an approximate detection and classification efficiency of 30% we find the rate of ULGRBs to be $\rho_{\mathrm{ULGRB}} \sim 30\ \mathrm{Gpc^{-1}yr^{-1}}$. In contrast to SLSNe, this measurement depends on the beam angle of the γ-emission as

GRBs do not radiate isotropically. We used an opening angle of $\theta = 12^\circ$ which can be seen as a conservative estimate, in line with the other values used here, resulting in this estimate to be seen as a lower limit on the true rate. Regardless, it is of particular interest that the value estimated for both SLSNe and ULGRBs appear very close, perhaps giving more evidence to their intrinsic connection and a shared physical origin.

6.3 Photometic classification of SN

Photometric classification of SNe forms the centre piece of this thesis. Performed using a number of methods, I demonstrate that the ML approach is the most powerful and successful, albeit, not the most straightforward to implement solution. While it required the construction of a large, artificial training sample, the results obtained using this method have largely exceeded the capabilities of other tools publically available to date.

6.3.1 Training sample

Using the combination of readily available models for SN Ia and AGNs as well as custom build models of SLSNe and CCSN, I have built a large training sample of transient light curves. I applied survey noise and cadence to match its properties with the real DES transient sample. The final sample consisted of ∼300,000 objects, therefore being the largest to date light curve collection used for a photometric classification study and represents objects from low redshift, local objects to those that lay at the edge of DES detectability.

6.3.2 Machine Learning Model

I developed a two-stage approach to the problem of classifying DES transients in order to reduce the number of free parameter in the model. In the first step, I separate SNe (regardless of their class) from other contaminants in the sample, including AGNs and spurious noise detections. This focuses on long-term variability of the object rather than their detailed evolution, used in the next stage to subdivide the SN sample into their respective classes. This approach produces an excellent classification rate, correctly identifying 99.81% SNe in the training sample. This was verified using a ground-truth sample where all spectroscopically confirmed transients (SNe and AGN) were correctly identified in this work.

Similarly to the SN identification pipeline, the SN classification algorithm exceeded our accuracy expectations. Compared to other similar projects, I did not use the spectroscopic redshift as a classification prior but, with a 97.85% classification rate, I achieved a higher precision than reported by the current state-of-the-art solution (Lochner et al., 2016). Upon identifying the sample of DES SNe, consisting of 5273 objects, I tested the model against a ground-truth sample of spectroscopically confirmed SN Ia, correctly identifying 243 out of 250 objects. It is even more encouraging to mention that the misclassified objects formed extreme season edge cases where no data was observed near the maximum light for these objects.

Applying this technique to the full sample of DES transients, I identified 3120 potential SN Ia as well as 509 SLSN candidates. The later number vastly exceeded our expectations based on the rate of SLSNe measured in Chapter 4. The visual inspection of the data showed that the sample is heavily contaminated by SN IIP, with characteristic long, red and plateauing light curves. We can attribute this to the lack of similar objects in the training sample as no objects of this class have passed the quality cuts required to generate a CoCo template

6.3.3 Selecting SLSN

Starting with a sample of 509 potential SLSN candidates, I used the auxiliary information on the objects including their host galaxies spectroscopic and photometric redshift measurements to analyse the sample, producing a pure sample of viable SLSN candidates. I used the redshifts measured by the AAT instrument to select 26 objects with an absolute luminosity, in its brightest photometric band, greater than $M_{mathrmmax} <$ -19.5.

Amongst this sample, I discovered 10 SLSN candidates in the first season of DES where only one candidate has previously been known, solving one of the big mysteries of the DES sample of SLSNe. However, no objects have been identified at redshift comparable or exceeding that of DES16C2nm demonstrating the need for a deeper analysis of the objects selected here and a development of more robust models of SN IIP that could be used to inform the ML classification tools.

6.4 Future Work

Having developed a successful approach for the photometric classification of SLSNe in large astronomical surveys, there are a number of avenues that I would like to pursue in the future. This includes the improvement and application of the method to in other surveys as well as using the archival data to solve some of the yet to be explained mysteries of SLSNe.

6.4.1 Expanding the Training Sample

One of the biggest issues identified in the process of photometrically classifying SLSNe was the incompleteness of the SN sample used in the training of the ML algorithm. The lack of examples of SN IIP had the greatest effect as it introduces a large number of impurity in the sample of SLSNe. However, the lack of other classes including rapidly evolving SNe and Tidal Disruption events also means that we cannot treat the samples of photometrically identified SN Ia and CCSNe as a pure sample.

In this thesis, the training sample was based on the spectroscopic templates for each class generated from the archival data for some of their most well-observed examples. While the techniques have generally varied in details, they all required spectroscopic data to an extent. However, for a number of classes or rare and fast transients, spectroscopy is very scarce while their photometries remain relatively abundant. A new approach, not requiring such extensive commitment from the data, is needed to extend the training samples. A possible solution, requiring a large commitment of resources, would be to use physically motivated simulations to produce a sample of objects and test their similarity to the available photometric samples. This approach is likely the most viable for the problem of modelling SN IIP where we could base the modelling on the existing simulations (Dessart et al., 2013, 2016).

6.4.2 Rates of SLSNe from DES

A natural extension of the work undergone in Chapter 4 is to use the sample of SLSNe found in Chapter 5 to compute their rate. The increase from 3 to 43 objects, compared to SNLS, would result in a vastly decreased uncertainties in the overall measurement. More importantly, it will be the first-ever measurement allowing for a separation of the rate into separate redshift bins using a single, homogeneous sample. With a tenfold increase in the observing area of the survey, the computational resources required to calculate the rate using the approach used in SNLS would likely be prohibitive. However, as part of the process of building the artificial sample of SLSNe, I simulated a large number of the randomly generated object throughout DES. While the main objective of this was to generate a sample of detectable SLSNe, the detection efficiency for each artificial SN is a by-product of this process. This gives us the tools necessary to calculate the detection efficiency of DES SLSNe by comparing their magnetar model fits those of the artificial sample.

6.4.3 Selecting SLSN in LSST

In the upcoming decade, LSST will dominate the landscape of optical astronomy and change the way that astronomers approach data reduction and selection of candidates for further follow-up. It is predicted that ∼10,000 SLSNe will be detected by the survey every year in the shallow fields as the longer cadence and all-sky coverage are ideal for the detection of these slowly evolving SNe. However, with such high number of objects and the millions of possible contaminants, the traditional non-ML methods of photometric classification would be too computationally prohibitive, as well as likely not effective.

The method proposed in Chapter 5 is a promising approach to the problems faced by LSST, however, a pure CNN approach can only be directly used with relatively long light curves making it impossible to target these objects for spectroscopic follow-up during their early rise-time phases. One possible extension that may be introduced to the current method is the use of the intermediate layers of the CNN as a way of identifying the light curve features which are most indicative of SLSNe. While this is not as powerful as a full CNN treatment, it would largely decrease the number of potential candidates and along with other auxiliary information, including the host galaxy properties and redshift.

6.4.4 Redshift estimation for photometric SN Ia in DES

Perhaps one of the most interesting results in this thesis, not directly related to the main subject of SLSNe, is the accuracy of the photometric classification of SN Ia. This is likely a reflection on the maturity of the model used to build the training sample of this class as well as our understanding of its parameter spaces. The lack of use of a redshift prior in the ML classification was motivated by the majority of objects in the real DES transient sample not being associated with an accurate redshift measurement. However, this information is present for each artificially generated light curve and could be used to estimate the redshift of the real DES SN Ia. This proposed new method would not require its estimation from model fitting but could be learned directly from the data given a sufficiently large data set.

6.5 Final remarks

The field of SLSNe research is still in its early stages. With the upcoming era of LSST, the numbers of SN detections are going to change the way we approach their properties, shifting fully from the study of individual objects to their statistical properties as a whole. We do not, however, have to wait until the LSST first light to begin this work. In this thesis, I demonstrated that the number of SLSNe detected by DES, each containing a high quality light curves and a wealth of supplementary data, by the nature of the survey, likely exceeds the total number of SLSNe discovered prior to DES. There are still a number of hidden secrets in the data, including many SLSN at z $\sim$ 2 waiting to be discovered by the next generations of ML algorithms.

Appendix A

Light Curves of SLSNe in DES

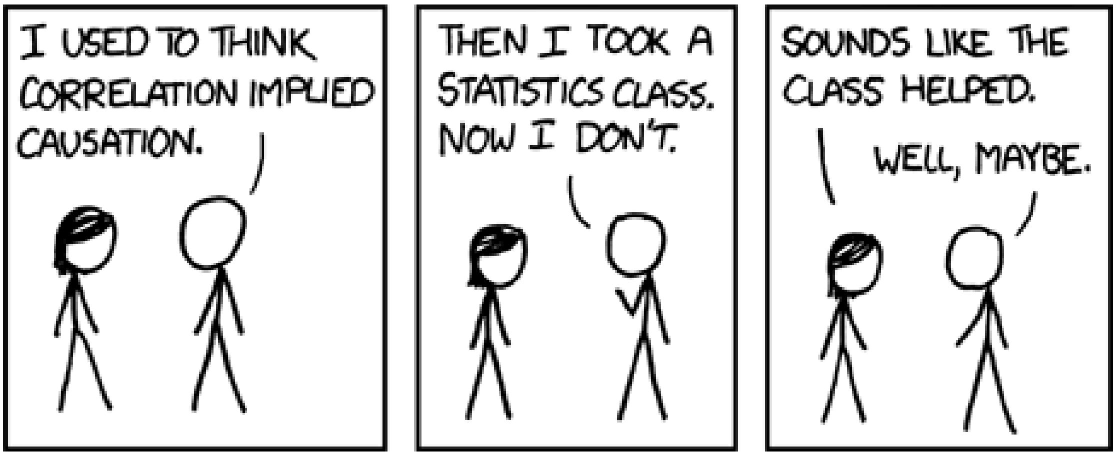

xkcd.com/552

A.1 Light Curves of Photometrically Classified SLSNe in DES

Below, I include the light curves of SLSNe classified using the ML photometric classification method developed in Chapter 5.

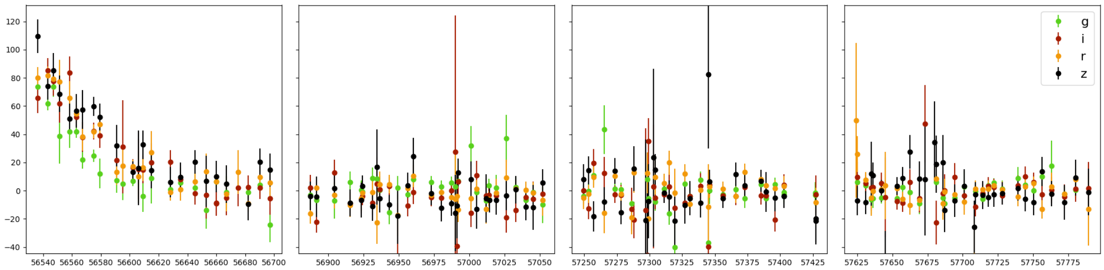

FIGURE A.1: DES13X2eti

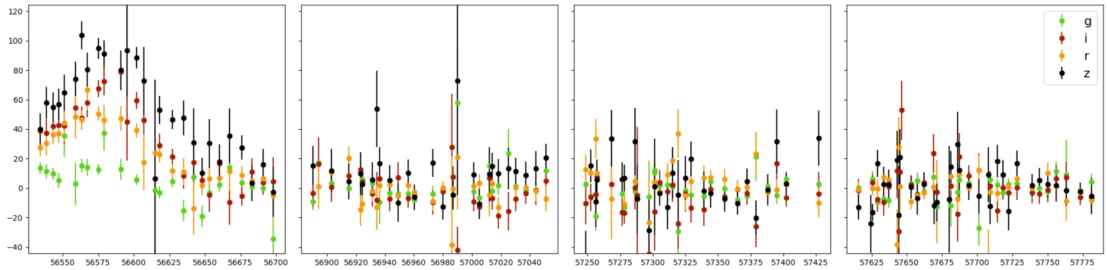

Figure A.2: DES13X1ayr

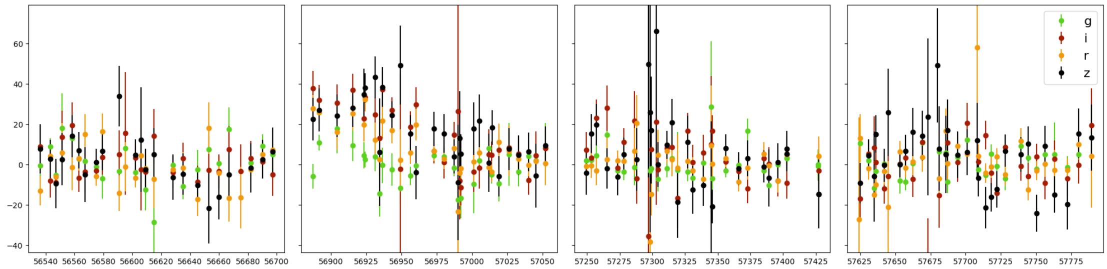

Figure A.3: DES14X2eb

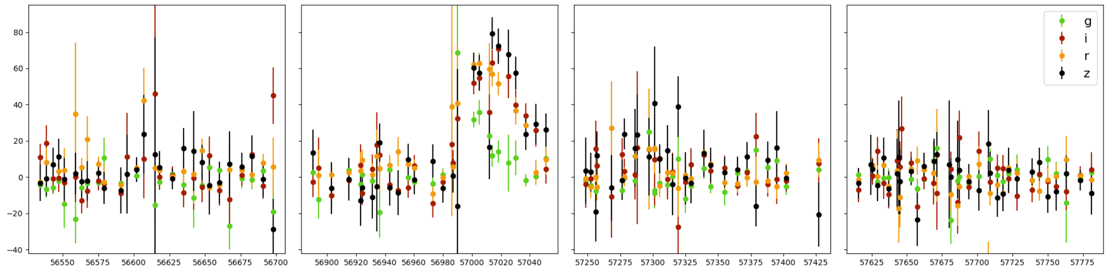

Figure A.4: DES14X1qzi

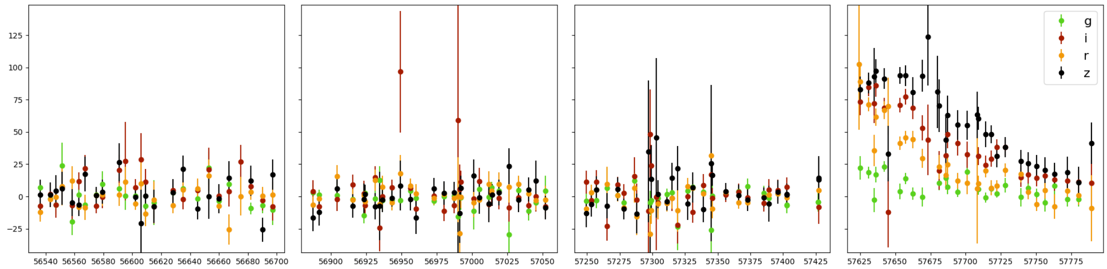

Figure A.5: DES16X2uq

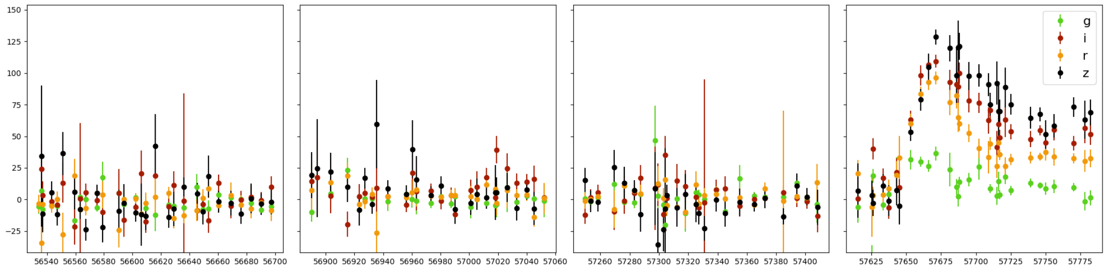

Figure A.6: DES16S1bzz

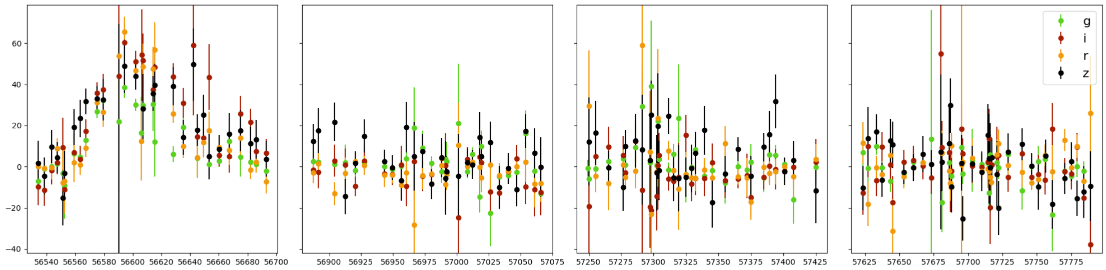

Figure A.7: DES13C1nln

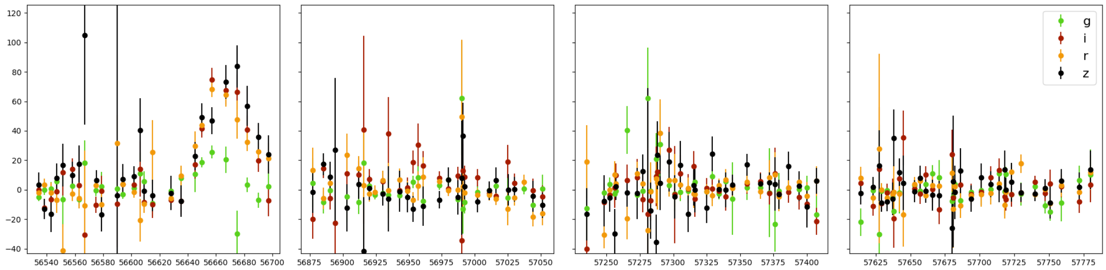

Figure A.8: DES13E1aftw

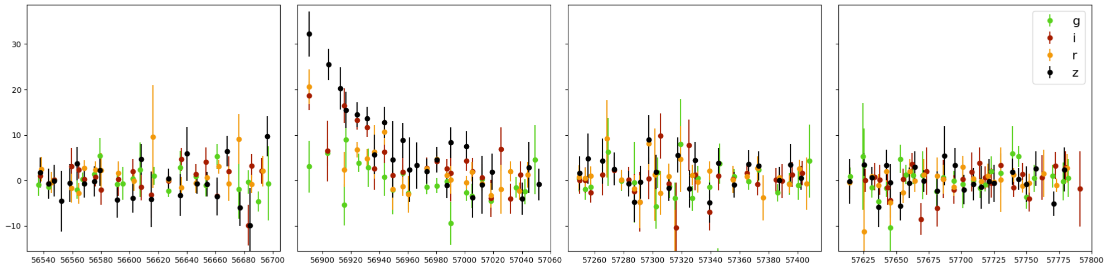

Figure A.9: DES14X3zq

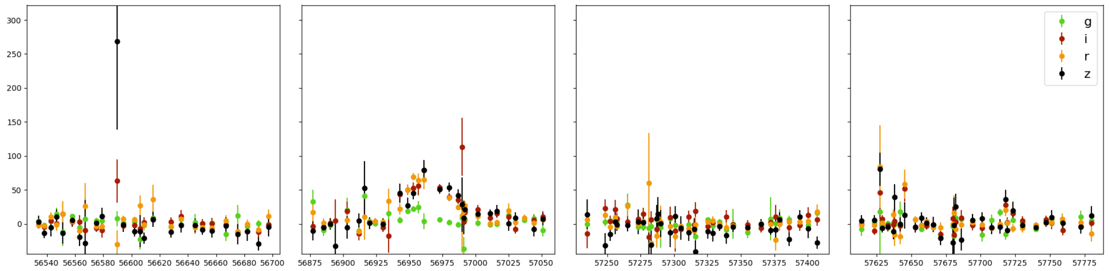

FIGURE A.10: DES14E1hek

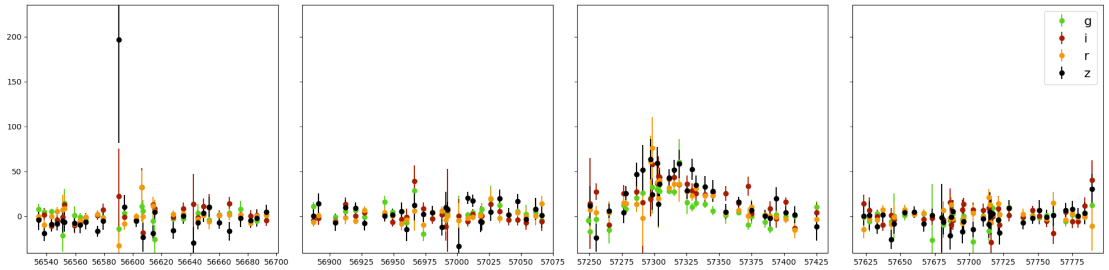

FIGURE A.11: DES15C1ljb

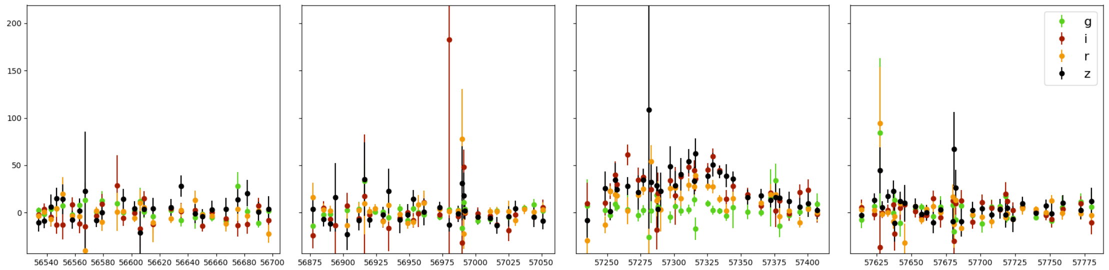

FIGURE A.12: DES15E1lwi

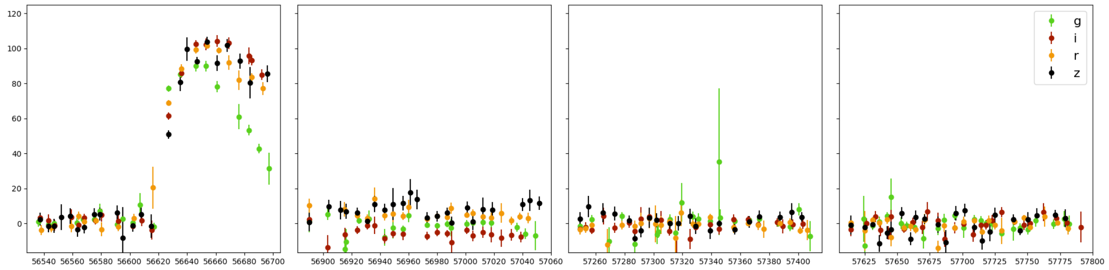

FIGURE A.13: DES13X3xyh

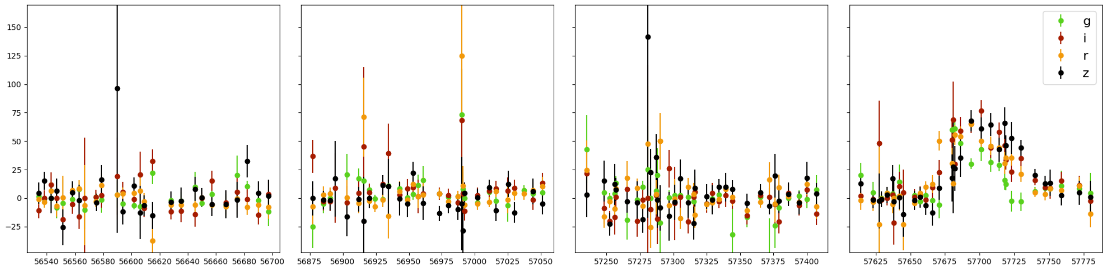

Figure A.14: DES16E1cjc

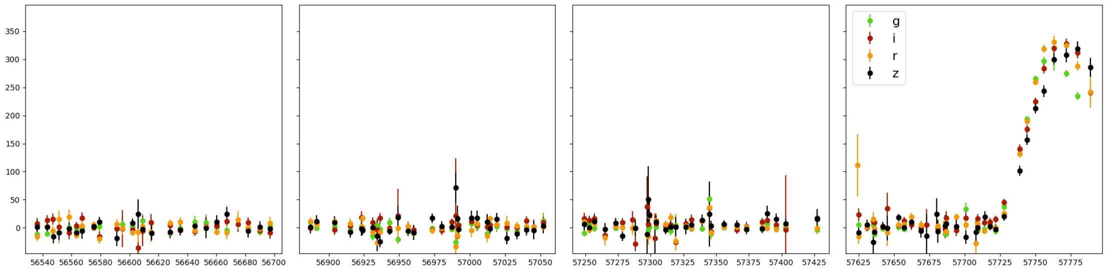

Figure A.15: DES16X2ewe

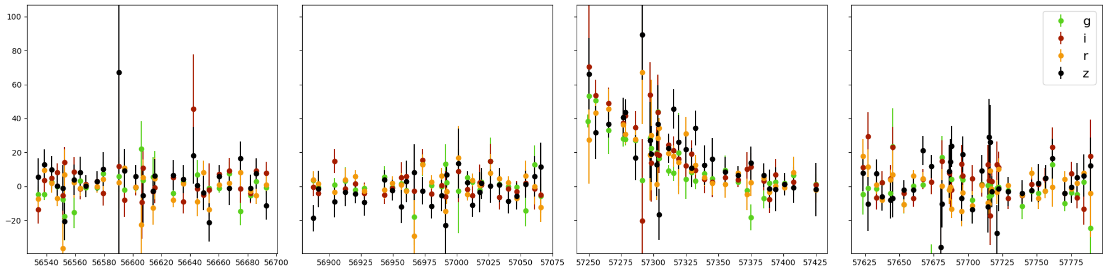

Figure A.16: DES15C1rq

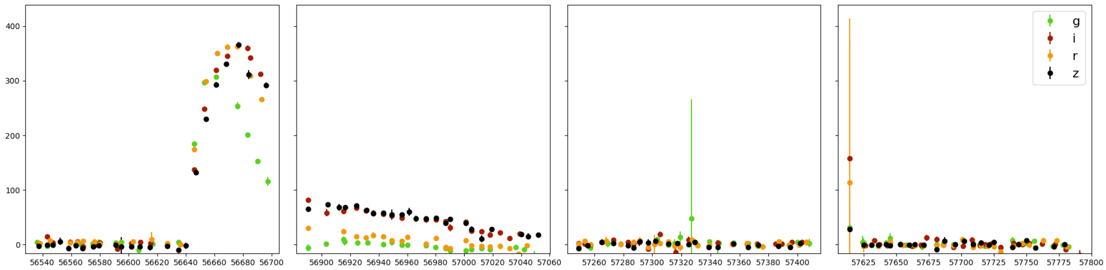

Figure A.17: DES13X3aajk

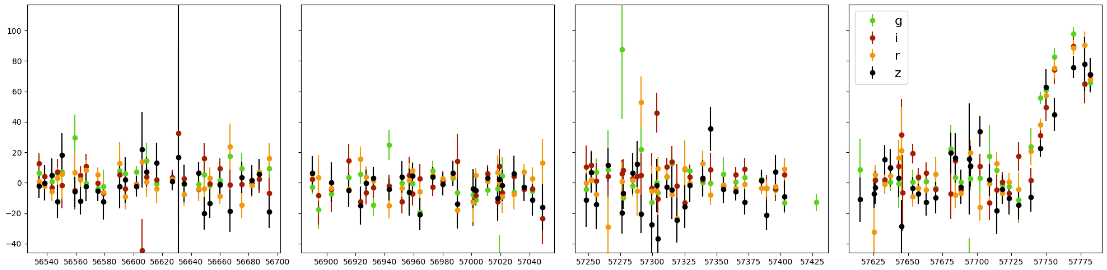

FIGURE A.18: DES16S2fqy

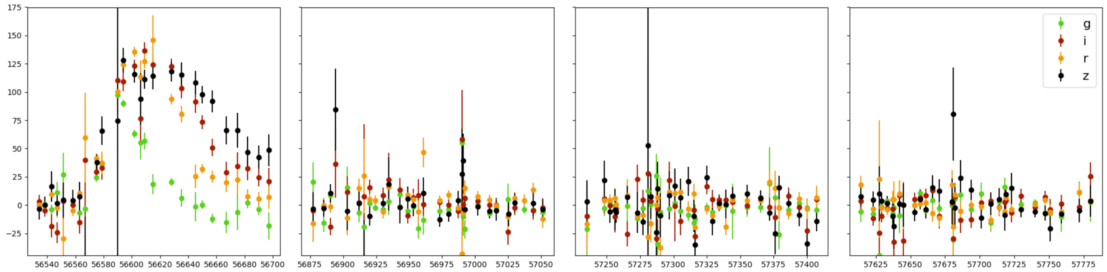

FIGURE A.19: DES13E1nkg

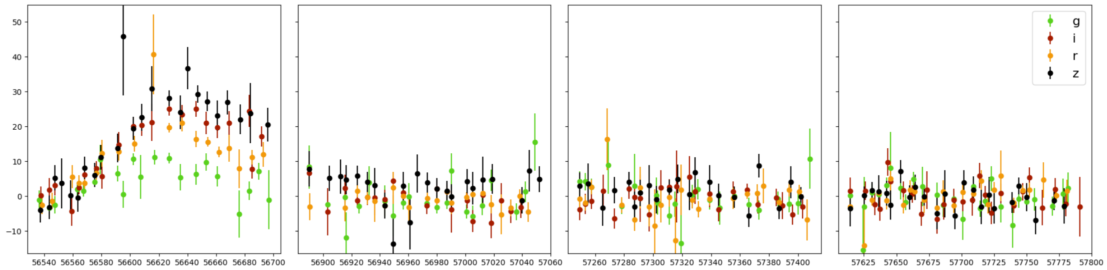

FIGURE A.20: DES13X3obu

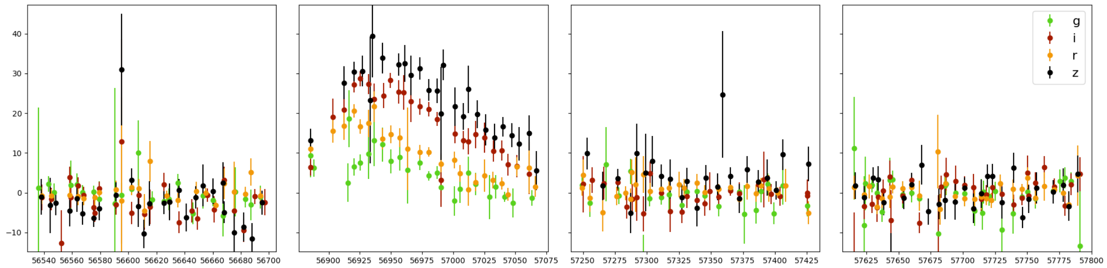

FIGURE A.21: DES14C3aba

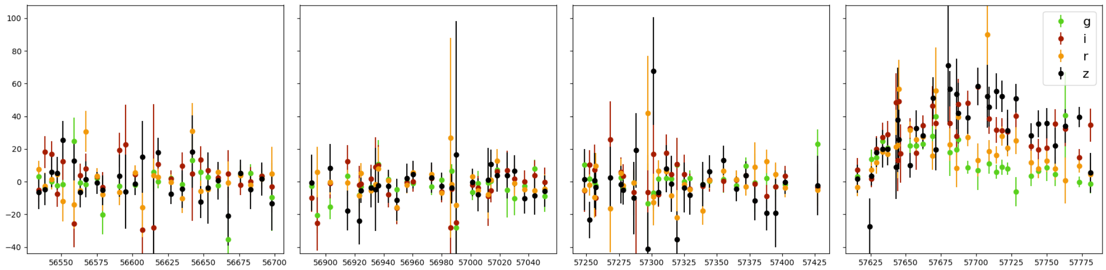

Figure A.22: DES16X1bhk

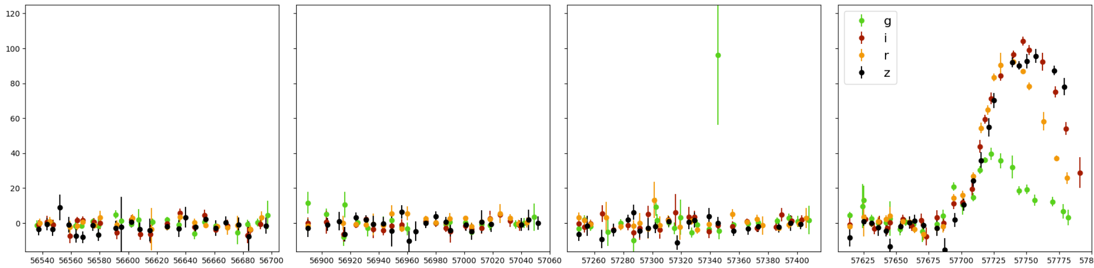

Figure A.23: DES16X3dlk

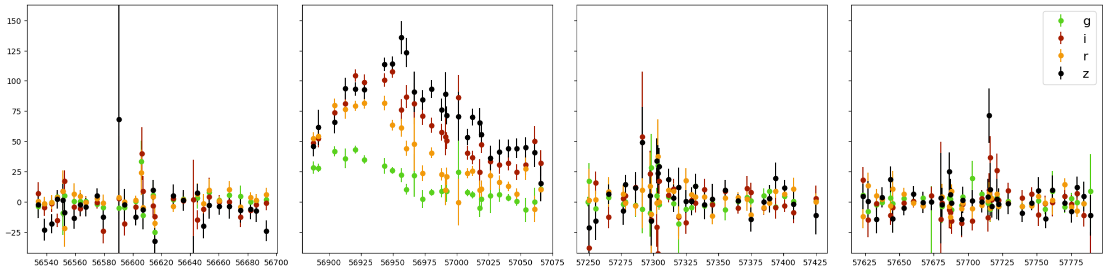

Figure A.24: DES14C1fs

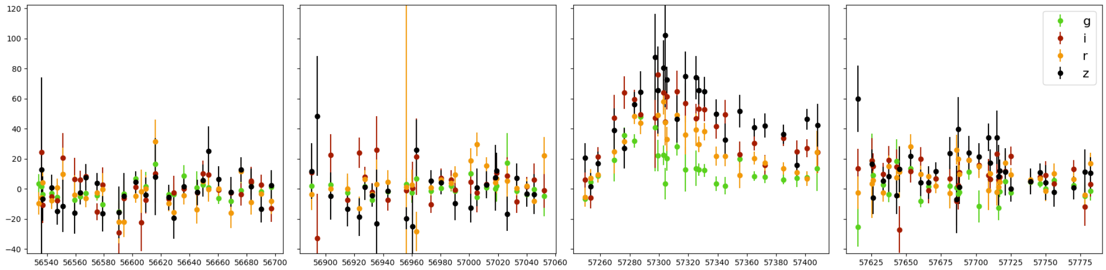

Figure A.25: DES15S1flm

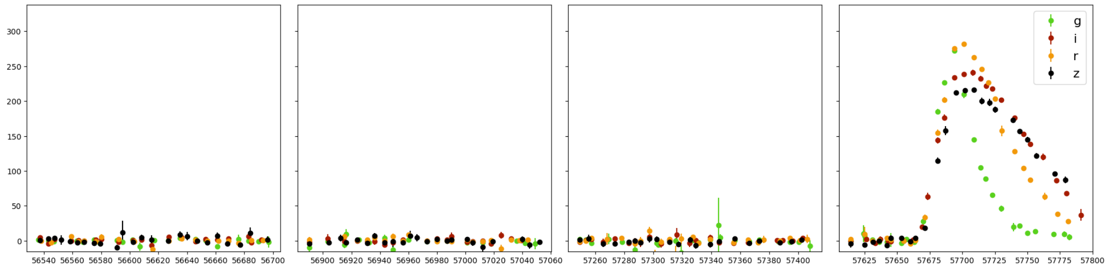

Figure A.26: DES16X3cer

Bibliography

Abbott, T. M. C., Abdalla, F. B., Allam, S., et al. 2018. https://arxiv.org/abs/1801.03181

Adam, R., Ade, P. A. R., Aghanim, N., et al. 2016, Astron. Astrophys., 594, A1, doi: 10.1051/0004-6361/201527101

Alard, C., & Lupton, R. H. 1997. https://arxiv.org/abs/9712287v1

Alsabti, A. W., & Murdin, P. 2017, Handbook of Supernovae, doi: 10.1007/978-3-319-20794-0. http://link.springer.com/10.1007/978-3-319-20794-0

Ambikasaran, S., Foreman-Mackey, D., Greengard, L., Hogg, D. W., & O 'neil, M. 2014

Angus, C. R., Levan, A. J., Perley, D. A., et al. 2016, Mon. Not. R. Astron. Soc., 458, 84, doi: 10.1093/mnras/stw063

Arcavi, I., Wolf, W. M., Howell, D. A., et al. 2016, Astrophys. J., 819, 35, doi: 10.3847/0004-637X/819/1/35

Arnett, W. D. 1982, Astrophys. J., 253, 785, doi: 10.1086/159681

Aspvall, B., & Stone, R. E. 1980, Elsevier J. Algorithms, 1, 1

Astier, P., Guy, J., Regnault, N., et al. 2005, Astron. Astrophys. Vol. 447, Issue 1, Febr. III 2006, pp.31-48, 447, 31, doi: 10.1051/0004-6361:20054185

—. 2006, Astron. Astrophys., 447, 31, doi: 10.1051/0004-6361:20054185

Baade, W., & Zwicky, F. 1934, Proc. Natl. Acad. Sci., 20, 254, doi: 10.1073/pnas.20.5.254

Balland, C., Baumont, S., Basa, S., et al. 2009, Astron. Astrophys., 507, 85, doi: 10.1051/0004-6361/200912246

Barbary, K. 2014, doi: 10.5281/ZENODO.11938

Barbary, K., Dawson, K. S., Tokita, K., et al. 2009, Astrophys. J., 690, 1358, doi: 10.1088/0004-637X/690/2/1358

Bazin, G., Palanque-Delabrouille, N., Rich, J., et al. 2009, A&A, 499, 653, doi: 10.1051/0004-6361/200911847

Bazin, G., Ruhlmann-Kleider, V., Palanque-Delabrouille, N., et al. 2011, Astron. Astrophys., 534, A43, doi: 10.1051/0004-6361/201116898

Bernstein, J. P., Kessler, R., Kuhlmann, S., et al. 2012, Astrophys. J., 753, 152, doi: 10.1088/0004-637X/753/2/152

Bertin, E. 2011, Analysis, 442, 435

Betoule, M., Kessler, R., Guy, J., et al. 2014, Astron. Astrophys., 568, A22, doi: 10.1051/0004-6361/201423413

Blanton, M. R., & Roweis, S. 2006, \aj, 133, 734, doi: 10.1086/510127

Boulade, O., Charlot, X., Abbon, P., et al. 2003, in Society of Photo-Optical Instrumentation Engineers (SPIE) Conference Series, Vol. 4841, Instrum. Des. Perform. Opt. Ground-based Telesc., ed. M. Iye & A. F. M. Moorwood, 72, doi: 10.1117/12.459890. http://proceedings.spiedigitallibrary.org/proceeding.aspx?doi=10.1117/12.459890

Bridle, S. 2002, Phys. Rev. D - Part. Fields, Gravit. Cosmol., 66, doi: 10.1103/PhysRevD.66.103511

Bronder, T. J., Hook, I. M., Astier, P., et al. 2007, Astron. Astrophys., 477, 717, doi: 10.1051/0004-6361:20077655

Brun, R., & Rademakers, F. 1997, Nucl. Instruments Methods Phys. Res. Sect. A Accel. Spectrometers, Detect. Assoc. Equip., 389, 81, doi: 10.1016/S0168-9002(97)00048-X

Burrows, A., Dessart, L., Livne, E., Ott, C. D., & Murphy, J. 2007, Astrophys. J., 664, 416, doi: 10.1086/519161

Burrows, A., & Lattimer, J. M. 1987, Astrophys. J., 318, L63, doi: 10.1086/184938

Cardelli, J. A., Clayton, G. C., & Mathis, J. S. 1989, Astrophys. Journal, Part 1 (ISSN 0004-637X), vol. 345, Oct. 1, 1989, p. 245-256., 345, 245, doi: 10.1086/167900

Charnock, T., & Moss, A. 2016, Astrophys. J., 837, L28, doi: 10.3847/2041-8213/aa603d

Chatzopoulos, E., Wheeler, J. C., Vinko, J., Horvath, Z. L., & Nagy, A. 2013, Astrophys. J., 773, 76, doi: 10.1088/0004-637X/773/1/76

Chen, K.-J., Moriya, T. J., Woosley, S., et al. 2017, doi: 10.3847/1538-4357/aa68a4

Chen, T. W., Smartt, S. J., Bresolin, F., et al. 2013, Astrophys. J. Lett., 763, L28, doi: 10.1088/2041-8205/763/2/L28

Chevalier, R. A., & Irwin, C. M. 2011, Astrophys. J. Lett., 729, L6, doi: 10.1088/2041-8205/729/1/L6

Chomiuk, L., Chornock, R., Soderberg, A. M., et al. 2011, Astrophys. J., 743, 114, doi: 10.1088/0004-637X/743/2/114

Clayton, D. D. 1968, 612/372

Cole, S., Percival, W. J., Peacock, J. A., et al. 2005, The 2dF Galaxy Redshift Survey: Power-spectrum analysis of the final data set and cosmological implications, doi: 10.1111/j.1365-2966.2005.09318.x. http://arxiv.org/abs/astro-ph/0501174http://dx.doi.org/10.1111/j.1365-2966.2005.09318.x

Connolly, A. J., Csabai, I., Szalay, A. S., et al. 1995, Astron. J., 110, 2655, doi: 10.1086/117720

Cooke, J., Sullivan, M., Gal-Yam, A., et al. 2012, Nature, 491, 228, doi: 10.1038/nature11521

Dark Energy Survey Collaboration, Abbott, T., Abdalla, F. B., et al. 2016, Mon. Not. R. Astron. Soc., 460, 1270, doi: 10.1093/mnras/stw641

De Cia, A., Gal-Yam, A., Rubin, A., et al. 2017a, Astrophys. J., 860, 100, doi: 10.3847/1538-4357/aaac2f

—. 2017b, Astrophys. J., 855, 2, doi: 10.3847/1538-4357/aaac2f

—. 2017c. https://arxiv.org/abs/arXiv:1708.01623v1

DePoy, D. L., Abbott, T., Annis, J., et al. 2008, in , 70140E, doi: 10.1117/12.789466. https://arxiv.org/pdf/0810.3600.pdfhttp://proceedings.spiedigitallibrary.org/proceeding.aspx?doi=10.1117/12.789466

DES Collaboration, Abbott, T. M. C., Abdalla, F. B., et al. 2017. https://arxiv.org/abs/1708.01530

Dessart, L., Hillier, D. J., Waldman, R., & Livne, E. 2013, Mon. Not. R. Astron. Soc., 433, 1745, doi: 10.1093/mnras/stt861

Dessart, L., John Hillier, D., Audit, E., Livne, E., & Waldman, R. 2016, Mon. Not. R. Astron. Soc., 458, 2094, doi: 10.1093/mnras/stw336

Dilday, B., Howell, D. A., Cenko, S. B., et al. 2012, doi: 10.1126/science.1219164

Drake, A. J., Djorgovski, S. G., Mahabal, A., et al. 2011, Astrophys. J., 735, 106, doi: 10.1088/0004-637X/735/2/106

Drlica-Wagner, A., Sevilla-Noarbe, I., Rykoff, E. S., et al. 2017, ArXiv e-prints. https://arxiv.org/abs/1708.01531

Drout, M. R., Chornock, R., Soderberg, A. M., et al. 2014, Astrophys. J., 794, doi: 10.1088/0004-637X/794/1/23

Ebden, M. 2015. https://arxiv.org/abs/1505.02965

Eisenstein, D. J. 2005, New Astron. Rev., 49, 360, doi: 10.1016/j.newar.2005.08.005

Ellis, R. S., Sullivan, M., Nugent, P. E., et al. 2008, Astrophys. J., 674, 51, doi: 10.1086/524981

Fakhouri, H. K. 2013, PhD thesis, University of California, Berkeley. https://ui.adsabs.harvard.edu/{#}abs/2013PhDT.......150F/abstract

Feroz, F., Hobson, M. P., & Bridges, M. 2009, Mon. Not. R. Astron. Soc., 398, 1601, doi: 10.1111/j.1365-2966.2009.14548.x

—. 2011, Astrophys. Source Code Libr., 9006, doi: 10.1111/j.1365-2966.2009.14548.x

Feroz, F., Hobson, M. P., Cameron, E., & Pettitt, A. N. 2013, ArXiv e-prints. https://arxiv.org/abs/1306.2144

Filippenko, A. V. 1997, Annu. Rev. Astron. Astrophys., 35, 309, doi: 10.1146/annurev.astro.35.1.309

Firth, R. E., Sullivan, M., Gal-Yam, A., et al. 2015, Mon. Not. R. Astron. Soc., 446, 3895, doi: 10.1093/mnras/stu2314

Flaugher, B. 2005, Int. J. Mod. Phys. A, 20, 3121, doi: 10.1142/S0217751X05025917

Flaugher, B., Diehl, H. T., Honscheid, K., et al. 2015, Astron. J., 150, 150, doi: 10.1088/0004-6256/150/5/150

Foreman-Mackey, D., Hogg, D. W., Lang, D., & Goodman, J. 2012, doi: 10.1086/670067

Fraley, G. S. 1968, Astrophys. Space Sci., 2, 96, doi: 10.1007/BF00651498

Frohmaier, C., Sullivan, M., Nugent, P. E., Goldstein, D. A., & DeRose, J. 2017, Astrophys. J. Suppl. Ser., 230, 4, doi: 10.3847/1538-4365/aa6d70

Gal-Yam, A. 2012, 337, doi: 10.1126/science.1203601

Gal-Yam, A., Mazzali, P., Ofek, E. O., et al. 2009, 462, 624, doi: 10.1038/nature08579

Goldstein, D. A., D'Andrea, C. B., Fischer, J. A., et al. 2015, Astron. J., 150, 82, doi: 10.1088/0004-6256/150/3/82

Greiner, J., Mazzali, P. a., Kann, D. A., et al. 2015, Nature, 523, 189, doi: 10.1038/nature14579

Guillochon, J., Parrent, J., Kelley, L. Z., & Margutti, R. 2016, Astrophys. J., 835, 64, doi: 10.3847/1538-4357/835/1/64

Guy, J., Sullivan, M., Conley, A., et al. 2010, Astron. Astrophys., 523, A7, doi: 10.1051/0004-6361/201014468

Hönig, S. F., Watson, D., Kishimoto, M., et al. 2017, Mon. Not. R. Astron. Soc., 464, 1693, doi: 10.1093/mnras/stw2484

Hopkins, A. M., & Beacom, J. F. 2006, 15, doi: 10.1086/506610

Howell, D. A., Sullivan, M., Perrett, K., et al. 2005, Astrophys. J., 634, 1190, doi: 10.1086/497119

Howell, D. A., Kasen, D., Lidman, C., et al. 2013, Astrophys. J., 779, 98, doi: 10.1088/0004-637X/779/2/98

Hubble, E. 1929, Proc. Natl. Acad. Sci., 15, 168, doi: 10.1073/pnas.15.3.168

Iben, I., J., & Tutukov, A. V. 1984, Astrophys. J. Suppl. Ser., 54, 335, doi: 10.1086/190932

Ilbert, O., Arnouts, S., McCracken, H. J., et al. 2006, Astron. Astrophys., 457, 841, doi: 10.1051/0004-6361:20065138

Inserra, C., Prajs, S., Gutierrez, C. P., et al. 2017, Astrophys. J., 854, doi: 10.3847/1538-4357/aaaaaa

Inserra, C., & Smartt, S. J. 2014, Superluminous Supernovae as Standardisable Candles and High-Redshift Probes, doi: 10.1088/0004-637X/796/2/87. http://stacks.iop.org/0004-637X/796/i=2/a=87?key=crossref.46c075724bc994c524d5a7614ecbf6f5

Inserra, C., Smartt, S. J., Jerkstrand, A., et al. 2013, Astrophys. J., 770, 128, doi: 10.1088/0004-637X/770/2/128

Inserra, C., Nichol, R. C., Scovacricchi, D., et al. 2018, Astron. Astrophys., 609, A83, doi: 10.1051/0004-6361/201731758

James, F., & Roos, M. 1975, Comput. Phys. Commun., 10, 343, doi: 10.1016/0010-4655(75)90039-9

Jerkstrand, A., Smartt, S. J., Inserra, C., et al. 2016, doi: 10.3847/1538-4357/835/1/13

Jones, D. O., Scolnic, D. M., Riess, A. G., et al. 2017

Kaiser, N., Burgett, W., Chambers, K., et al. 2010, in Society of Photo-Optical Instrumentation Engineers (SPIE) Conference Series, Vol. 7733, Soc. Photo-Optical Instrum. Eng. Conf. Ser., 0

Karpenka, N. V., Feroz, F., & Hobson, M. P. 2012, Mon. Not. R. Astron. Soc, 000, 1. https://arxiv.org/abs/arXiv:1208.1264v3

Kasen, D., & Bildsten, L. 2010, Astrophys. J., 717, 245, doi: 10.1088/0004-637X/717/1/245

Kessler, R., Bernstein, J. P., Cinabro, D., et al. 2009, Publ. Astron. Soc. Pacific, 121, 1028, doi: 10.1086/605984

Kessler, R., Bassett, B., Belov, P., et al. 2010, Publ. Astron. Soc. Pacific, 122, 1415, doi: 10.1086/657607

Kessler, R., Marriner, J., Childress, M., et al. 2015, Astron. J., 150, 172, doi: 10.1088/0004-6256/150/6/172

Khachiyan, L. G. 1980, USSR Comput. Math. Math. Phys., 20, 53, doi: 10.1016/0041-5553(80)90061-0

Khokhlov, A. M., Höflich, P. A., Oran, E. S., et al. 1999, Astrophys. J., 524, L107, doi: 10.1086/312305

Krige, d. g. 1951, A Statistical Approach to Some Mine Valuation and Allied Problems on the Witwatersrand (publisher not identified). https://books.google.co.uk/books?id=M6jASgAACAAJ

Law, N. M., Kulkarni, S. R., Dekany, R. G., et al. 2009, Publ. Astron. Soc. Pacific, 121, 1395, doi: 10.1086/648598

Le Borgne, D., & Rocca-Volmerange, B. 2002, Astron. Astrophys., 386, 446, doi: 10.1051/0004-6361:20020259

Le Fèvre, O., Cassata, P., Cucciati, O., et al. 2013, Astron. Astrophys., 559, A14, doi: 10.1051/0004-6361/201322179

Leloudas, G., Schulze, S., Krühler, T., et al. 2015a, 449, 917, doi: 10.1093/mnras/stv320

Leloudas, G., Patat, F., Maund, J. R., et al. 2015b, Astrophys. J. Lett., 815, L10, doi: 10.1088/2041-8205/815/1/L10

Levan, A. J., Tanvir, N. R., Starling, R. L., et al. 2014, Astrophys. J., 781, 13, doi: 10.1088/0004-637X/781/1/13

Levenberg, K. 1944, Q. Appl. Math., 2, 164, doi: 10.1090/qam/10666

Li, W., Chornock, R., Leaman, J., et al. 2011, Mon. Not. R. Astron. Soc., 412, 1473, doi: 10.1111/j.1365-2966.2011.18162.x

Lidman, C., Ruhlmann-Kleider, V., Sullivan, M., et al. 2012, Publ. Astron. Soc. Aust., 30, e001, doi: 10.1017/pasa.2012.001

Lilly, S. J., Fevre, O. L., Renzini, A., et al. 2007, Astrophys. J. Suppl. Ser., 172, 70, doi: 10.1086/516589

Lochner, M., McEwen, J. D., Peiris, H. V., Lahav, O., & Winter, M. K. 2016, Astrophys. J. Suppl. Ser., 225, 31, doi: 10.3847/0067-0049/225/2/31

Lunnan, R., Chornock, R., Berger, E., et al. 2013, Astrophys. J., 771, 97, doi: 10.1088/0004-637X/771/2/97

—. 2014, Astrophys. J., 787, 138, doi: 10.1088/0004-637X/787/2/138

—. 2015, Astrophys. J., 804, doi: 10.1088/0004-637X/804/2/90

Magnier, E. A., & Cuillandre, J.-C. 2004, 116, 449, doi: 10.1086/420756

Margalit, B., Metzger, B. D., Thompson, T. A., Nicholl, M., & Sukhbold, T. 2018, Mon. Not. R. Astron. Soc., 475, 2659, doi: 10.1093/mnras/sty013

Markwardt, C. B. 2008, XXX. https://arxiv.org/abs/arXiv:0902.2850v1

Marquardt, D. W. 1963, J. Soc. Ind. Appl. Math., 11, 431, doi: 10.1137/0111030

Mazzali, P. A., Sullivan, M., Pian, E., Greiner, J., & Kann, D. A. 2016, Mon. Not. R. Astron. Soc., 458, 3455, doi: 10.1093/mnras/stw512

Mazzali, P. A., Sullivan, M., Filippenko, A. V., et al. 2015, Mon. Not. R. Astron. Soc., 450, 2631, doi: 10.1093/mnras/stv761

McCrum, M., Smartt, S. J., Rest, A., et al. 2014a, Mon. Not. R. Astron. Soc., 448, 1206, doi: 10.1093/mnras/stv034

McCrum, M., Smartt, S. J., Kotak, R., et al. 2014b, Mon. Not. R. Astron. Soc., 437, 656, doi: 10.1093/mnras/stt1923

McCulloch, W. S., & Pitts, W. 1943, Bull. Math. Biophys., 5, 115, doi: 10.1007/BF02478259

Metzger, B. D., Margalit, B., Kasen, D., & Quataert, E. 2015, Mon. Not. R. Astron. Soc., 454, 3311, doi: 10.1093/mnras/stv2224

Möller, A., Ruhlmann-Kleider, V., Leloup, C., et al. 2016. https://arxiv.org/abs/arXiv:1608.05423v2

More, J. J., Garbow, B. S., & Hillstrom, K. E. 1980, User Guide for Minpack-1. http://inspirehep.net/record/155642?ln=en

Neill, J. D., Sullivan, M., Gal-Yam, A., et al. 2011, Astrophys. J., 727, 15, doi: 10.1088/0004-637X/727/1/15

Nicholl, M., Guillochon, J., & Berger, E. 2017, Astrophys. J., 850, 55, doi: 10.3847/1538-4357/aa9334

Nicholl, M., & Smartt, S. J. 2016, Mon. Not. R. Astron. Soc. Lett., 457, L79, doi: 10.1093/mnrasl/slv210

Nicholl, M., Smartt, S. J., Jerkstrand, A., et al. 2013, Nature, 502, 346, doi: 10.1038/nature12569

—. 2014, 2096, doi: 10.1093/mnras/stu1579

—. 2015a, Mon. Not. R. Astron. Soc., 452, 3869, doi: 10.1093/mnras/stv1522

—. 2015b, Astrophys. J. Lett., 807, doi: 10.1088/2041-8205/807/1/L18

Nomoto, K., Tolstov, A., Sorokina, E., et al. 2016, Proc. Int. Astron. Union, 12, 39, doi: 10.1017/S174392131700343X

Nugent, P., Sullivan, M., Ellis, R., et al. 2006, Astrophys. J., 645, 841, doi: 10.1086/504413

Ofek, E. O., Cameron, P. B., Kasliwal, M. M., et al. 2007a, Astrophys. J., 659, L13, doi: 10.1086/516749

—. 2007b, Astrophys. J., 659, L13, doi: 10.1086/516749

Oliphant, T. E. 2007, Comput. Sci. Eng., 9, 10, doi: 10.1109/MCSE.2007.58

Pan, Y. C., Foley, R. J., Smith, M., et al. 2017, doi: 10.1093/mnras/stx1467

Papadopoulos, A., D'Andrea, C. B., Sullivan, M., et al. 2015, Mon. Not. R. Astron. Soc, 449, 0, doi: 10.1093/mnras/stv174

Pastorello, A., Turatto, M., Benetti, S., et al. 2002, Mon. Not. R. Astron. Soc., 333, 27, doi: 10.1046/j.1365-8711.2002.05366.x

Pastorello, A., Smartt, S. J., Botticella, M. T., et al. 2010, Astrophys. J., 724, L16, doi: 10.1088/2041-8205/724/1/L16

Perlmutter, S., Aldering, G., Goldhaber, G., et al. 1999, Astrophys. J., 517, 565, doi: 10.1086/307221

Perrett, K., Balam, D., Sullivan, M., et al. 2010, Astron. J., 140, 518, doi: 10.1088/0004-6256/140/2/518

Perrett, K., Sullivan, M., Conley, A., et al. 2012, Astron. J., 144, 59, doi: 10.1088/0004-6256/144/2/59

Phillips, M. M. 1993, Astrophys. J., 413, L105, doi: 10.1086/186970

Piro, A. L. 2015, Astrophys. J. Lett., 808, 1, doi: 10.1088/2041-8205/808/2/L51

Prajs, S., Sullivan, M., Smith, M., et al. 2016, Mon. Not. R. Astron. Soc., 464, 3568, doi: 10.1093/mnras/stw1942

Prat, J., Sánchez, C., Fang, Y., et al. 2017. https://arxiv.org/abs/1708.01537

Pritchet, C. J., & Collaboration, S. 2004, Obs. Dark Energy, ASP Conf. Ser., 339, 9. https://arxiv.org/abs/0406242

Pursiainen, M., Childress, M., Smith, M., et al. 2018. https://arxiv.org/abs/1803.04869

Quimby, R. 2014, The First UV Spectra of a Hydrogen-Rich Superluminous Supernova, HST Proposal

Quimby, R. M. 2006, ProQuest Diss. Theses; Thesis (Ph.D.)–The Univ. Texas Austin

Quimby, R. M., Aldering, G., Wheeler, J. C., et al. 2007, Astrophys. J., 668, L99, doi: 10.1086/522862

Quimby, R. M., Yuan, F., Akerlof, C., & Wheeler, J. C. 2013, Mon. Not. R. Astron. Soc., 431, 912, doi: 10.1093/mnras/stt213

Quimby, R. M., Kulkarni, S. R., Kasliwal, M. M., et al. 2011, Nature, 474, 487, doi: 10.1038/nature10095

Rasmussen, C. E., & Williams, C. K. 2006, Gaussian Processes for Machine Learning

Rau, A., Kulkarni, S. R., Law, N. M., et al. 2009, Publ. Astron. Soc. Pacific, 121, 1334, doi: 10.1086/605911

Rest, A., Garnavich, P. M., Khatami, D., et al. 2018, 1. https://arxiv.org/abs/1804.04641

Riess, A. G., Filippenko, A. V., Challis, P., et al. 1998, \aj, 116, 1009, doi: 10.1086/300499

Roming, P. W., Kennedy, T. E., Mason, K. O., et al. 2005, Space Sci. Rev., 120, 95, doi: 10.1007/s11214-005-5095-4

Russakovsky, O., Deng, J., Su, H., et al. 2015, Int. J. Comput. Vis., 115, 211, doi: 10.1007/s11263-015-0816-y

Saxena, A., Marinello, M., Overzier, R. A., et al. 2018, Publ. Astron. Soc. Japan, 00, 1, doi: 10.1093/pasj/xxx000

Scalzo, R. A., Ruiter, A. J., & Sim, S. A. 2014, Mon. Not. R. Astron. Soc., 445, 2535, doi: 10.1093/mnras/stu1808

Schlegel, E. M. 1995, Astron. J., 109, 2620, doi: 10.1086/117475

Schulze, S., Krühler, T., Leloudas, G., et al. 2016, MNRAS, 473, 1258, doi: 10.1093/mnras/stx2352

Scovacricchi, D., Nichol, R. C., Bacon, D., Sullivan, M., & Prajs, S. 2015, Mon. Not. R. Astron. Soc., 456, 1700, doi: 10.1093/mnras/stv2752

Skilling, J. 2006, Bayesian Anal., 1, 833, doi: 10.1214/06-BA127

Slipher, V. M. 1915, Pop. Astron., 23, 21

Smith, M., Sullivan, M., D'Andrea, C. B., et al. 2015, Astrophys. J. Lett., 818, doi: 10.3847/2041-8205/818/1/L8

Smith, M., Sullivan, M., Nichol, R. C., et al. 2018, Astrophys. J., 854, 37, doi: 10.3847/1538-4357/aaa126

Smith, N., Li, W., Foley, R. J., et al. 2007, Astrophys. J., 666, 1116, doi: 10.1086/519949

Sorokina, E., Blinnikov, S., Nomoto, K., Quimby, R., & Tolstov, A. 2015, ArXiv e-prints, doi: 10.3847/0004-637X/829/1/17

Sternberg, A. 2013, Science, 856, 856, doi: 10.1126/science.1203836

Sullivan, M., Howell, D. A., Perrett, K., et al. 2006, Astron. J., 131, 960, doi: 10.1086/499302

Sullivan, M., Guy, J., Conley, A., et al. 2011, SNLS3: Constraints on dark energy combining the Supernova Legacy Survey three-year data with other probes, doi: 10.1088/0004-637X/737/2/102. http://iopscience.iop.org/article/10.1088/0004-637X/737/2/102/pdfhttp://stacks.iop.org/0004-637X/737/i=2/a=102?key=crossref.e735c12c199d3274597f8a25549eebcdhttp://arxiv.org/abs/1104.1444http://dx.doi.org/10.1088/0004-637X/737/2/102

Tauris, T. M., Langer, N., Moriya, T. J., et al. 2013, Astrophys. J. Lett., 778, L23, doi: 10.1088/2041-8205/778/2/L23

Tully, R. 1988, J. Br. Astron. Assoc., 98, 316

Vreeswijk, P. M., Savaglio, S., Gal-Yam, A., et al. 2014, Astrophys. J., 797, 206, doi: 10.1088/0004-637X/797/1/24

Wang, S. Q., Wang, L. J., Dai, Z. G., & Wu, X. F. 2015, Astrophys. Journal, Vol. 807, Issue 2, Artic. id. 147, 10 pp. (2015)., 807, 1, doi: 10.1088/0004-637X/807/2/147

Whelan, J., & Iben, Icko, J. 1973, Astrophys. J., 186, 1007, doi: 10.1086/152565

Woosley, S. E. 2010, Astrophys. J. Lett., 719, L204, doi: 10.1088/2041-8205/719/2/L204

Woosley, S. E., Blinnikov, S., & Heger, A. 2007, Nature, 450, 390, doi: 10.1038/nature06333

Yan, L., Perley, D. A., De Cia, A., et al. 2017. https://arxiv.org/abs/1711.01534

Yan, L., Quimby, R., Ofek, E., et al. 2015, Astrophys. J., 814, 108, doi: 10.1088/0004-637X/814/2/108

Yaron, O., & Gal-Yam, A. 2012, Publ. Astron. Soc. Pacific, 124, 668, doi: 10.1086/666656

Zwicky, F. 1938, \pasp, 50, 215